Title
Fundamental Study on Laser Interaction with Metal Matrix Nanocomposites

Author
Ma, Chao

Publication Date
2015

Peer reviewed|Thesis/dissertation

UNIVERSITY OF CALIFORNIA

Los Angeles

Fundamental Study on Laser Interaction with Metal Matrix Nanocomposites

A dissertation submitted in partial satisfaction of the

requirements for the degree Doctor of Philosophy

in Mechanical Engineering

by

Chao Ma

2015

ABSTRACT OF THE DISSERTATION

Fundamental Study on Laser Interaction with Metal Matrix Nanocomposites

by

Chao Ma

Doctor of Philosophy in Mechanical Engineering

University of California, Los Angeles, 2015

Professor Xiaochun Li, Chair

The objective of this study is to significantly advance the fundamental understanding of laser interaction with metal matrix nanocomposites (MMNCs) and to overcome the fundamental limits of current laser processing techniques by tuning heat transfer and fluid flow using nanoparticles. MMNC, also known as nanoparticles reinforced metal, is an emerging class of materials exhibiting unusual mechanical, physical, and chemical properties. Laser, as an advanced processing tool, has been extensively studied for metal processing and has brought huge impacts in industries. It is of tremendous scientific and technical interests to conduct a fundamental study on laser interaction with MMNCs. In addition, previous research shows nanoparticles can considerably change the thermophysical properties of MMNCs as compared with the base metals

or alloys. Hence it is possible to use nanoparticles to tailor the heat transfer and fluid flow during laser melting and thus potentially break the fundamental limits of laser processing techniques.

In this study, electrocodeposition was used to prepare MMNCs samples (e.g., Ni/Al_2O_3 and Ni/SiC) for laser melting experiments. The average diameter of Al_2O_3 or SiC nanoparticles used this study was 50 nm. Characterizations by scanning electron microscopy (SEM) showed that uniform distribution and dispersion of nanoparticles were achieved by ultrasonic assisted electrocodeposition. Vickers hardness tests showed that the Ni/Al_2O_3 (4.4 vol. %) was 73.6 % harder than the pure Ni.

The effects of nanoparticles on the optical and thermophysical properties were studied both experimentally and theoretically since these essential properties to study laser interaction with MMNCs had not been available. Firstly, using a power meter, the reflectivity of Ni/Al_2O_3 (1.8 vol. %) was measured to be 65.8 % while pure Ni was at 67.4%, indicating that the Al_2O_3 nanoparticles did not change the reflectivity substantially. In order to determine the surface tension and viscosity of MMNCs, an innovative measurement system was developed based on the accessible laser system, inspired by the so-called oscillating drop method. The surface tensions of Ni/Al_2O_3 (4.4 vol. %) and Ni/SiC (3.6 vol. %) at ~1500 °C were 1.39 ± 0.03 N/m and 1.57 ± 0.06 N/m, respectively, slightly lower than that of pure Ni, 1.68 ± 0.04 N/m. The viscosities of these Ni/Al_2O_3 and Ni/SiC MMNCs at ~1500 °C were 13.3 ± 0.8 mPa·s and 17.3 ± 3.1 mPa·s, respectively, significantly higher than that of pure Ni, 4.8 ± 0.3 mPa·s. Differential scanning calorimetry was used to determine the heat capacity of the same MMNCs. The specific heat capacities of the Ni/Al_2O_3 and Ni/SiC at room temperature were 424 ± 13 J/(kg·K) and 423 ± 14 J/(kg·K), respectively, close to that of pure Ni, 424 ± 8 J/(kg·K). An experimental setup was developed to measure thermal conductivity based on the laser flash method. The thermal

conductivities of these Ni/Al_2O_3 and Ni/SiC MMNCs at room temperature were 84.1 ± 3.4 W/(m·K) and 87.3 ± 3.4 W/(m·K), respectively, slightly less than that of pure Ni, 91.7 ± 2.8 W/(m·K). Theoretical models based on the effective medium approximation theory were also used to predict the heat capacity and thermal conductivity of the MMNCs. The prediction results matched well with the measurements. The knowledge of the optical and thermophysical properties of MMNCs would provide valuable insights to fundamentally understand how laser interacts with MMNCs.

To understand the influences of the nanoparticles-modified thermophysical properties on laser melting, an analytical model was developed to theoretically predict the melt pool flows. An experimental study was then conducted for comparison. The predicted surface topography introduced by thermocapillary flows matched well with the measurements from white light interferometry. Both the theoretical and experimental results indicated that the thermocapillary flows were tremendously suppressed because of the increased viscosity by the addition of nanoparticles. As an emerging application of laser melting, laser polishing could significantly benefit from this new phenomenon because an effective suppression of thermocapillary flows would result in an improved surface finish. This study suggested the laser melting of Ni/Al_2O_3 (4.4 vol. %) resulted in the best surface finish.

Systematic laser polishing experiments at various laser pulse energies were conducted on Ni/Al_2O_3 (4.4 vol. %) and pure Ni for comparison. It was discovered that the suppression of thermocapillary flows by nanoparticles enlarged the processing window of the capillary regime of laser polishing. In addition, the nanoparticles-enabled viscosity enhancement also improved the smoothening effects of the capillary regime due to an increased viscous damping of capillary oscillations. The surface roughness of the Ni/Al_2O_3 was reduced from 323 nm to 72 nm with the

optimal laser polishing parameters while that of pure Ni only from 254 nm to 107 nm. The normalized surface roughness was decreased by nearly a factor of two with the help of nanoparticles. The study demonstrated the proposed methodology of controlling heat transfer and fluid flow by nanoparticles successfully overcame one of the fundamental limits in laser processing.

The microstructural study on the laser processed region also revealed interesting features. By the addition of the 4.4 vol. % Al_2O_3 nanoparticles, the laser melted zone (MZ) depth was increased from 1.9 μm to 3.1 μm while the heat affected zone (HAZ) size was, surprisingly, largely reduced from 8.3 μm to 2.7 μm. To better understand why nanoparticles induced such an interesting modification in microstructures, numerical simulations were performed using the newly measured effective optical and thermophysical properties as input parameters to account for the effects of nanoparticles. The simulation results indicate that the addition of nanoparticles inhibit the heat transfer and thus enhance heat accumulation within the surface layer to effectively increase the MZ depth. On the other hand, the nanoparticles substantially restrict the grain growth to shrink HAZ remarkably. It would be of great significance if this phenomenon can be utilized to other manufacturing processes such as laser welding and laser additive manufacturing where a minimal HAZ is highly desired.

In summary, analytical, numerical and experimental approaches have been established to significantly advance fundamental understanding of laser melting of MMNCs, especially on the specific effects of nanoparticles on the process. This study has demonstrated the feasibility to tune the thermophysical properties and thus control the laser processing outcomes by nanoparticles, which can be applied to other laser-based manufacturing technologies to improve the process capability and broaden the application space.

The dissertation of Chao Ma is approved.

Tsu-Chin Tsao

Pei-Yu Chiou

Jenn-Ming Yang

Xiaochun Li, Committee Chair

University of California, Los Angeles

2015

Dedicated to my parents for their unconditional love.

TABLE OF CONTENTS

ACKNOWLEDGEMENTS

I would like to thank Professor Xiaochun Li for his remarkable support and guidance, without which this would not be possible. He always emphasized on gaining a thorough scientific understanding prior to conducting experimental research, which helped me to lay a solid foundation of the knowledge required for my Ph.D. study and even for my future career. In addition, I want to thank him for the freedom he granted me to explore different ideas and solve technical problems independently.

I would also like to acknowledge Professors Tsu-Chin Tsao, Pei-Yu Chiou and Jenn-Ming Yang for serving in my doctoral committee. I really appreciate their valuable inputs for my research.

I am also very grateful to all of my colleagues in the research group. I benefited greatly from the technical discussions with them, which inspired many wonderful ideas.

VITA

2012, M.S., Mechanical Engineering, University of Wisconsin–Madison, US

2010, B.S., Mechanical Engineering, Tsinghua University, Beijing, China

2010, B.A., Economics, Tsinghua University, Beijing, China

JOURNAL PAPERS

- **Ma, C.**, Chen, L., Xu, J., Zhao, J., and Li, X., 2015, "Control of Fluid Dynamics by Nanoparticles in Laser Melting," *Journal of Applied Physics*, Vol. 117, pp. 114901-1–114901-8.

- **Ma, C.**, Vadali, M., Li, X., Duffie, N.A., and Pfefferkorn, F.E., 2014, "Analytical and Experimental Investigation of Thermocapillary Flow in Pulsed Laser Micropolishing," *Journal of Micro and Nano-Manufacturing*, Vol. 2(2), pp. 021010-1–021010-8.

- **Ma, C.**, Vadali, M., Duffie, N.A., Pfefferkorn, F.E., and Li, X., 2013, "Melt Pool Flow and Surface Evolution during Pulsed Laser Micro Polishing of Ti6Al4V," *Journal of Manufacturing Science and Engineering*, Vol. 135, pp. 061023-1–061023-8.

- **Ma, C.**, Chen, L., Xu, J., Fehrenbacher, A., Li, Y., Pfefferkorn, F.E., Duffie, N.A., Zheng, J., and Li, X., 2013, "Effect of Fabrication and Processing Technology on the Biodegradability of Magnesium Nanocomposites," *Journal of Biomedical Materials Research Part B: Applied Biomaterials*, Vol. 101B(5), pp. 870–877.

- Vadali, M., **Ma, C.**, Duffie, N.A., Li, X., and Pfefferkorn, F.E., 2013, "Effects of Pulse Duration on Laser Micro Polishing," *Journal of Micro and Nano-Manufacturing*, Vol. 1(1), pp. 011006-1–011006-9.

- Li, H., Choi, H., **Ma, C.**, Zhao, J., Jiang, H., Cai, W., Abell, J.A., and Li, X., 2013, "Transient Temperature and Heat Flux Measurement in Ultrasonic Joining of Battery Tabs Using Thin-Film Microsensors," *Journal of Manufacturing Science and Engineering*, Vol. 135, pp. 051015-1–051015-8.

- Pfefferkorn, F.E, Duffie, N.A, Li, X., Vadali, M., and **Ma, C.**, 2013, "Improving Surface Finish in Pulsed Laser Micro Polishing Using Thermocapillary Flow," *CIRP Annals*, Vol. 62(1), pp. 203–206.

- Vadali, M., **Ma, C.**, Duffie, N.A., Li, X., and Pfefferkorn, F.E., 2012, "Pulsed Laser Micro Polishing: Surface Prediction Model," *Journal of Manufacturing Processes*, Vol. 14, pp. 307–315.

- Chen, L., Konishi, H., Fehrenbacher, A., **Ma, C.**, Xu, J., Choi, H., Xu, H., Pfefferkorn, F.E, and Li, X., 2012, "Novel Nanoprocessing Route for Bulk Graphene Nanoplatelets Reinforced Metal Matrix Nanocomposites," *Scripta Materialia*, Vol. 67(1), pp. 29–32.

- Guha, A., Li, H., Sun, Z., **Ma, C.**, Werschmoeller, D., and Li, X., 2012, "Wireless Acquisition of Temperature Data from Embedded Thin Film Sensors in Cutting Insert," *Journal of Manufacturing Processes*, 2012, Vol. 14(3), pp. 360–365.

CONFERENCE PAPERS

- **Ma, C.**, Vadali, M., Duffie, N.A., Pfefferkorn, F.E., and Li, X., 2013, "Effect of Thermocapillary Flow on the Surface Profile in Pulsed Laser Micro Polishing," *The 8th International Conference on Micro Manufacturing*, Victoria, BC, Canada. ***(Honorable Paper Award)***

- **Ma, C.**, Vadali, M., Duffie, N.A., Pfefferkorn, F.E., and Li, X., 2013, "Melt Pool Flow and Surface Evolution during Pulsed Laser Micro Polishing of Ti6Al4V," *The ASME International Manufacturing Science and Engineering Conference*, Madison, WI, US.

- **Ma, C.**, Chen, L., Xu, J., Fehrenbacher, A., Li, Y., Pfefferkorn, F.E., Duffie, N.A., Zheng, J., and Li, X., 2012, "Biodegradability and Mechanical Performance of Hydroxyapatite Reinforced Magnesium Matrix Nanocomposites," *TMS Annual Meeting*, Orlando, FL, US.

- Vadali, M., **Ma, C.**, Li, X., Pfefferkorn, F.E., and Duffie, N.A., 2013, "Effects of Irregular, Adaptive Scan Trajectories for Pulsed Laser Micro Polishing," *The 8th International Conference on Micro Manufacturing*, Victoria, BC, Canada.

- Vadali, M., **Ma, C.**, Duffie, N.A., Li, X., and Pfefferkorn, F.E., 2012, "Effects of Laser Pulse Duration on Pulsed Laser Micro Polishing," T*he 7th International Conference on Micro Manufacturing*, Evanston, IL, US.

- Chen, L., Choi, H., Fehrenbacher, A., Xu, J., **Ma, C.**, and Li, X., 2012, "Uniform Dispersion of Nanoparticles in Metal Matrix Nanocomposites," *TMS Annual Meeting*, Orlando, FL, US.

- Vadali, M., **Ma, C.**, Duffie, N.A., Li, X., and Pfefferkorn, F.E., 2011, "Pulsed Laser Micro Polishing: Surface Prediction Model," *The 6th International Conference on Micro Manufacturing*, Tokyo, Japan. ***(Outstanding Paper Award)***

- Vadali, M., **Ma, C.**, Duffie, N.A., Li, X., and Pfefferkorn, F.E., 2011, "Model Guided Pulsed Laser Micro Polishing of H13 Tool Steel," *The 44th CIRP Conference on Manufacturing Systems*, Madison, WI, US.

- Vadali, M., **Ma, C.**, Duffie, N.A., Li, X., and Pfefferkorn, F.E., 2011, "Pulsed Laser Micro Polishing: an Analytical Method for Predicting Surface Finish," *The ASME International Manufacturing Science and Engineering Conference*, Corvallis, OR, US.

- Xu, J., Cao, C., Das, S., Chen, L., **Ma, C.**, Mishra, R.S., and Li, X., 2015, "High Performance Mg6Zn Nanocomposites Fabricated Through Friction Stir Processing," *TMS Annual Meeting*, San Antonio, TX, US.

PATENT

- Vadali, V.M., **Ma, C.**, Duffie, N.A., Li, X., and Pfefferkorn, F.E., 2014, "Reducing Surface Asperities," US 2014/0202997 A1

CHAPTER 1. INTRODUCTION

1.1 BACKGROUND AND MOTIVATION

Metal matrix nanocomposite (MMNC), or nanoparticles reinforced metal, is an emerging class of materials with nano-sized particulates incorporated in the metal matrix. MMNCs have great potentials to provide significantly enhanced mechanical properties, thermophysical properties, electrical and chemical properties, and so on. There is an explosive growth in fundamental research and technical development in recent years trying to unleash their unusual performance for widespread applications [Rawal 2001, Crainic 2002, Jiang 2003, Yang 2004, Cao 2008, Kuo 2004, Qu 2004, Low 2006, Chen 2006, Bund 2007, Borkar 2011, García-Lecina 2012].

Laser, as an advanced materials processing tool, has been used to process (e.g., melt or ablate) metals for decades and showed remarkable impacts in industries [Ready 2001, Steen 2010]. It is of tremendous scientific and technical interests to use laser to process MMNCs. For example, there is fast-growing research and development of laser additive manufacturing (AM) processes, such as selective laser melting (SLM) for MMNC products [Gu 2009, Gu 2010, Gu 2011, Gu 2012, Gu 2014, Biedunkiewicz 2011, Figiel 2012, Biedunkiewicz 2013, Dadbakhsh 2012, Song 2013]. As one of the most promising AM process, SLM has been successfully used to fabricate three-dimensional metallic parts with complex geometries and configurations directly from fine powders. Nanocomposite concept was recently introduced to SLM processes where nanoparticles were added and mixed into the original SLM powders to investigate the potential benefits. While most past research focused on the mechanical properties affected by nanoparticles, little fundamental

understanding has been obtained on the underlining physics of the process, especially the effects of nanoparticles on the laser melting process, such as how nanoparticles would change laser-mater interaction (e.g., absorption and reflection), thermophysical properties (e.g., surface tension, viscosity, and thermal conductivity), thus heat transfer and melt pool flow, and eventually the microstructure and material performance. It is highly essential to fill this gap of fundamental knowledge on how laser interacts with MMNCs. The knowledge on how the nanoparticles affect the absorption of laser energy by metals and thermophysical properties of metals is valuable not only in the laser surface melting domain (e.g., laser welding, laser polishing, laser texturing, laser cladding, etc.) but also in laser surface heating domain where melting does not occur (e.g., laser hardening, laser peening, etc.).

Moreover, this study is also motivated by an intriguing hypothesis that the introduction of nanoparticles in the laser-induced melt pool would break fundamental limits that exist in some current laser processing techniques. For example, the surface conditions (e.g., residual roughness, gloss and reflectivity) that can be possibly achieved by laser polishing are limited. Recent studies have shown that these barriers are directly related to melt pool dynamics such as capillary oscillations and thermocapillary (Marangoni) flows [Vadali 2012, Vadali 2013, Ma 2013, Pfefferkorn 2013, Ma 2014], which are further determined by thermophysical properties of the metal melt. On the other hand, studies have shown that thermophysical properties of a material can be tailored by addition of nanoparticles [Vafaei 2006, Vafaei 2009, Kim 2006, Corcione 2011, Poudel 2008, Biswas 2012, Zebarjadi 2011]. Such engineering nanocomposites have properties that are dependent on the material, size, and fraction of the nanoparticles. Therefore, there is an opportunity to break the limits/barriers of current laser materials processing technologies by tuning melt pool dynamics via nanoparticles, possibly significantly broadening laser melting capability

and application space. For example, the ability to quickly create a smoother finish on a part through laser polishing is expected to significantly benefit manufacturers of medical devices, optical instruments, automobile and aerospace components, and so on.

1.2 OVERARCHING GOALS AND SPECIFIC RESEARCH OBJECTIVES

The overarching goals of this study are: (a) to significantly advance the fundamental understanding of the interactions and outcomes of laser melting of metal matrix nanocomposites (MMNCs), (b) to overcome the existing limit of laser processing by tuning melt pool dynamics using nanoparticles, (c) to extend capability and application space of laser melting processes. More specifically, the research objective is to understand the exact influence of nanoparticles on laser melting, which includes the effects of nanoparticles on the optical and thermophysical properties of the base metal, the corresponding heat transfer and melt pool flow processes, and the consequent surface property and microstructure.

1.3 OUTLINE

The remaining part of the dissertation will be organized as follows.

- Chapter 2 reviews the existing work of high relevance to this study.
- Chapter 3 describes the fabrication of MMNC samples using electrocodeposition.
- Chapter 4 conducts theoretical and experimental studies to understand and measure the optical and thermophysical properties of MMNCs.

- In Chapter 5, analytical study of laser melting of MMNCs is carried out based on the measured material properties from Chapter 4.
- A systematic experimental study is performed in Chapter 6 on the selected material system with the guidance of the initial investigation in Chapter 5.
- The conclusions of this work are made in Chapter 7.
- Future work is recommended in Chapter 8.

CHAPTER 2. LITERATURE REVIEW

The literature review begins with a brief introduction to metal matrix nanocomposite (MMNCs), followed by a thorough review on electrocodeposition of MMNCs, which is the method used for preparation of MMNC samples in this study. The existing studies on laser interaction with MMNCs are then described in detail. Melt pool flow is crucial for many laser processing techniques, and therefore possible fluid flow patterns in a laser-induced melt pool are reviewed. Laser polishing will be used as an example to investigate the possibility to overcome a fundamental limit of laser processing using nanoparticles, hence an extensive literature survey on laser polishing is presented. Finally, the effects of nanoparticles on thermophysical properties are reviewed in order to examine the feasibility of tuning thermophysical properties by nanoparticles.

2.1 METAL MATRIX NANOCOMPOSITES

Incorporation of nanoparticles into materials can lead to significantly enhanced chemical, physical, and mechanical properties. A great deal of work has been done on polymer-based matrix materials with unusual properties. Recently, significant effort has been taken to develop metal matrix nanocomposites (MMNCs) [Rawal 2001, Crainic 2002, Jiang 2003, Yang 2004, Cao 2008, Zimmerman 2002, Kuo 2004, Qu 2004, Low 2006, Chen 2006, Bund 2007, Borkar 2011, García-Lecina 2012, Tong 1998a, Tong 1998b, Niu 1998, Islamgaliev 2001, Audebert 2002, Yamasaki 2003, Hirosawa 2003]. As compared with conventional metal matrix composites (MMCs) that are reinforced with micro inclusions, this new class of material can overcome many disadvantages of MMCs such as poor ductility, low fracture toughness and poor machinability [Arsenault 1991, Nardone 1986]. The matrix materials can be aluminum, titanium, copper, nickel, and iron, etc.,

and the reinforcement phases can be borides, carbides, nitrides, oxides, or their mixtures. MMNCs are poised to insert enormous impact for widespread applications in aerospace, automobile, and defense industries, to name a few.

The challenges for MMNCs manufacturing include achieving uniform distribution and effective dispersion of nanoparticles while preventing chemical reactions between nanoparticles and matrix. An effective dispersion of nanoparticles inside metal grains is crucial to enhance materials properties. However, the nanoparticles tend to agglomerate due their large surface area and high surface energy. Therefore, most research on fabrication of MMNCs has been focused on dispersion of nanoparticles via ultrasonication, surfactant, ball milling, plastic deformation, and so on. Chemical reaction of nanoparticles is another critical issue in fabrication of MMNCs, because nanoparticles are more reactive than their bulk counterpart. It is difficult to maintain the original composition and morphology of nanoparticles during manufacturing of MMNCs, especially during high temperature liquid processing. Nanoparticles have to be selected with a careful consideration on the matrix material and the process temperature in order to prevent potential chemical reactions.

Various manufacturing methods have been developed to fabricate MMNCs, including solidification processing, electrocodeposition, high energy ball milling and powder metallurgy, selective laser melting, and severe plastic deformation. A new scalable manufacturing technology has recently been developed, which combines solidification processing (e.g., casting) with ultrasonic cavitation based dispersion of nanoparticles in metal melts [Yang 2004, Cao 2008]. This innovative technique has been successfully tested in industry to produce bulk aluminum nanocomposite parts of industrial prototypical scale (e.g., 27 kg part). In addition, the mechanical

properties of MMNCs were enhanced significantly when compared with the base alloys. Electrocodeposition is another popular technique to fabricate MMNC at low cost, especially for high-performance coatings for a variety of industrial applications. Extensive research have demonstrated that the electrocodeposited MMNC coatings show significantly improved material properties such as wear and corrosion resistances over their base metal counterparts [Kuo 2004, Qu 2004, Low 2006, Chen 2006, Bund 2007, Borkar 2011, García-Lecina 2012]. Electrocodeposition is chosen to produce MMNC samples for laser melting in this work because it is compatible with lithography-based microfabrication process such that the placement of nanoparticles can be accurately controlled to enable fundamental study. For example, nanoparticles can electroplated in selected micro or sub-micron areas/features on the metal surface to serve as tracers/markers for melt pool flows.

2.2 ELECTROCODEPOSITION OF METAL MATRIX NANOCOMPOSITES

Electrocodeposition is an emerging technique to produce nanocomposite coatings with improved material properties such as wear and corrosion resistances. In electrocodeposition process, nanoparticles are suspended in the electrolyte and codeposited with the metal atoms, forming metal matrix nanocomposite layers. Electrocodeposition is advantageous over many coating techniques due to its low cost and high throughput and can be readily applied to complex geometries. Electrocodeposition is becoming more and more useful over the last two decades since the nanoparticles can provide tremendous strengthening effects and even enable advanced functional materials.

2.2.1 Materials

Low et al. conducted a literature survey which gives a detailed background to electrocodeposition of nanocomposites [Low 2006]. Various pure metals and alloys have been experimented as the matrixes such as Ni, Cu, Co, Cr, Au, Ag, Zn, Fe, and some binary alloys made of these metal elements. Selection of nanoparticles are wide, including ceramics, such as Al_2O_3, SiC, TiO_2, SiO_2, Si_3N_4, CeO_2, and ZrO_2, and carbon materials, such as diamond, carbon nanotube and graphene.

Among all materials investigated, Ni/Al_2O_3 is the most widely studied system because of its low cost and high performance as a coating for engine cylinders, high-pressure valves and dies. Extensive research validates the improved hardness, wear resistance, heat resistance and corrosion resistance by the addition of Al_2O_3 nanoparticles in Ni deposits [Kuo 2004, Qu 2004, Chen 2006, Bund 2007, Borkar 2011, García-Lecina 2012].

There has also been a great amount of research on electrocodeposition of Zn based nanocomposites, which have wide applications as corrosion-resistant coating or as catalysts for air and water purification potentially. Zinc coating has already been widely used to protect structural materials such as steels from corrosion. Recently, it was found that the addition of nanoparticles can significantly improve the corrosion resistance of zinc coatings. Many types of nanoparticles have been attempted and showed beneficial effects on inhibition of corrosion, such as carbon nanotube [Praveen 2007], TiO_2 [Praveen 2008, Vlasa 2010, Frade 2011, Kumar 2011], SiO_2 [Khan 2011], ZrO_2 [Vathsala 2011], V_2O_5 [Bindiya 2012], NiO [Chandrappa 2012], CeO_2 [Ranganatha 2012], MoS_2 [Kanagalasara 2012], B_4C [Kumar 2012], and TiO_2 + CeO_2 [Nemes 2013]. More interestingly, TiO_2 nanoparticles were found to be able to catalyze photochemical or

electrochemical reactions to purify air and water, which is attracting more and more research attention [Ito 1999, Deguchi 2001, Gomes 2005, Fusters 2008, Frade 2010, Gomes 2013].

2.2.2 Incorporation of Nanoparticles

The relationship between the incorporation amount of nanoparticles and the experimental conditions is the focus of most theoretical and experimental work. Incorporation of nanoparticles into metal deposits is dependent on many process parameters, including characteristics of nanoparticles (e.g. type, surface charge, concentration, shape, and size), electrolyte (e.g. composition, concentration, additives, surfactant, pH, and temperature), current (e.g. direct current, pulsed current, pulse time, and duty cycle), hydrodynamics (laminar, turbulent, and mixed regimes), and electrode configuration (e.g. parallel plate electrodes, rotating disk electrode, rotating cylinder electrode) [Low 2006].

2.2.2.1 Experimental Work

Experimental results showed that the amount of nanoparticles in the metal deposit can be increased by pulse current techniques and/or by increasing nanoparticle concentration in the electrolyte [Borkar 2011]. Three kinds of nanocomposite coatings, Ni/Al_2O_3, Ni/SiC and Ni/ZrO_2, were deposited with Watts baths using direct current (DC), pulsed current (PC), and pulsed reverse current (PRC). The weight percentage of reinforcements in the deposit is the lowest using DC and the highest using PRC for all three kinds of coatings. The effect of Al_2O_3 content in the electrolyte on the weight percentage of Al_2O_3 in the deposit was also experimentally studied. The weight percentage of incorporated Al_2O_3 increased nearly linearly when the Al_2O_3 concentration in the electrolyte increases from 0 to 40 g/L.

In the study on Ni/Al_2O_3 codeposition by Shao et al, the volume percentage of Al_2O_3 increased linearly with increasing Al_2O_3 concentration in the electrolyte and then saturated at high Al_2O_3 concentration [Shao 2002]. The results also showed that the volume percentage of Al_2O_3 in Ni deposit decreased as the size of the Al_2O_3 nanoparticles decreased from 300 nm to 50 nm.

Kuo et al. investigated the effect of electrolyte dilution on Al_2O_3 nanoparticles incorporation into Ni deposit [Kuo 2004]. XRD showed that the volume percentage of Al_2O_3 increased from 8.37% to 26.78% when the concentration of Ni^{2+} was diluted from 1.27 M to 0.35 M because of decreased deposition of Ni. The volume percentage of Al_2O_3 decreased with further dilution because of hydrogen formation.

Bath agitation also influences the incorporation process as it helps suspend the nanoparticles in the electrolyte and transport the nanoparticles to the cathode. Increased agitation generally enhances the amount of nanoparticles in the deposit while excessive agitation may decrease the incorporation as vigorous hydrodynamic forces can wash off entrapped nanoparticles [Low 2006].

Recent investigations by different researcher showed that magnetic field can affect the incorporation content as well. Al_2O_3 nanoparticles were codeposited with Ni while various magnetic flux densities were applied [Feng 2007, Wang 2009a]. Composition analysis showed that weight percentage of Al_2O_3 in the deposited nanocomposite increased with increasing magnetic flux density, possibly because of an enhanced mass transfer.

2.2.2.2 Theoretical Work

Theoretical models have been proposed to predict the amount of incorporated nanoparticles given experimental conditions [Guglielmi 1972, Celis 1987, Fransaer 1992, Vereecken 2000]. It is generally agreed that the codeposition process consists of three main steps [Thiemig 2008]:

- (I) Transport of particles from the bulk electrolyte to the cathode by means of various mechanisms, e.g., convection, diffusion and electrophoresis
- (II) Particle adsorption at the cathode
- (III) Irreversible entrapment of the particles in the deposit

The models [Guglielmi 1972, Celis 1987, Fransaer 1992, Vereecken 2000] describe the codeposition process with different physics and work only for limited experimental conditions. The codeposition mechanisms are still not completely understood yet because many factors (e.g. the characteristics of nanoparticles, electrolyte, current, and hydrodynamics) interact with each other, making the codeposition process rather complex to describe. The existing models are still unable to predict the deposit composition *a priori* for a given system and experimental conditions.

2.2.3 Dispersion of Nanoparticles

Research on electrocodeposition of nanocomposites has always been extensive since the concept was introduced. Most of the research effort has been focused on measurement and prediction of the amount of the incorporated nanoparticles because it significantly affects the material properties. It is worth noting that material properties of nanocomposites are also determined by another equally important but generally overlooked factor, the dispersion of

nanoparticles. For example, given the same amount of reinforcements in composite, smaller nanoparticles provide more significant Orowan strengthening and Zener pinning effects than their agglomerates for much more enhanced materials properties. Therefore, more attention needs to be drawn to the dispersion of nanoparticles in the deposit to obtain full benefit from nanosized reinforcements. Since nanoparticles tend to form agglomerates in most environments due to their high surface energy and large specific surface area, it is necessary to apply effective dispersion techniques, such as dilution of electrolyte, surfactants, and ultrasonication before and/or during electrocodeposition.

Self-dispersion of nanoparticles in aqueous solutions can be enabled by electric double layers (EDL) around the nanoparticles because EDL can generate a repulsive force between nanoparticles. However, the self-dispersion effect by EDL can be inhibited by electrolyte because high ionic concentration in a solution can screen the EDL effect. Therefore, dilution of electrolyte is generally beneficial to achieve nanoparticle dispersion. Surfactants can also be engineered to adsorb on nanoparticles and provide electrostatic repulsion or steric interference between nanoparticles to enhance dispersion. In addition to above-mentioned chemical methods, ultrasonication can be applied as well to reduce agglomeration because the shock wave generated by ultrasonic cavitation can break up nanoparticle clusters. Existing research on dispersion of Al_2O_3 nanoparticles in Ni deposit will be particularly reviewed since Ni/Al_2O_3 is the most studied material system.

Kuo et al. studied the dispersion of Al_2O_3 nanoparticles (80 nm) in the nickel deposit obtained by direct current (DC) electrodeposition in a nickel sulfamate bath [Kuo 2004]. Dynamic light scattering (DLS) measurements showed that the agglomeration size in the electrolyte was

1109 nm without any treatment while the agglomeration size was reduced to 280 nm and 448 nm respectively using ultrasonication and surfactants (cetyltrimethyl ammonium bromide, CTAB). From SEM observations, the nanoparticle agglomerates in the deposited nanocomposites also became smaller by ultrasonication and surfactants. The volume percentages of Al_2O_3 in nanocomposites increased as well by applying ultrasonication and surfactants. It is interesting to note that the nanoparticles remained fairly dispersed during the electrocodeposition for 8 h after only 40 minutes ultrasonication. The agglomeration size in the electrolyte can be further reduced from 280 nm to 178 nm when Ni^{2+} was diluted from 1.27 M to 0.20 M. SEM images showed the size of the nanoparticle clusters in the deposit was not significantly changed by dilution while the volume percentage of incorporated nanoparticles was increased tremendously.

Qu et al. studied the effect of ultrasonication during electrocodeposition of Ni/Al_2O_3 using pulsed current in a sulfamate bath [Qu 2004]. SEM study showed ultrasonication slightly reduced agglomeration but significantly reduced the amount of Al_2O_3 nano-whiskers incorporated in the composite coatings.

Chen et al. reported the effect of surfactants on dispersion and incorporation of Al_2O_3 nanoparticles (0.8 μm) in electrocodeposition of Ni/Al_2O_3 [Chen 2006]. Various concentrations of surfactants, hexadecylpyridinium bromide (HPB), were added to the Watts bath before electrocodeposition. Measurements showed that the zeta potential of the suspended nanoparticles increased from about −5 mV to +20 mV when the HPB concentration increased from 0 to 300 mg/L. SEM observation of Ni/Al_2O_3 deposits showed the Al_2O_3 nanoparticles were slightly less agglomerated with addition of HPB, while EDS analysis showed Al_2O_3 content increased significantly from 8.6 vol. % to 14.7 vol. %.

In the study by Bund et al., the dispersion of Al_2O_3 nanoparticles (with a diameter of 13 nm) was found strongly dependent on the bath composition [Bund 2007]. Two kinds of electroplating baths were used: acidic sulfamate and alkaline pyrophosphate. The acidic bath contains 1.08 M $Ni(NH_2SO_3)_2$, 0.04 M $NiCl_2$, and 0.65 M H_3BO_3 while the alkaline bath contains 0.30 M $NiSO_4$, 0.75 M $K_4P_2O_7$, and 0.12 M $C_6H_8O_7$. SEM study showed that the alkaline bath produced Ni/Al_2O_3 of higher quality with Al_2O_3 well dispersed and uniformly distributed than the acidic sulfamate bath. The size of Al_2O_3 nanoparticle agglomerates from the alkaline bath was about 100 nm while that from acidic bath was about 200 nm.

Zheng et al. studied the effect of ultrasonic power on dispersion and incorporation of Al_2O_3 nanoparticles in Zn-Ni deposits by applying ultrasonication at various power during electrocodeposition in 120 mL cell of $NiCl_2$ and $ZnCl_2$. SEM showed that the Al_2O_3 nanoparticles were well dispersed when the ultrasonic power was increased to 0.7 W/cm^2. When the ultrasonic power was further increased to 0.9 W/cm^2, many nanosized and microsized pores were formed possibly because of detachment of loosely bonded Al_2O_3 nanoparticles. EDS analysis also showed that the ultrasonic power significantly influenced the incorporation amount of Al_2O_3 nanoparticles. The weight percentage of Al_2O_3 in the deposit increased from 4.5 wt. % to 11.2 wt. % when the ultrasonic power increased from 0 to 0.9 W/cm^2 while a further increase in ultrasonic power reduced the Al_2O_3 incorporation [Zheng 2008].

García-Lecina et al. conducted a comparative study on the effect of mechanical and ultrasonic agitation on electrodeposited Ni/Al_2O_3 nanocomposite coatings with Watts baths [García-Lecina 2012]. TEM images showed that the size of the Al_2O_3 nanoparticles used for reinforcements varied from 20 nm to 150 nm with a mean diameter of 50 nm. Acoustic

spectroscopy measurements were made to characterize the size distribution of nanoparticle clusters in the electrolytes after magnetic stirring and ultrasonic treatment. After magnetic stirring for 24 h, the particle size distribution (PSD) showed two maxima at 205 ± 19 nm and 5.8 ± 0.539 μm while the maxima shifted to 109 ± 7 nm and 1 ± 0.062 μm after an additional ultrasonic processing. The results indicated ultrasonic treatment could effectively break up agglomerates in the electrolyte. Nonetheless, the deagglomeration effect of ultrasonication was transitory: the PSD shifted back one hour after ultrasonication. The effects of mechanical and ultrasonic agitation during deposition on the microstructures were studied by SEM and TEM. SEM micrographs of the sample cross sections showed the Al_2O_3 nanoparticles in the sample produced by ultrasonic agitation were more dispersed than that by magnetic stirring. Individual nanoparticles were observed by TEM in the Ni/Al_2O_3 after ultrasonic processing. The results indicated ultrasonication is more effective for deagglomeration than magnetic stirring. In addition, EDS analysis showed that ultrasonic agitation also enhanced the incorporation content when compared with magnetic stirring.

2.2.4 Summary

Electrocodeposition of nanocomposites is gaining more and more attention in the field of material science because of its low cost and widespread applications. The technique has been used to fabricate various material systems successfully. Current and past research has been focused on the improvement of incorporation content of nanoparticles in the deposits to achieve enhanced properties. Experimental work showed the amount of reinforcements in codeposited nanocomposites can be increased by applying pulse plating techniques, increasing the nanoparticle content in the electrolyte, and improving the hydrodynamics of the plating cell. Theoretical models

has been proposed to predict the amount of nanoparticles embedded in the deposits, but the existing models would work only for limited conditions and are unable to predict the incorporation content *a priori*. More comprehensive models are needed to provide insights and guidance for experiments or practical applications.

Unfortunately, less attention has been paid to the dispersion of nanoparticles in the plating bath and final deposits, although dispersion is a factor as important as the nanoparticle content to determine the material properties of the deposited nanocomposites. Several techniques have been experimentally tested to effectively improve dispersion: ultrasonication, electrolyte dilution and surfactants. When compared with the latter two techniques, ultrasonication has the potential for broad applications because it does not alter electrolyte composition and thus avoids possible undesirable effects. However, the experimental results on the effects of ultrasonication are inconsistent and sometimes even contradictory. Therefore, more study is necessary to better understand the ultrasonication effect before or during electrocodeposition. Measurements of zeta potential and agglomeration size of nanoparticles in electrolyte by dynamic light scattering (DLS) can be insightful to understand the agglomeration and dispersion behavior of the suspended nanoparticles. Eventually, a theoretical model on the dispersion of nanoparticles in electrolyte can be very useful.

2.3 LASER PROCESSING OF METAL MATRIX NANOCOMPOSITES

There exists little literature about laser melting of prefabricated metal matrix nanocomposite (MMNC). However, laser melting processes have been used to fabricate MMNC coatings on various substrates. Among all laser melting processes for MMNCs, laser surface

alloying (LSA) and laser cladding (LC) are the most studied and thus will be the focus of this review. In addition, selective laser sintering/melting (SLS/SLM) is becoming more and more popular because it enables rapid fabrication of three-dimensional parts with any complex geometries and configurations directly from powders. Since nanocomposites promise to offer significantly enhanced material properties, nanocomposite concept was recently introduced in SLM process to fabricate bulk MMNCs and investigate the potential benefits. Thus SLM of MMNCs will be especially reviewed.

2.3.1 Laser Surface Alloying

2.3.1.1 Process Description

Laser surface alloying (LSA) involves surface melting and rapid solidification along with material added on or to the surface. The added material is mixed into the surface during the melting. The composition and microstructure of the surface layer are modified because of the additional material mixed and rapid solidification. The result can be a thin hardened or even functional layer on the surface [Ready 2001]. The additional material can be added in various ways [Steen 2010]:

- electroplating
- vacuum evaporation
- preplaced powder coating
- thin foil application
- ion implantation

- diffusion, e.g., boronising
- powder blowing
- wire feeding
- reactive gas shroud, e.g., C_2H_2 in Ar or N_2

It is possible to add elements such as boron, nitrogen, carbon, chromium, silicon, and nickel to the surface, thus specific techniques developed accordingly, such as laser boronising, laser nitriding, and laser carbonization, etc. LSA is capable of producing a wide variety of surface alloys and composites. The high solidification rate even allows some metastable alloys to be formed on the substrate surface [Steen 2010]. Enabled by laser melting, it shares many advantages with other laser materials processing technologies:

- It can selectively strengthen specified areas with high precision.
- It requires no physical contact with the substrate.
- It can be performed rapidly.
- It offers high reliability and reproducibility.

The major application of LSA is to enhance the surface wear and corrosion resistance of components. Recently, LSA also finds applications in the biomedical field to improve the biocompatibility and bioactivity of implants. LSA has been used to produce nanocomposite coating with great potential for broad applications. This review will particularly focus on LSA for fabrication of nanocomposite coatings.

2.3.1.2 Nanocomposite Coating via Laser Surface Alloying

In 2000, Wu and Hong reported a composite coating synthesized by laser alloying of Zr nanoparticles on an austenite stainless steel surface [Wu 2000]. An organic solution containing Zr nanoparticles (6 nm) was sprayed on the stainless steel surface for a layer thickness of 220 nm. Laser irradiation was then applied using a pulsed Nd:YAG laser with a wavelength of 1.06 μm, a pulse duration of 180 ns, a frequency of 12 kHz, an average output power of 250 W and a spot size of 200 μm. The optical image of the cross section of the alloyed sample showed a maximum melt depth of about 60 μm, while the energy dispersive spectroscopy (EDS) analysis showed Zr was presented only up to 16 μm below the top surface and the Zr distribution was discontinuous and uninform, indicating Zr was not fully mixed in the melt pool possibly due to the short effective melting period. Amorphous phases appeared in the Zr-containing zone and were often present near the austenite dendrites. Nanoindentation tests showed significant improvements in hardness from 1.8–2.1 GPa of the substrate to 2.6–3.2 GPa of the melt pool without Zr due to the refinement of the microstructure, and further to 3.8–4.6 GPa of amorphous layer. Wear-corrosion experiments showed the wear-corrosion rates were 7.3×10^{-5} g/mm^2-h and 21.4×10^{-5} g/mm^2-h for the alloyed and original surface, respectively.

Choudhury et al. reported the fabrication of *in-situ* nanocomposite coating on a medium carbon steel substrate where the reinforcements were synthesized from chemical reaction of the preplaced powders [Choudhury 2007]. $Ti(OH)_4$ nanoparticles, B_4C powder (800–1200 mesh), and Ti6Al4V powder (100–325 mesh) were mechanical mixed in acetone and pasted on the substrate. Laser surface alloying was carried out using a diode laser (at 808 nm and 940 nm wavelengths) with a power of 1200 W and scan speeds of 0.5, 1.25, 5 and 10 mm/s. The focused spot was

rectangular with a dimension of 2.5 mm × 3.5mm. SEM and XRD analysis showed TiB nanoparticles and FeB microparticles were formed and dispersed in Fe + Fe_2B matrix after laser irradiation. With the *in-situ* reinforcements, the microhardness and wear resistance of the nanocomposite coating were significantly improved when compared with the original substrate. The researchers also fabricated coatings on medium carbon steel and stainless steel substrates using a similar method except that TiO_2 nanoparticles and B_4C powder were used [Choudhury 2008]. In this case, both TiB_2 and TiB nanoparticles were identified. High resolution TEM showed the TiB2 and TiB nanoparticles were of different size ranges, 200–500 nm, 20 nm and 5–10 nm. Other borides and carbides of micron size were also found dispersed in the matrix. Again, the microhardness and wear resistance were improved with the nanocomposite coatings.

2.3.1.3 Summary on Laser Surface Alloying

Only a few studies on laser surface alloying of nanocomposites were reported. Perhaps it is difficult to incorporate the preplaced nanoparticles into the melt pool because nanoparticles prefer to remain along the interface between the molten metal and the protective gas. Despite of limited research, the addition of nanoparticles has successfully refined the microstructure and improved the mechanical properties of substrates.

2.3.2 Laser Cladding

2.3.2.1 Process Description

Laser cladding (LC) is to melt a substrate surface with a laser and then continuously feed filler materials into the melt pool, thus forming a cladded layer (cladding). It is considered as a

welding of filler materials onto the substrate. The cladding mixes with the substrate in a minimal manner. This is in contrast to the case of laser surface alloying, in which the alloying material is generally thoroughly mixed with the surface matrix [Ready 2001]. Diluting the cladding metal with substrate is generally considered as a contamination of the cladding that would degrade its mechanical, corrosion or other properties [Steen 2010]. The filler can be in the form of wire, strip, or powder. Generally, a powder form is preferred, as it is easier to control for lower feed rates. The powder can be transported by an inert carrier gas or preplaced. LC offers optimum bonding, great flexibility, low distortion, and low thermal load on the substrate together with little need for post-treatment [Ready 2001]. LC finds great applications for improving wear resistance, corrosion resistance and bioactivity, and repairing critical parts. Research work on LC has been active since its invention. The review will focus on fabrication of nanocomposite coating via LC.

2.3.2.2 Nanocomposite Coating via Laser Cladding

Chen et al. reported the effect of WC nanoparticles (50–500 nm) and microparticles (3–5 μm) on the wear behavior of laser cladded Ni-based alloy coatings [Chen 2005, Chen 2008a]. The powder mixtures were preplaced on carbon steel substrates, followed by laser cladding using a CO_2 laser with a power of 1.6 kW, a beam diameter of 4 mm and a scan speed of 240 mm/min in a protective nitrogen atmosphere. Although WC particles were agglomerated, the sliding wear tests showed the wear resistance was improved by WC. The enhancement from WC nanoparticles was slightly higher than that from WC microparticles. Interestingly, the best wear resistance was obtained by combining both WC nanoparticles and microparticles.

Al_2O_3 nanoparticles (80–180 nm) and Fe powder (5–200 μm) were used for laser cladding to fabricate nanocomposite coatings on iron-based substrates [Yu 2006]. Laser cladding was carried out using a CO_2 laser in the argon shielding atmosphere after preplacing the powder mixture. A rectangle laser beam spot of 15 mm × 2 mm was used. The optimum processing parameters were found to be the laser beam power of 2.5 kW at the scan speed of 1.5 mm/s. Vickers hardness tests showed the microhardness of coating was significantly higher than the substrate. Wear tests showed the wear rate (weight loss) decreased as the percentage of Al_2O_3 in the coating increased from 4 wt. % to 8 wt. %.

Li et al. studied the effect of Y_2O_3 nanoparticles on the microstructure of Co-based coatings [Li 2006]. Mixtures of Co-based alloy powder (53–153 μm) and Y_2O_3 nanoparticles (0.2–1.0 wt. %, 10–30 nm) were preplaced onto a Ni-based alloy plate and scanned with a CO_2 laser. The laser parameters were 2.0 kW laser power, 4.5 mm beam diameter and 250 mm/min scan speed under the protection of argon gas. In addition to the common γ-Co and $Cr_{23}C_6$ phases, the addition of Y_2O_3 nanoparticles resulted in a new ε-Co phase. It was proposed that the low thermal conductivity of Y_2O_3 reduced the cooling rate so that the equilibrium ε-Co phase formed. The Co-based alloy matrix formed columnar dendrite due to the rapid directional solidification without Y_2O_3 while multi-orientation dendrites or even equiaxed grains formed with the addition of Y_2O_3 as heterogeneous nuclei. Later on, similar phenomena, i.e., new phase formation and microstructure refinement, were also observed by the introduction of CeO_2 nanoparticles into Ni-based coatings [Zhang 2008]. The microhardness and wear resistance of the coatings are greatly improved by the CeO_2 powder addition, and the improvements were more significant with the addition of CeO_2 nanoparticles than microparticles. Wang et al. also studied the thermal shock resistance of CeO_2

nanoparticles reinforced Ni alloy coatings [Wang 2010a], which was much higher than the Ni alloy coating.

In Wang and Yan et al.'s work, Ni nanoparticles were used to improve the interfacial compatibility between lubrication enhancement phases (WS_2 and h-BN) and the Ni-based alloy matrix to fabricate self-lubricating composite [Wang 2008, Yan 2010]. It was known that the lubricants such as WS_2 and h-BN tend to decompose at high temperature and react with the base alloy. Therefore, Ni nanoparticles (10–40 nm) were mixed with the WS_2 (880 nm) or h-BN (≤100 nm) powder by ball milling to prepare Ni-encapsulated lubrication enhancements, which were then mixed with the base Ni alloy and laser cladded onto medium carbon steel substrates. Laser cladding was carried out using a pulsed Nd:YAG laser with a pulse width of 0.5 ms, a frequency of 60 Hz, a beam diameter of 3 mm, an average power of 350 W and 370 W and a scan speed of 120 mm/s and 240 mm/s. XRD analysis showed that WS_2 and h-BN decomposed less with Ni encapsulation. The coefficient of friction were reduced and the wear resistance were improved by the successful introduction of the lubricants.

Chen et al. investigated the feasibility of laser cladding of Al/SiC nanocomposites onto Mg alloy substrate [Chen 2008b]. Mixture of Al and SiC (40–60 nm) in a weight ratio of 3:1 were preplaced on the ZM5 alloy substrate and laser cladded using an Nd:YAG laser in argon atmosphere. The microhardness, wear resistance and corrosion resistance were improved by laser cladding.

Wang et al. studied the effect Al_2O_3 nanoparticles on the microstructure and performance of Ni-based coating [Wang 2009b, Wang 2010b]. Composite powders containing 0.5 wt. %, 1.0 wt. % and 1.5 wt. % Al_2O_3 nanoparticles (20 nm) were pre-coated on Ni-based superalloy,

followed by laser cladding using a CO_2 laser under nitrogen protection. The laser power was 1 kW and the spot diameter was 2 mm while the scan speed was 5 mm/s. The microstructure of the matrix was refined with the addition of Al_2O_3 nanoparticles because the nanoparticles induced heterogeneous nucleation and hindered grain growth. XRD showed that the Al_2O_3 nanoparticles prevented the formation of α-Cr phase. Modified by Al_2O_3 nanoparticles, cracking of the coating was reduced because Al_2O_3 nanoparticles decreased the temperature gradient in the cladding process. The oxidation resistance was significantly improved as well, which was likely due to the acceleration of a selective oxidation of Cr, inhibition of volatilization of Cr_2O_3 scales, improvement of the self-repairing capability of oxide scale, and blocking of micro channels for oxygen penetration.

Zhang et al. reported a biphasic calcium phosphate (BCP)/Ti nanocomposite coating to improve the biocompatibility of Ti6Al4V implants [Zhang 2011]. Hydroxyapatite (HA) nanoparticles and Ti nanoparticles were mixed into polyvinyl alcohol (PVA) and dip coated on a Ti6Al4V substrate. Laser cladding was carried out using an Nd:YAG laser with a power of 12–30 W, a scan speed of 0.5–2 mm/s, and a laser beam radius of 0.3–1 mm under helium protection. SEM analysis showed the morphology of the HA nanoparticles remained the same after laser processing while the Ti nanoparticles melted, merged, and encapsulated HA nanoparticles. XRD identified β-tricalcium phosphate (β-TCP) phase formed after laser processing due to a partial decomposition of HA into β-TCP and thus formation of BCP, i.e., a mixture of HA and β-TCP. XRD analysis also confirmed the evaporation of PVA after laser irradiation. Scratch tests showed the interfacial bonding strength of the gradient multilayer HA/Ti coatings was more than twice of that of the commercial plasma sprayed coating. Preliminary cell culture studies showed that the BCP/Ti nanocomposite coating supported the adhesion and proliferation of cells.

Ti_3Al matrix nanocomposite coatings were fabricated on Ti6Al4V substrates [Li 2012a]. Powder mixtures consisting of Al_3Ti (50–150 μm), TiB_2 (150–250 μm), Al_2O_3 (150–250 μm) and Y_2O_3 nanoparticles (10–200 nm) were preplaced on the substrates and then underwent laser cladding under argon protection. The laser power was 700–1150 W, the scan speed was 2–5 mm/s, and the spot diameter was 4 mm. XRD analysis on the coatings identified the following phases: Ti_3Al, TiB_2, SiO_2, TiO_2, Y_2O_3 and Al_2O_3. Ti_3Al was the major phase, which was formed from the reaction of the introduced Al_3Ti and Ti from the substrates. Y_2O_3 nanoparticles refined the precipitations of TiB_2 and Al_2O_3 because of the inhibition of crystalline growth. Due to the microstructure refinement and Orowan strengthening, the microhardness and wear resistance were significantly improved when compared with the original Ti6Al4V substrate. CeO_2 nanoparticles reinforced Ti_3Al/γ-Ni matrix coating was also investigated, and similar microstructure refinement and properties enhancement were observed [Li 2012b].

2.3.2.3 Summary on Laser Cladding

The existing research on nanocomposite coating via LC mainly focuses on the microstructure characterization and property enhancement. Refinement of primary phases and precipitation phases in some systems were observed. The introduced nanoparticles refined the matrix by increasing heterogeneous nucleation sites and inhibiting the crystal growth. Due to the microstructure refinement and the enhancement of nanoparticles, improvements of material properties were often achieved, including hardness, wear resistance, oxidation resistance, thermal shock resistance, corrosion resistance, and crack resistance.

2.3.3 Selective Laser Melting

2.3.3.1 Process Description

Selective laser sintering/melting (SLS/SLM) is one of the additive manufacturing processes that enable rapid fabrication of complex three-dimensional parts. SLS/SLM builds an object layer by layer: a thin layer of powder is placed on a platen and a pattern is drawn by laser to selectively bond the powder, after which another layer is laid on top and the process is repeated until the object is built [Ready 2001, Steen 2010]. One major difference between SLS and SLM is that the appellation of SLM is reserved for metallic materials [Kruth 2005].

Additive manufacturing has many advantages over the traditional subtractive processes, such as great flexibility, ability to build complex shapes, and rapid prototyping, etc. In addition, SLS/SLM enables rapid solidification and thus ultrafine microstructure for improved material properties. Recently, SLS/SLM process has been investigated for fabrication of nanocomposites since nanocomposites promise to provide enhanced material properties. While extensive research has been reported on SLS of polymer or ceramic matrix nanocomposites, this review will particularly focus on SLM of metal matrix nanocomposites (MMNCs).

2.3.3.2 Bulk Metal Matrix Nanocomposite via Selective Laser Melting

Gu et al. reported their experimental work on fabrication and microstructure characterization of TiC reinforced Ti-Al composite by ball milling and SLM [Gu 2009]. Micro powders consisted of 50 at. % Ti (30 μm), 25 at. % Al (16 μm), and 25 at. % graphite (30 μm) were mechanically alloyed with a ball mill. TiC reinforced TiAl composite was expected to form

with a molar ratio of 1:1. XRD analysis showed TiC and Ti(Al) solid solution were formed: TiC nanoparticles (20 nm) were dispersed in Ti(Al) micro powder (0.8 μm). The nanocomposite powder was used for SLM using a CW Gaussian CO_2 laser with a wavelength of 10.6 μm. Based on a parametric study, suitable process parameters were found: a spot size of 0.30 mm, a power of 800 W, a scan speed of 0.10 m/s and a scan line spacing of 0.15 mm. After laser processing, $TiAl_3$ and Ti_3AlC_2 were formed as the matrix instead of TiAl because $TiAl_3$ precipitated preferably, and TiAl reacted with TiC and turned into Ti_3AlC_2. Eventually, TiC reinforced ($TiAl_3$ + Ti_3AlC_2) composite was fabricated via SLM. The $TiAl_3$ and Ti_3AlC_2 matrix was laminated with an axial length of 1.5 μm and a thickness of 0.25 μm, and the reinforcing TiC grew as well, but still below 1 μm. The report was focused on the microstructure characterization and evolution mechanism. Although TiAl was not fabricated as expected, the process of the combination of ball milling and SLM is interesting.

Later on, Gu et al. fabricated TiC/Ti nanocomposites with the same method, the combination of ball milling and SLM [Gu 2010, Gu 2011, Gu 2012, Gu 2014]. The starting components included 15 wt. % TiC powder (1.5 μm) and 85 wt. % Ti powder (45 μm). Ti/TiC nanocomposite powder was formed after ball milling with a uniform particle size of 5.8 μm. TEM showed the TiC nanoparticles with a mean size below 50 nm were uniformly dispersed in the Ti matrix. SLM was conducted under argon protection using an Nd:YAG laser (1.064 μm) with a spot size of 70 μm, a power of 100 W, a scan speed of 0.1–0.4 m/s and a hatch spacing of 140 μm. Density measurements showed that the densification level of a SLMed part increases as the scan speed decreases, i.e., the laser energy density increases. SEM observations revealed that the TiC phases formed lamellar structures after SLM with a thickness below 100 nm, different from the milled particulate structures. The lamellar TiC phase slightly coarsened and aggregated with

decreasing scan speed, i.e., increasing energy density. It was believed the TiC nanoparticles melt and precipitated as the lamellar structures. Tribological study showed that the coefficient of friction and wear rate first decreased and then increases with increasing scan speed. The scan speed was optimized at the combination of a sound densification and fine reinforcing nanostructures. In addition, mechanical mixed Ti powder (22.5 μm) and TiC powder (50 nm) were also used for SLM. The densification behavior and tribological properties from mechanical mixed powder were slightly worse than those from ball milled powder.

Biedunkiewicz and Figiel et al. fabricated TiC reinforced stainless steel SS 316L nanocomposites with ball milling and SLM, and demonstrated increased hardness and oxidation resistance as compared with the reference sample prepared from 316L steel powder [Biedunkiewicz 2011, Figiel 2012, Biedunkiewicz 2013].

Dadbakhsh and Hao et al. investigated the feasibility of *in-situ* composites on different Al alloys (Al, AlMg1SiCu and AlSi10Mg) with SLM method [Dadbakhsh 2012]. Each alloy powder (40 μm) was mechanical mixed with 15 wt. % Fe_2O_3 powder (below 53 μm). After SLM, *in-situ* nanoparticles formed, including Al-Fe intermetallics, α-Al_2O_3, Al-Fe-Si intermetallics and Si crystals. The hardness of these composites was improved when compared with conventionally manufactured (e.g., casting) counterparts without Fe_2O_3 because of both reinforcing effect of nanoparticles and microstructure refinement from rapid solidification.

SLM was also used to prepare SiC reinforced Fe matrix composites [Song 2013]. Fe powder with an average particle size of 20 μm, and hierarchical SiC powder (micro- and nano-sized) with an average particle size of about 0.7 μm were used. SLM was carried out using a continuous-wave ytterbium fiber laser (1064–1100 nm) with a laser beam diameter of 34 μm, a

laser power of 100 W, a scan speed of 0.33 m/s, and a scan line spacing of 40 um. SEM observations of the surface of the SLMed pure Fe part revealed the solidified regular melt front, suggesting complete melting and significant melt pool flow occurred. However, the melt front features did not show up on the SLMed Fe/SiC. It was believed that the melt pool flow was less intensive because the addition of SiC increased the viscosity of the melt pool. TEM and XRD showed the SiC particles partially reacted with Fe and formed Fe_3C, and the rest retained their original micro- and nano-size. Fe matrix was also modified by SiC and nanocrystalline and amorphous Fe were observed. Tensile tests showed the strength of the SLMed Fe/SiC is much higher than that of the SLMed pure Fe.

2.3.3.3 Summary on Selective Laser Melting

Since both SLM and nanocomposites are new concepts, research on fabrication of bulk nanocomposites through SLM just emerged as a new research area with both opportunities and challenges. Although enhanced material properties were demonstrated, problems such as reaction, growth and agglomeration of nanoparticles were encountered as well, where significant research is thus necessary.

2.3.4 Summary

Research progress on laser melting of metal matrix nanocomposites (MMNCs) was reviewed. Laser surface alloying (LSA), laser cladding (LC) and selective laser melting (SLM) are the most important laser melting processes for fabrication of MMNCs currently. There is little research on LSA of nanocomposites because of the difficulty in mixing nanoparticles into the melt pool. Fabrication of bulk MMNCs using SLM just emerged, thus there is little literature. Among

the three technologies, LC is the most studied, in which microstructure refinement and property enhancement gained from addition of nanoparticles are frequently observed.

Overall, existing literature shows that laser melting based manufacturing of MMNCs is promising because of enhanced material properties and great flexibility the process offers. However, there remain numerous unresolved issues. Agglomeration of nanoparticles has been often observed, but there is little research on how to improve the distribution and dispersion of nanoparticles. Most past research focused on the material properties, but the underlining physics of the process was not studied, especially the effects of nanoparticles on laser melting process. For example, nanoparticles could change laser-mater interaction (e.g., absorptivity), thermophysical properties (e.g., surface tension, viscosity, and thermal conductivity), and thus the dynamics of the melt pool flow. All these effects introduced by nanoparticles need intensive study. The fundamental knowledge will provide valuable insights and guidance for various laser manufacturing processes for MMNCs.

2.4 FLUID FLOWS IN A LASER-INDUCED MELT POOL

Melt pool flow plays a crucial role in laser manufacturing processes. For example, the melt pool flow in laser welding determines the penetration depth and thus the welding quality. In laser polishing, the resultant surface topography, i.e., the surface finish, is also dictated by the dynamics of melt pool flow. Since nanoparticles can modify the thermophysical properties of base metals and alloys, it is highly possible to control the melt pool flow and thus overcome fundamental limits that exist in some current laser processing techniques. In this section, existing work on melt pool

flow in laser melting will be reviewed to lay a solid foundation for a better understanding of melt pool dynamics.

Previous study suggests that there exist at least two fluid flow patterns in a laser-induced melt pool: damped capillary oscillations and thermocapillary flows. Dependent on the material properties and laser parameters, one melt pool flow may dominate another. Given the same material, damped capillary oscillations are usually associated with a relatively low laser fluence while thermocapillary flows often occur at a high laser fluence. Two laser melting regimes can be defined according to the dominant melt pool flow: *Capillary Regime* where capillary oscillations dominate and *Thermocapillary Regime* where thermocapillary flows dominate. The dynamics of these two fluid patterns are reviewed as follows.

2.4.1 Damped Capillary Oscillations

When a laser irradiates and melts a surface with asperities, the surface tension drives the surface asperities to oscillate, and the amplitudes of the oscillations decay due to viscous dissipation. This kind of fluid flow is called damped capillary oscillation, which is schematically depicted in Figure 2-1. Landau and Lifshitz [Landau 1959] modeled the oscillatory motion of a sinusoidal wave with a small amplitude-to-wavelength ratio in a viscous fluid. The model was further developed for prediction of surface topography that resulted from laser melting [Perry 2009a, Vadali 2012]. The oscillation frequency ω is predicted as:

$$\omega^2 = \frac{\sigma \kappa^3}{\rho} tanh(\kappa h) \qquad (2-1)$$

where σ is the surface tension, ρ is the density, h is the depth of the liquid, and κ is the wave number of the oscillation which is given as:

$$\kappa = \frac{2\pi}{\lambda} \qquad (2-2)$$

where λ is the wavelength of the oscillation. The amplitude ζ of the oscillatory wave decays exponentially with time:

$$\zeta(t) = \zeta(0)e^{-\gamma t} \qquad (2-3)$$

where γ is the damping coefficient which is given as:

$$\gamma = \frac{2\mu\kappa^2}{\rho} \qquad (2-4)$$

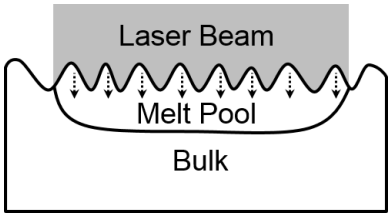

Figure 2-1 Schematics of damped capillary oscillation

The above model works only for perfect sinusoidal waves. However, a surface with random asperities can be decomposed into sinusoidal waves by the Fourier analysis such that the above model can be applied. As the model predicts, the amplitude of an oscillation is reduced due to viscous damping. This phenomenon has inspired a laser-based surface smoothening technology, i.e., laser polishing. The resultant surface topography is dependent on the material properties (the density and viscosity), the original surface condition (the wave number), and the process parameter (melt duration).

2.4.2 Thermocapillary Flows

In addition to capillary oscillations, thermocapillary or Marangoni flows can occur in a laser-induced melt pool as a result of temperature gradient and consequent surface tension gradient. The temperature of the melt pool is higher in the inner part than the outer part because of outward heat transfer. The temperature gradient can result in a surface tension gradient since surface tension σ is a function of temperature T ($d\sigma/dT$ is called surface tension coefficient). The surface tension gradient will further induce a surface flow toward the high surface tension region if it overcomes the viscous force, which usually happens at relative high laser fluence given the same material.

For most liquid metals, the surface tension coefficient is negative, i.e., surface tension increases as temperature decreases [Smithells 2004]. In this case, thermocapillary flow is radially outward thus creating a crater at the center and a rim at the outer perimeter of the melt pool as shown in Figure 2-2. Thermocapillary flows not only smooth the original asperities but also introduce ripple structures on a surface.

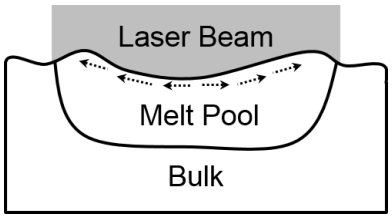

Figure 2-2 Schematics of thermocapillary flow

Thermocapillary flow has been extensively studied in the field of welding since Heiple and Roper [Heiple 1982] used it to explain why a little minor element could significantly change the weld pool depth. It was proposed that the minor elements could serve as surface active agents which changed the sign of surface tension coefficient and thus the direction of the flow. Kou and Sun [Kou 1985] developed a numerical model of Marangoni flow by coupling heat transfer and

fluid flow equations. A steady-state two-dimensional heat transfer and fluid flow model was built. The enthalpy method was used to deal with the phase change in heat transfer equation. Similarly, the effective viscosity method was introduced to solve the equation of motion to cover both solid and liquid phases within one computational domain. The temperature and velocity fields were obtained from the coupled model. Three driving forces for fluid flow were considered: buoyancy force, electromagnetic force and surface tension gradient. It was found that surface tension gradient had much more significant effects of on fluid flow than buoyancy. The limitation of this work was that it assumed a non-deformable surface. In a later work by Tsai and Kou [Tsai 1989], a steady-state model assuming a free surface was developed. Not only the temperature and velocity fields were obtained but also the deformation of the weld pool surface was predicted from the model. Besides, it was concluded that the weld pool depth can be significantly overestimated assuming a non-deformable surface. Sim and Kim [Sim 2005] develop a transient model of thermocapillary flow during laser melting assuming a free surface. The deformations of the melt pool surface at different times were shown, but resolidification process was not included in the model and thus the solidified surface profile could not be estimated. In addition, the experimental validation of the simulation results lacked clarity.

A more comprehensive model which considered a free surface and took resolidification into account was recently developed [Ma 2013]. The surface profile and melt pool geometry predicted from the model agreed well with experimental observations (Figure 2-3). However, the numerical nature of the model requires long computing time. A simple yet reliable model of thermocapillary flow in a laser-induced melt pool needs to be developed to provide insights and guidance for laser melting processes. An analytical model is desired to directly demonstrate the dependence of thermocapillary flows on material properties and process parameters, and predict

the conditions for onset of thermocapillary flows and thus for transitions of the two laser melting regimes.

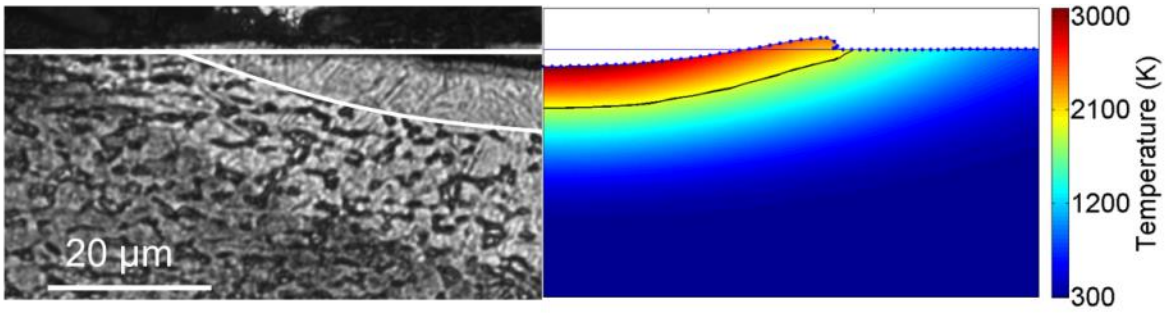

(a)

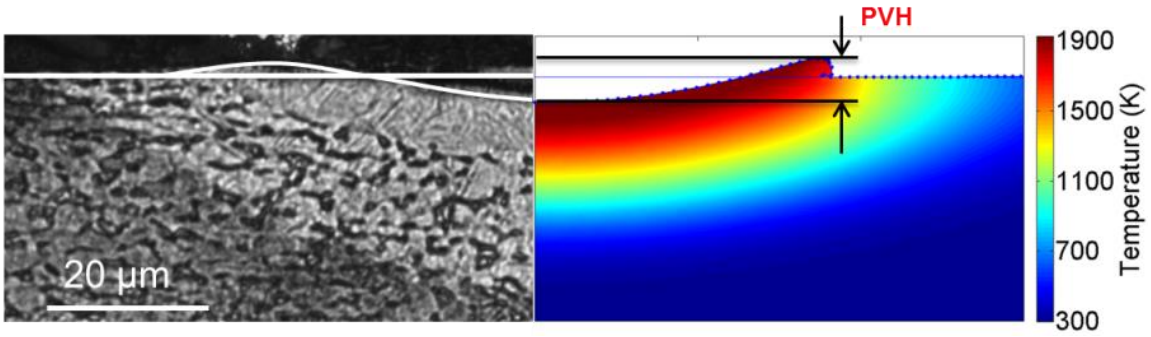

(b)

Figure 2-3 Comparison between numerical and experimental results: (a) melt pool shape at the end of the pulse; (b) solidified surface profile

2.4.3 Summary

Two types of melt pool flows were review: damped capillary oscillations and thermocapillary flows. Accordingly, two laser melting regimes were defined: capillary and thermocapillary regimes. The fluid flow model for damped capillary oscillations is well established while there is still a lack of understanding of thermocapillary flows. Extensive research has been conducted to develop numerical models to simulate thermocapillary flows, however, numerical models are limited by high computational cost and thus not effective enough for fast parameter selection as well as process control and automation. It is of great interest to construct a simple

analytical model to predict direct dependence of thermocapillary flows on material properties and process parameters.

2.5 LASER POLISHING

As a variant of laser melting, laser polishing will be used as an example to demonstrate the possibility to break the fundamental limits of laser processing techniques using the proposed methodology, i.e., control of melt pool dynamics by nanoparticles. An extensive literature review of the existing work on laser polishing will be presented. In addition, Bordatchev et al. also published a review paper on laser polishing of metallic surfaces [Bordatchev 2014], which is a good summary for the research progress on laser polishing.

Laser polishing is an emerging surface smoothening process suitable for micro/meso metallic parts, where conventional polishing techniques are impossible or uneconomic. In laser polishing, a laser is used to melt small spots on the surface of the part and then the surface asperities can be smoothed out by the fluid flow on or in the melt pool. Laser polishing is expected to have many advantages over conventional (mechanical or chemical) polishing [Mai 2004, Perry 2009b, Nüsser 2011, and Bordatchev 2014]:

- It can be easily automated to polish three-dimensional features.
- It can selectively polish specified areas.
- It requires no physical contact with the part.
- It produces clean surfaces with no residues.

- It affects only a thin layer of the surface, leaving the bulk of the part unaffected, especially with pulse laser micro polishing.
- It can be performed rapidly.
- It offers high reliability and reproducibility.

The laser used for polishing can be either continuous or pulsed, which are reviewed respectively in the following sections.

2.5.1 Continuous-wave Laser Polishing

In continuous-wave (CW) laser polishing, the laser continuously irradiates and scans across the surface of a part. The intensity of the heat input is determined by the laser power and beam size. The interaction time between the laser and the material and the resultant melt duration are controlled by the scan speed. CW laser polishing is known as an effective way to smooth large surface asperities with long wavelengths since the heat input and the spot size are generally larger for CW lasers than the pulsed lasers.

Continuous-wave (CW) laser polishing has been studied previously for various metals and even ceramics. Wang et al. [Wang 1998] polished silica rods with a 10.6 μm CO_2 laser. The peak-to-valley roughness was reduced from 2.0 μm to 0.05 μm. They proposed the polishing mechanism was laser melting of a very thin layer of material and the molten metal flowing under the action of surface tension. Later on, Ramos et al. [Ramos 2001] polished metallic surfaces using 1.06 μm neodymium-doped yttrium aluminum garnet (Nd:YAG) and 10.6 μm CO_2 lasers in CW mode. The samples were made of 420 stainless steel infiltrated with bronze by means of indirect selective

laser sintering (SLS). Surfaces with initial roughness Ra of 9.0 μm were polished down to 2.4 μm at 220 W and 1.7 mm/s using the Nd:YAG laser. With CO_2 laser, the Ra value was further reduced from 2.4 μm to 0.8 μm at 420 W and 4.5 mm/s. Lamikiz and Ukar et al. [Lamikiz 2006, Lamikiz 2007 and Ukar 2008] successfully polished a variety of metals using CW lasers, including medium carbon steel, tool steel and cast iron parts produced by milling and electric discharge machining (EDM), and SLSed 420 stainless steel infiltrated with bronze. The results showed clear roughness reductions in all cases. It was observed that no macro deformation of the parts due to CW laser polishing. Additionally, three-dimensional surface polishing was demonstrated on SLSed parts [Lamikiz 2007].

Hafiz et al. investigated the influence of overlap between laser beam tracks on surface finish by laser polishing [Hafiz 2012]. Laser polishing was experimented on H13 tool steel at different overlap percentages (80%, 90%, 95%, and 97.5%) with the same energy density. The surface finish improved as the overlap percentage increased from 80% to 95%, and then the surface quality deteriorated as the overlap further increased up to 97.5%. The reduction in the areal surface roughness Sa increased from 65.9% to 77.9% as the overlap increased from 80% to 95%. However, it is worth mentioning that the processing speed deceases as the overlap increases: the speed decreases by a factor of four as the overlap increases from 80% to 95%. Therefore, there is a trade-off between the surface finish and the processing speed. A suitable set of parameters should be selected based the applications.

Although CW laser polishing was proven to be an effective method to reduce surface roughness in macro parts, the large heat input limits the effectiveness of CW laser polishing, especially for micro parts. The temperature rise below the surface is a serious problem for many

microfabricated parts because it causes unacceptable heating of the substrate or distortion of the parts. Pulsed laser polishing was developed to smooth meso/micro parts because it melts the surface with a short laser pulse and allows it to cool down during laser OFF time.

2.5.2 Pulsed Laser Polishing

In pulsed laser polishing, the sample is heated by laser pulses one after another with a certain overlap between adjacent melt pools. The laser is generally pulsed at a short duty cycle (≤20%), thereby allowing longer time for cooling than heating to minimize an excess of heat input. Similar to CW laser polishing, the heat input intensity in pulsed laser polishing is determined by the power and the beam size. The difference is that the laser interaction time is directly the pulse duration, which can range from 1 ns to 10 μs. Pulsed laser polishing mitigates the problem of excessive heat input and reduces the heat affected zone such that it just smooths the surface and leaves the bulk part mostly unaffected.

2.5.2.1 Experimental Work

The earliest work on pulsed laser polishing can be traced back to the research on laser planarization in the late 1980s and early 1990s. Laser planarization was studied as a method to enable fabrication of planar interconnects on integrated circuits (ICs). In this application, after deposition of metal thin films on integrated circuits, a pulsed laser was used to briefly melt the surface and allow surface tension forces to smooth out the surface. Tuckerman and Weisberg [Tuckerman 1986] successfully planarized gold and aluminum line features using 504 nm dye lasers with 0.6 μs and 1.0 μs pulse widths. A lot of research on laser planarization was carried out after Tuckerman and Weisberg's work. Ong et al. [Ong 1991] reviewed the previous work and

discussed many factors that affected the process including metal reflectivity, metal thickness, contact profile, laser fluence, initial temperature, and so on. The effects of laser planarization on grain size, stress, specular reflectivity and electrical properties were also summarized.

Pulsed laser polishing is a latest evolution of laser planarization with broader applications. Bereznai et al. [Bereznai 2003] successfully polished titanium dental implant material using a 193 nm ArF excimer laser with 18 ns pulses. In the best case scenario, the surface roughness (Ra) was reduced from 256 nm to 25 nm. This result was important for dental applications because a smoother surface could avoid pathogenic plaque accumulation. Mai and Lim [Mai 2004] polished 304 stainless steel using a 532 nm Nd:YAG laser with a pulse width of 160 ns. Commercial 304 SS samples were irradiated at a 5 kHz repetition rate with 300–800 mJ/cm^2 energy density. AFM measurements revealed a decrease in Ra value from 195 nm to 75 nm. Further tests indicated that diffuse reflectivity was found to decrease from 38.6% to 15.6% after laser polishing. Furthermore, the laser polished samples also showed an improvement in homogeneity of microhardness distribution and resistance to pitting corrosion. Kim et al. [Kim 2004] polished tungsten thin films that had been deposited on Si using line shaped excimer lasers (248 nm KrF and 308 nm XeCl) with a pulse width of 20–30 ns. The length of the beam was 52 mm and the width of the beam was variable, which was used to control the fluence. As-grown tungsten films were polished with the 248 nm laser. The root-mean-squared (RMS) surface roughness was reduced from ~135 Å to ~82 Å with the best parameters. Tungsten films that had undergone chemical-mechanical polishing were also laser polished. The RMS roughness was reduced from ~27 Å to ~10 Å. This work showed that line beam could be used in semiconductor industry for large-scale production.

Perry et al. studied the effects of laser pulse width on laser polishing of microfabricated nickel with 1064 nm Nd:YAG laser [Perry 2009b]. Polishing with 300 ns and 650 ns pulse widths results in Ra values of 66 nm and 47 nm, respectively, corresponding to 30% and 50% reductions as compared with the original surface. It suggested that longer pulses result in smoother surfaces in PLμP. Nüsser et al. studied the influences of intensity distribution and pulse width [Nüsser 2011]. Tool steel (1.2343) was polished with two lasers, a 1030 nm fiber-coupled disk laser (TruMicro 7050) and a 1064 nm fiber-coupled rod laser (based on Rofin DY-series). It was shown that a flattop beam with homogeneous intensity distribution led to a lower surface roughness than a near-Gaussian beam. Also, a homogeneous, circular intensity distribution resulted in a lower surface roughness than a homogeneous, square distribution. Additionally, it is found that longer pulse width tended to achieve higher the maximal polishable spatial wavelength.

Vadali et al. studied the effect of pulse duration on pulsed laser polishing and discovered two distinct polishing mechanisms [Vadali 2013]. Pulsed laser polishing was carried out on micro end milled Ti6Al4V samples at three different pulse durations: 0.65 μs, 1.91 μs, and 3.60 μs. At the short pulse duration (0.65 μs), the melt pool flow was dominated by damped capillary oscillations. The resultant reduction in areal surface roughness Sa was only 21.3% but it did not leave artificial textures. The longer pulse durations (1.91 μs and 3.60 μs) resulted in much smoother surfaces, and the associated reductions in surface roughness are 68.6% and 72.4% respectively. Ripple textures were formed on the surface after laser melting in these cases, which are the signature of thermocapillary flows. This study suggests that the both types of melt pool flows (damped capillary oscillations and thermocapillary flows) can contribute to smoothening asperities and thus enable two distinct polishing regimes: capillary and thermocapillary regimes. Both regimes have advantages: capillary regime is good at smoothening high-frequency asperities

without leaving artificial textures while thermocapillary regime tends to offer higher reduction for originally rough surfaces with low-frequency asperities. Later on, combining the two polishing regimes, Pfefferkorn et al. reported a two-pass polishing process in which the first pass took advantage of thermocapillary flows in significantly reducing the surface roughness, and the second pass removes the residual process features [Pfefferkorn 2013]. Experimental results on micro end milled Ti6Al4V surfaces showed the first pass reduced the areal surface roughness by 50.0 %, and the second pass further decreased the roughness by 45.3%, resulting in a total reduction of 72.7%.

2.5.2.2 Theoretical Modeling

In pulsed laser polishing, the material usually cools down to the initial temperature (e.g., room temperature) before being heated by another laser pulse because of the short duty cycle (≤20%). In this case, modeling surface melting induced by a single laser pulse is sufficient to represent the process. Almost all of the existing modeling work on pulsed laser polishing only deals with surface melting in a single pulse because it is representative for the entire process.

Fourier-based fluid flow analysis was developed to model the laser planarization. A molten surface profile could be decomposed into Fourier components and that the actual surface profile would behave as the sum of the Fourier components. Based on the assumption of Couette flow, Tuckerman and Weisberg [Tuckerman 1986] derived a time constant that described the exponential decay of a topographic Fourier component. In later work by Marella et al. [Marella 1989], a more refined fluid flow model was solved analytically. In addition to the damping times for various wavenumbers, the oscillation frequencies were also predicted. In experiments on microfabricated line features of gold films, the reduction of amplitude and the change of phase in

the surface waves supported the predictions made from the model. Pendleton et al. [Pendleton 1993] calculated the melt duration in addition to damping time and concluded that the melt duration must exceed the damping time for a Fourier component to be sufficiently smoothed upon resolidification. Electroplated nickel samples were smoothed by applying 23 ns laser pulses. The spatial frequency spectra showed that laser polishing was more effective at higher spatial frequency, which agreed with the model.

Similar to laser planarization, Perry et al. [Perry 2009a] also used Fourier analysis to model PLμP. The fluid flow of each component was modeled as a stationary capillary wave assuming negligible convective flows. The analytical solution to a capillary wave was applied to calculate the damping time for each Fourier component [Landau 1959]:

$$t_d = \frac{\rho \lambda^2}{8\pi^2 \mu} \qquad (2-5)$$

where t_d is the damping time, ρ is the density, λ is the wavelength of the component and μ is the dynamic viscosity. If the melt duration is significantly longer than the damping time for a Fourier component, then the amplitude of this component can be expected to be significantly reduced upon resolidification. Conversely, little change in a Fourier component would be expected if the melt duration is significantly shorter than the time constant. The melt duration t_m, therefore, can be used to determine the critical frequency f_{cr} above which the spatial frequency content should be diminished.

$$f_{cr} = \sqrt{\frac{\rho}{8\pi^2 \mu t_m}} \qquad (2-6)$$

Experiments of laser polishing on nickel were used to show the effectiveness of the critical frequency concept. Microfabricated line features on nickel were polished with a 1064 nm Nd:YAG laser with 300 ns pulses. The critical frequency for the experimental condition was estimated. It was found that significant reduction in surface roughness could be achieved if the dominant frequency content of the original surface features was above the critical spatial frequency.

Vadali et al. [Vadali 2012] further developed the concept of critical frequency into a surface prediction methodology. In spatial frequency domain, the damping of a spatial frequency component is given by:

$$\zeta_\infty(f_x, f_y) = \zeta_0(f_x, f_y)\exp[-(f_x/f_{cr})^2 - (f_y/f_{cr})^2] \qquad (2-7)$$

where $\zeta_\infty(f_x, f_y)$ and $\zeta_0(f_x, f_y)$ are the final and initial amplitudes of a spatial frequency component, f_{cr} is the critical frequency, the cutoff point in the spatial frequency spectrum, above which a significant reduction in the amplitude is expected. Known the initial surface topography, material properties, and process parameters, the surface topography resulted from laser polishing can be predicted using Fourier and inverse Fourier analysis. Experiments of laser polishing on pure nickel, Ti6Al4V, and Al-6061 were conducted to validate the surface prediction model. The predicted surface topographies matched well with the experimental results for, resulting in predicted areal surface roughness within 12% of the experimental value for all three materials.

2.5.3 Fundamental Limit of Laser Polishing

Laser polishing will be used in this study as an example to demonstrate the feasibility to control fluid dynamics of laser-induced melt pool using nanoparticles and the possibility to overcome the fundamental limit of laser materials processing. A large number of existing studies

on laser polishing aimed to determine the parameters that result in the best surface finish. The studies suggest there exists a fundamental limit on the reduction of roughness achievable by laser polishing.

The resultant surface topography by laser polishing is dictated by the dynamics of melt pool flow. The melt pool flow is dominated by damped capillary oscillations at low laser fluences where is defined as *Capillary Regime* [Ma 2013, Pfefferkorn 2013, Ma 2014]. In the capillary regime, the smoothening mechanism is through a viscous dissipation based damping of capillary waves. The surface roughness decreases with increasing fluence because the surface capillary waves will be damped more due to the increased melting time. However, as the fluence increases to a certain level, thermocapillary flow begins to dominate the melt pool flow, where is defined as *Thermocapillary Regime* [Ma 2013, Pfefferkorn 2013, Ma 2014]. In the thermocapillary regime, the molten metal flows along the radial direction of the melt pool due to a surface tension gradient induced by a large temperature gradient. The surface asperities can be smoothed by the radial thermocapillary flow. However, the thermocapillary flow also introduces ripples and thereby increases surface roughness. To determine the optimal laser parameters, both the damping of capillary waves and the smoothening and roughening effects of the thermocapillary flow should be considered to achieve the maximum reduction of surface roughness for a given material. It is well known that the surface quality achievable by laser polishing is limited only through optimization laser parameters.

Since the melt pool dynamics is also governed by the thermophysical properties of the material, nanoparticles could be added into the base material to modify the thermophysical

properties, which provides a new pathway to break existing fundamental limit for a further improved surface finish.

2.5.4 Summary

As one of the important applications of laser melting, laser polishing has been extensively studied as a non-contact surface smoothening technology. Most existing studies on laser polishing aimed to determine the parameters that would result in the best surface finish. Although significant improvements in surface quality have been achieved, the studies suggest a fundamental limit exists in laser polishing if the thermophysical properties of the material to be polished are not modified. It is proposed that nanoparticles can be added to tune the melt pool dynamics during laser melting and thus improve the surface finish of laser polishing.

2.6 EFFECT OF NANOPARTICLES ON THERMOPHYSICAL PROPERTIES

2.6.1 Surface Tension

The effect of nanoparticles on gas-liquid surface tension is complex and rarely explored. Vafaei et al. measured the effective surface tension of aqueous nanofluids with Bi_2Te_3 nanoparticles and studied its dependence on nanoparticle size and concentration [Vafaei 2009]. The presence of nanoparticles in nanofluids reduced the effective surface tension and the largest reduction is greater than 50% when compared with the base fluid (pure water). This work showed the possibility of controlling the effective surface tension by adjusting nanoparticle characteristics (i.e., size and concentration). How the nanoparticles can be used to tune the surface tension of high temperature melt pools would be of tremendous scientific and engineering value.

2.6.2 Viscosity

The viscosity of molten metal matrix nanocomposites (MMNCs) has been rarely measured accurately, although it has been observed in experiments that an MMNC is more viscous than its base alloy. However, extensive experimental work has shown that nanofluids have higher viscosity than their base fluids. An empirical correlation was proposed based on a large amount of experimental data in literature [Corcione 2011]. It covers various nanoparticles (alumina, titania, silica, and copper) and base fluids (water, ethylene glycol, propylene glycol, and ethanol). The nanoparticle diameter ranges from 25 nm to 200 nm. The fraction of nanoparticles ranges from 0.01 vol. % to 7.1 vol. %. The best-fit correlation is

$$\frac{\mu_{eff}}{\mu_f} = \frac{1}{1 - 34.87(d_p/d_f)^{-0.3}\varphi^{1.03}} \qquad (2-8)$$

where μ_{eff} is the effective dynamic viscosity of a nanofluid, μ_f is the dynamic viscosity of the base fluid, d_p is the nanoparticle diameter, and d_f is the equivalent diameter of the base fluid molecule given by

$$d_f = 0.1\left(\frac{6M}{N\pi\rho_f}\right)^{1/3} \qquad (2-9)$$

where M is the molecular weight of the base fluid, N is the Avogadro number, and ρ_f is the mass density of the base fluid. As suggested by the correlation, the effective viscosity of the nanofluid increases as the nanoparticle diameter decreases and the volume fraction increases for a given base fluid. Also, the correlation does not depend on the material itself, but only dimensions. The laws of nanoparticle-modified viscosity in metal melts remain to be understood.

2.6.3 Heat Capacity

The heat capacity of a material is directly related to the phase or structure of the material. Since presence of nanoparticles can modify the microstructures of a material, addition of nanoparticles can potentially change the heat capacity of the material. It was found that heat capacity could be significantly increased by nanoparticles in different systems including molten slats and polymers [Nelson 2009, Tiznobaik 2009]. Electron microscopy analysis showed that nanoparticles could modify the microstructures of the molten salts, which contributed to the enhancement of the heat capacity [Tiznobaik 2009]. The influences of particular nanoparticles on the heat capacity of specific metals remain to be studied.

2.6.4 Thermal Conductivity

Heat is conducted by electrons and phonons in materials. Recent studies show that the presence of nanoparticles results in scattering of electrons and phonons. This scattering of electrons and phonon results in reduction of the thermal conductivity [Poudel 2008, Biswas 2012]. On the other hand, it was also shown that the nanoparticles can increase the thermal conductivity of the matrix if the nanoparticles themselves have higher carrier (electrons and holes) concentration than the base matrix. This higher carrier concentration enhances the electronic thermal conductivity and aids in improving the effective thermal conductivity of the matrix [Zebarjadi 2011]. Further improvement is possible by increasing the concentration of the nanoparticles. Therefore, the change of thermal conductivity in nanocomposites is a function of not just the concentration of the nanoparticles, but also the type of the nanoparticles.

2.6.5 Summary

It is believed, through literature review, that thermophysical properties can be altered by addition of nanoparticles and thus can be used to control the laser melting process. However, it is necessary to explore and quantify the influences of particular nanoparticles on thermophysical properties of metals and then to understand the consequent effects on laser melting.

CHAPTER 3. ELECTROCODEPOSITION OF METAL MATRIX NANOCOMPOSITES

Electrocodeposition is used in this study to prepare metal matrix nanocomposites (MMNCs) samples for laser melting. Electrocodeposition is chosen because of its low cost, simple setup and high quality. Electrocodeposition is actually one of the most promising technologies for fabrication of MMNCs to realize industrial applications because electrocodeposition coatings offer excellent performance and can directly grow on parts with complex geometries. Experimentations with various kinds of nanoparticles and electrocodeposition parameters were conducted to study their effects on dispersion and incorporation of nanoparticles. In-depth characterizations of the microstructures and mechanical performance of a nanocomposite deposit were then performed.

3.1 EXPERIMENTAL METHOD

3.1.1 Electrocodeposition

Among all the electrocodeposited nanocomposite coatings that have been investigated, nickel is the most popular base metal because of the low cost and high performance, and therefore it is selected in this study. Various nanoparticles were investigated, including alumina (Al_2O_3), silicon carbide (SiC), zirconia (ZrO_2), and yttria (Y_2O_3). The nanocomposites were prepared by electrocodeposition of nickel and nanoparticles with a standard nickel Watts bath containing nanoparticles. Nickel Watts bath was selected because it is one of the most popular electrolytes for electroplating in industries. The composition of the nickel Watts bath is listed in Table 3-1. Although the electrolyte could be repeatedly used, a fresh electrolyte was always prepared for each

experiment to eliminate the potential effect of minor change in the composition. The amount of electrolyte for each experiment was 200 mL.

Table 3-1 Composition of the nickel Watts bath

Chemical	Mass concentration (g/L)
Nickel Sulfate, $NiSO_4 \cdot 6H_2O$	250
Nickel Chloride, $NiCl_2 \cdot 6H_2O$	30
Boric Acid, H_3BO_3	30

The process flow of electrocodeposition is schematically shown in Figure 3-1. The solution containing nanoparticles was mechanically mixed and ultrasonically processed for 2 hours prior to electrocodeposition to achieve a uniform distribution and effective dispersion of the nanoparticles. Electrocodeposition was then carried out with the continuation of mechanical stirring and ultrasonication to maintain the nanoparticle dispersion and distribution. An ultrasonication amplitude of 23 μm was used for all the experiments except for studying the effect of the amplitude. The temperature was maintained at 43 °C. All electrocodeposition processes were carried out for 2 hours at a current density of 1 A/dm^2 unless specified differently. Al 6061 alloy substrates were used as the cathodes for deposition. A polyimide mask was used to expose only the area to be deposited on, which was a circle with a diameter of 22.2 mm. For comparison, pure Ni samples were also prepared under the same electrodeposition parameters without ultrasonication.

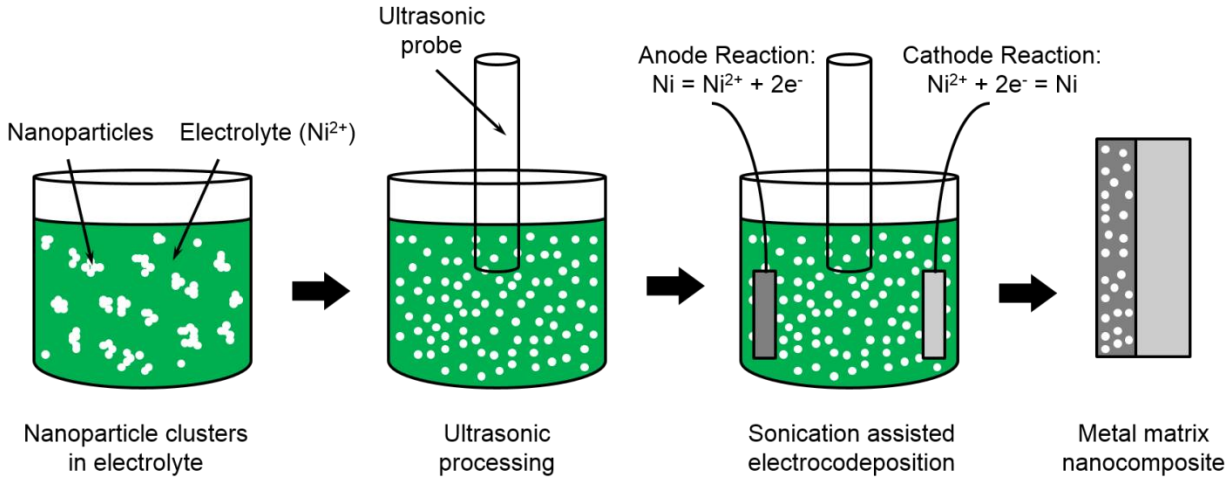

Figure 3-1 Schematic of the electrocodeposition process

3.1.2 Characterization

Characterization of micro/nano-structures of samples was carried out using scanning electron microscopy (SEM) facilitated with energy dispersive X-ray spectroscopy (EDS/EDX). EDS analysis was used to quantify the fraction of nanoparticles incorporated into the nanocomposites. The volume fraction of nanoparticles was estimated based the atom fraction of the major element in the nanoparticles and the base metal. Three EDS measurements at different locations were made for each sample, and the average value and the standard deviation of the volume fraction were calculated.

The mechanical performance of the deposits was characterized with Vickers hardness. The load was 50 g and the dwell time was 10 s. Five tests were conducted for at different locations for each sample and an average value of microhardness was used for describe the mechanical property of a deposit.

3.2 EXPERIMENTAL RESULTS

3.2.1 Effect of Nanoparticle Material

Firstly, pure nickel deposit was prepared without addition of any nanoparticles for reference. Figure 3-2 shows SEM micrographs of electrodeposited pure Ni surface at different magnifications. The pure nickel deposit is composed of pyramidal crystals by observation from the surface. The grain size is highly non-uniform: large grains are surrounded by fine grains.

Various nanoparticles were then added to the Watts electrolyte to investigate the effects of nanoparticle material on the incorporation and dispersion behaviors during electrocodeposition. The nanoparticles were selected based on the following requirements: (a) thermodynamically stable in the melts at processing temperatures (no or minimal chemical reaction), (b) good interfacial bonding between matrix alloys and nanoparticles, and (c) commercially available. The nanoparticles used in this study include alumina (Al_2O_3), silicon carbide (SiC), zirconia (ZrO_2), and yttria (Y_2O_3). The parameters regarding the nanoparticles are listed in Table 3-2. The mass concentration for each type of nanoparticle is different from each other because the nanoparticles have different densities and the volume fraction of nanoparticles in the electrolyte is kept the same for different kinds of nanoparticles. While characterizing the nanocomposite deposits, special attentions were paid to the dispersion of the incorporation amount of nanoparticles as these parameters determine the performance of the deposits including enhancement in mechanical properties, modification of thermophysical properties, and so on.

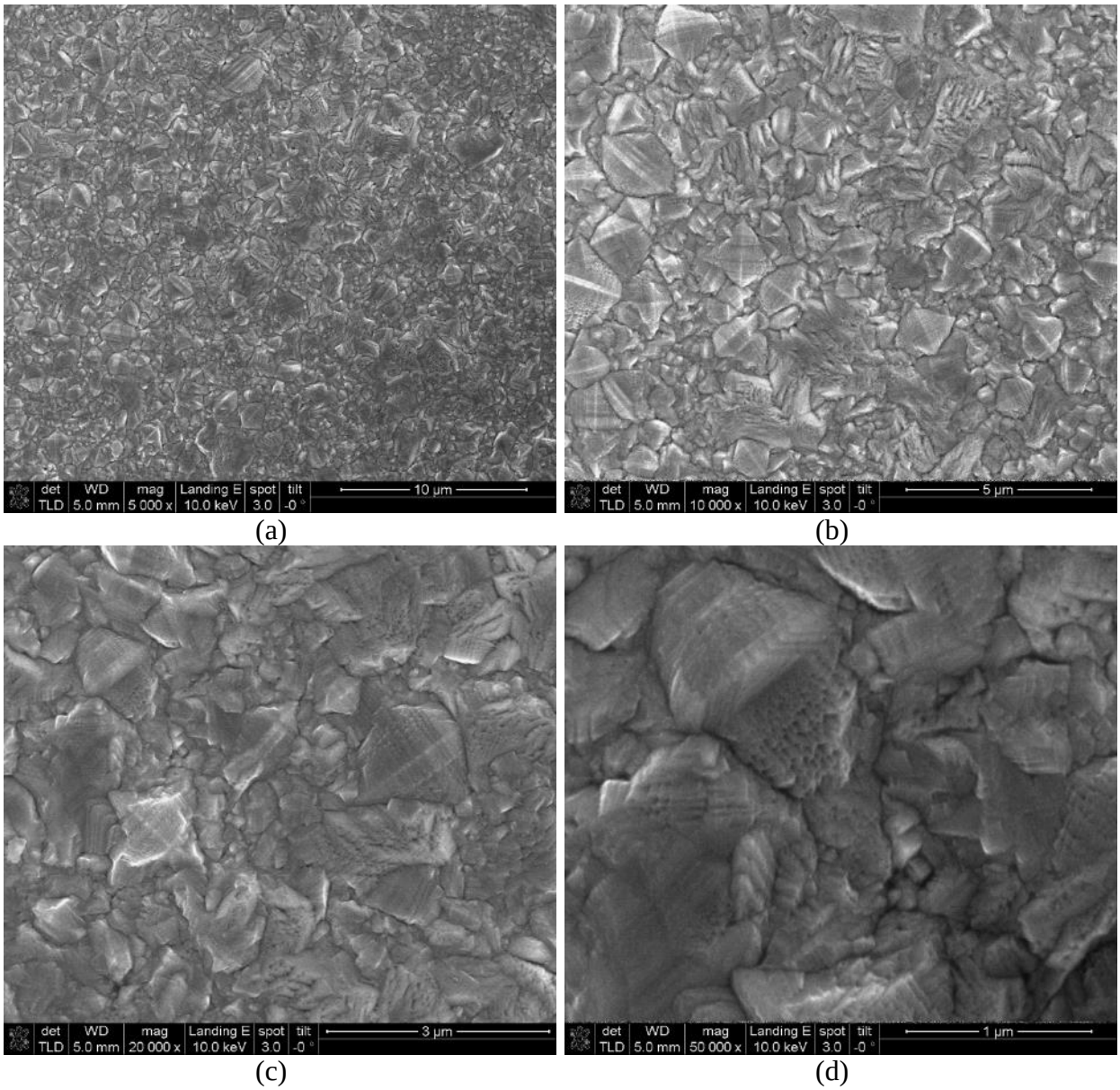

(a) (b)

(c) (d)

Figure 3-2 SEM micrographs of electrodeposited pure nickel surface

The SEM micrographs of electrocodeposited Ni/Al_2O_3 surface are shown in Figure 3-3. The tiny white spots in the micrographs are Al_2O_3 nanoparticles, which is confirmed by EDS analysis. The Al_2O_3 nanoparticles are evenly distributed in Ni matrix without large clusters, indicating a uniform distribution and effective dispersion of nanoparticles. An excellent dispersion and distribution of nanoparticles is necessary to achieve ideal laser melting results because

nanoparticle clusters are as not effective as dispersed nanoparticles in modification of thermophysical properties. With the atom fractions of Al and Ni in the nanocomposite measured by EDS, the volume fraction of Al_2O_3 nanoparticles was estimated to be 4.4 ± 0.1 vol. %.

Table 3-2 Parameters of nanoparticles

Material	Chemical formula	Nominal size (nm)	Density (g/cm3)	Mass concentration (g/L)
Alumina	Al_2O_3	50	3.95	10
Silicon carbide	SiC	45–55	3.21	8
Zirconia	ZrO_2	40	5.57	14
Yttria	Y_2O_3	30–45	5.01	12

In addition, the microstructure and morphology of the electrodeposited nickel were significantly altered by addition of Al_2O_3 nanoparticles. The grains were considerably refined and the distribution of the grain size is more uniform. Electrodeposition is a competition between nucleation and crystal growth. Incorporation of Al_2O_3 nanoparticles introduces barriers for grain growth and provides nucleation sites in the meantime. Therefore, significant grain refinement was achieved by addition of Al_2O_3 nanoparticles.

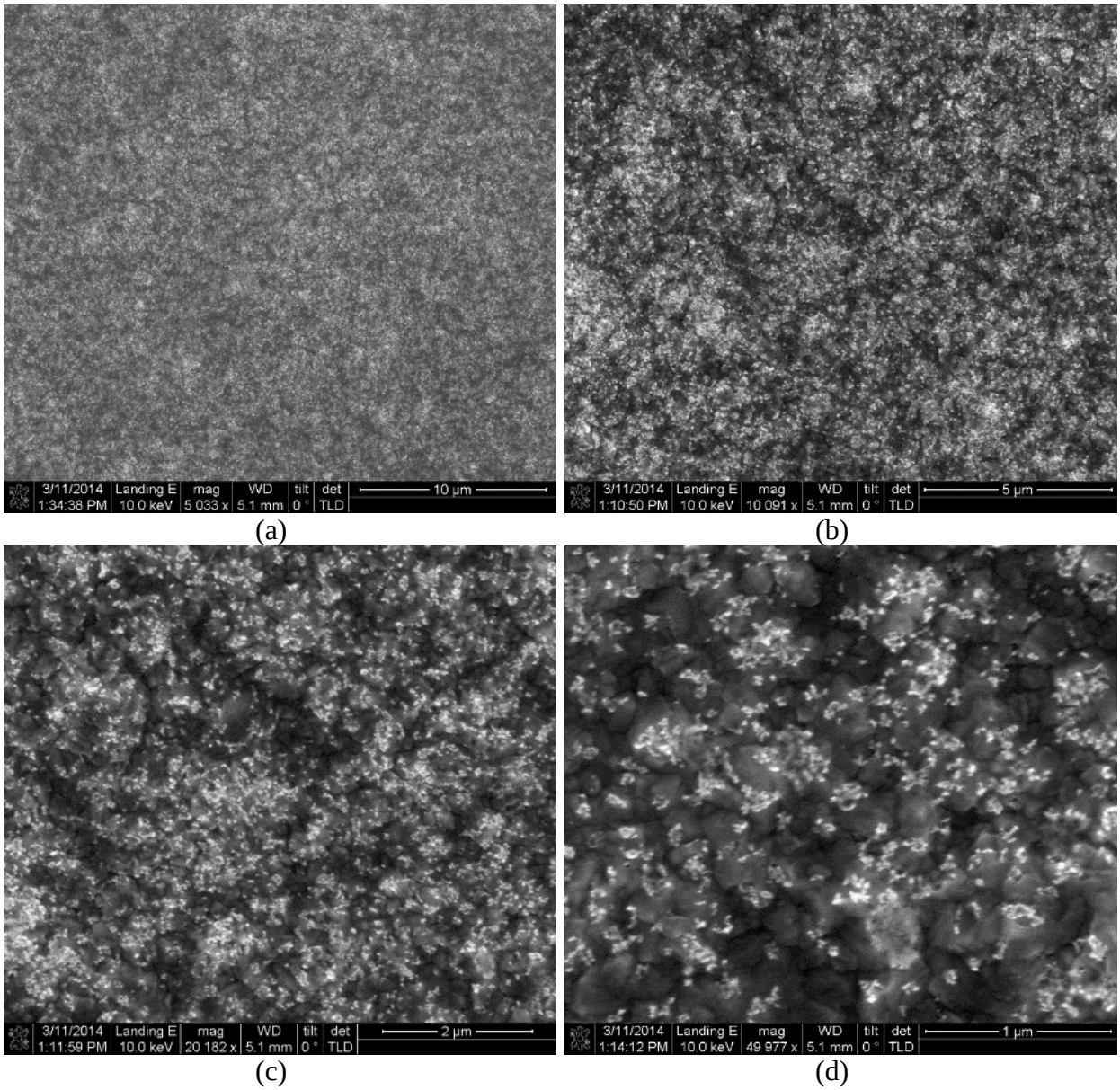

Figure 3-3 SEM micrographs of electrocodeposited Ni/Al_2O_3 surface

Figure 3-4 shows the SEM micrographs of electrocodeposited Ni/SiC surface. The SiC nanoparticles appear as the bright spots. As compared with Al_2O_3 nanoparticles, the SiC nanoparticles were much less incorporated. The volume fraction of SiC nanoparticles in the nanocomposite was estimated to be 2.6 ± 0.1 vol. % based on the EDS measurements of the atom fractions of Si and Ni.

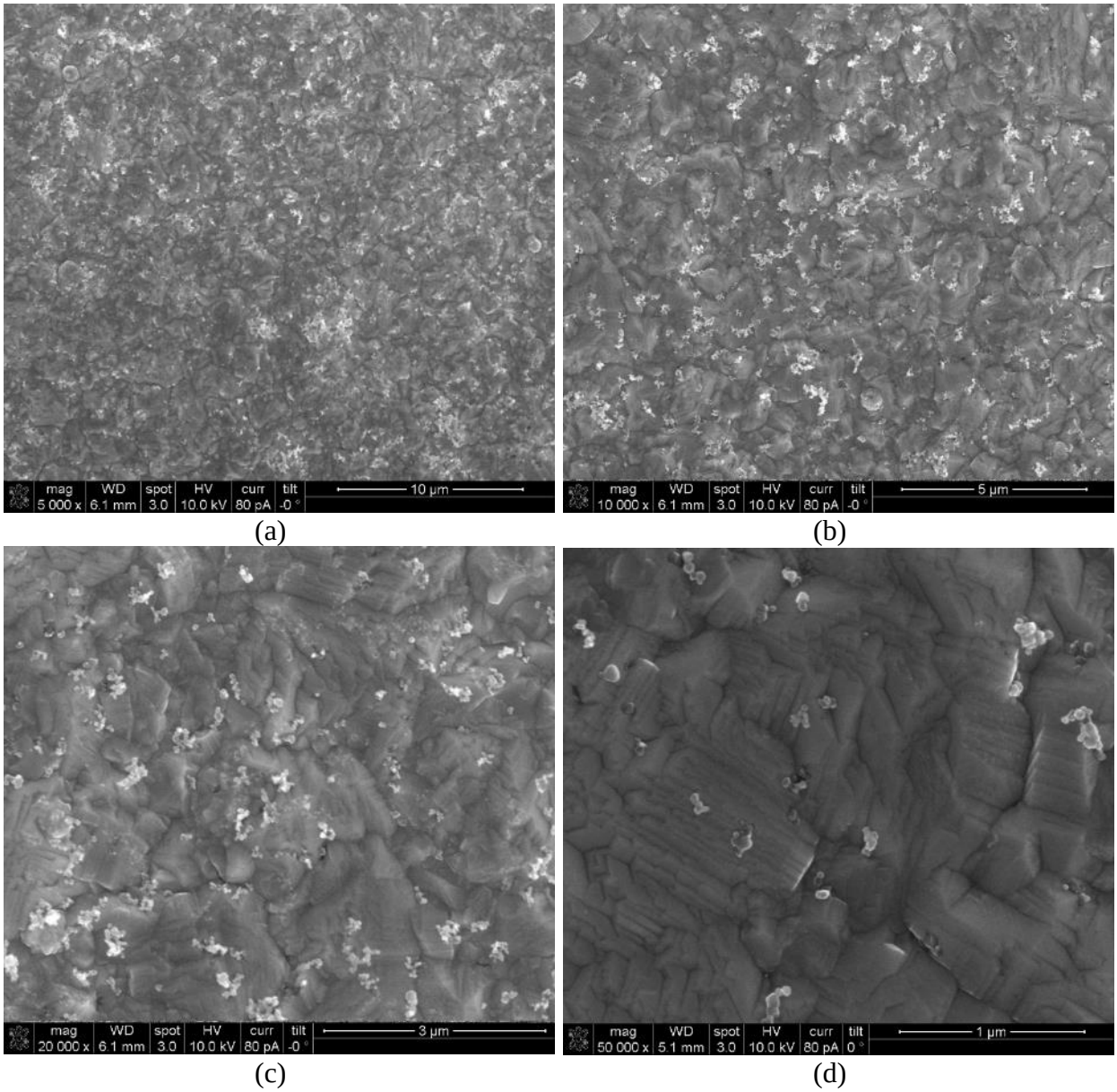

Figure 3-4 SEM micrographs of electrocodeposited Ni/SiC surface

The difference in the incorporation fraction between SiC than Al_2O_3 nanoparticles suggests that the nanoparticle material plays a vital role in the incorporation process. The nature of the nanoparticles determines the chemical interactions with the electrolyte and the nickel deposit and thus the attraction or repulsion force with the cathode. The force exerted on the nanoparticles towards the cathode is probably less attractive in the case of SiC than Al_2O_3. In addition,

agglomeration is slightly more significant for SiC than Al_2O_3 possibly because the van der Waals attraction between nanoparticles, i.e., the interparticle force, is stronger in SiC than Al_2O_3.

The Ni/ZrO_2 nanocomposite is shown in Figure 3-5. The spherical particles are the ZrO_2 phase, which are evenly distributed in the Ni matrix. The dispersion of the ZrO_2 is excellent: almost no clustering of nanoparticles is observed. The incorporation amount is 2.6 ± 0.8 vol. %.

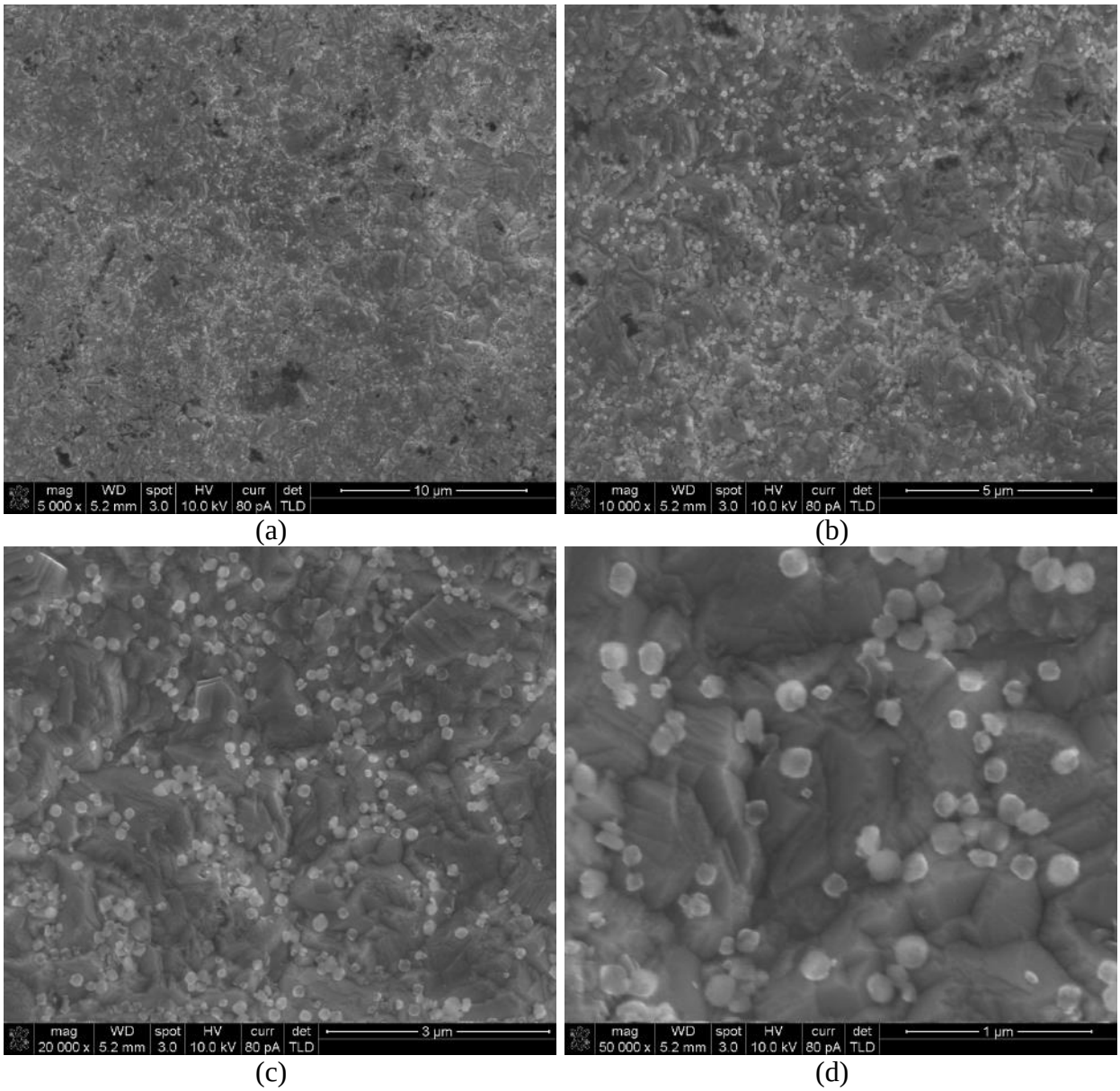

Figure 3-5 SEM micrographs of electrocodeposited Ni/ZrO_2 surface

However, the actual size of the nanoparticles appear larger than the nominal size (40 nm) possibly because a different characterization method is used by the vendor.

Figure 3-6 shows the SEM micrographs of electrocodeposited Ni/Y_2O_3 surface. The white spots in the images are the Y_2O_3 nanoparticles, which is identified "point" EDS analysis. The incorporation amount of Y_2O_3 nanoparticles is so low Y signal was not detectable by "area" EDS analysis and thus the volume fraction of Y_2O_3 nanoparticles could be estimated. Again, it is the material nature of the nanoparticles that determines the interactions with the electrolyte and the cathode. To improve the incorporation, surfactant can be added into the solution in future study.

Although only minimal amount of Y_2O_3 nanoparticles were incorporated into the nickel deposit, it significantly altered the crystal structure of nickel by addition of nanoparticles. The grain size was considerably refined and uniformly distributed. The shape of the grains changed as well: more elongated as compared with the pure nickel in Figure 3-2.

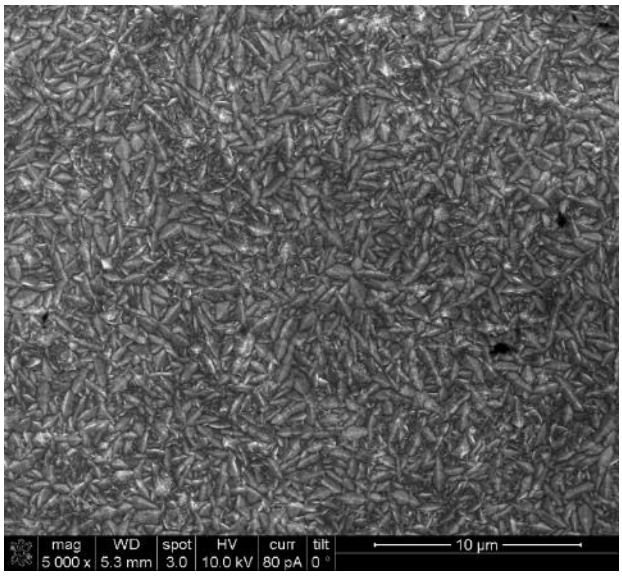

(a)

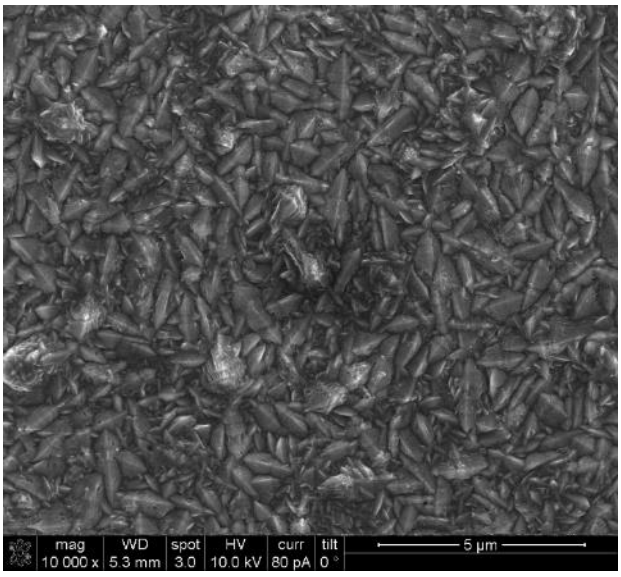

(b)

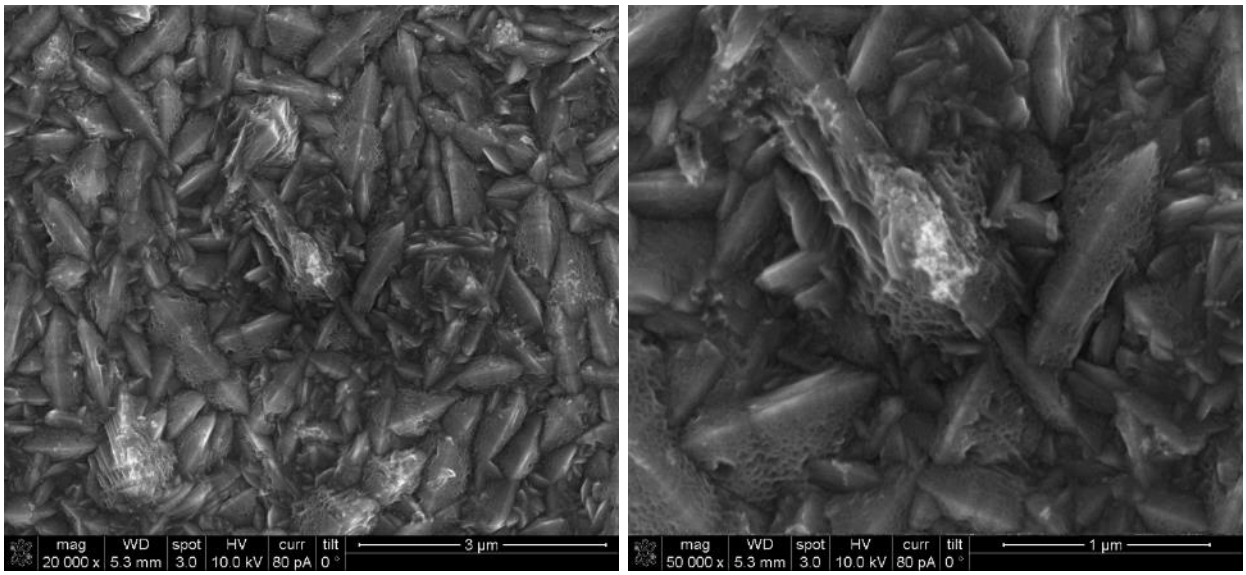

(c) (d)

Figure 3-6 SEM micrographs of electrocodeposited Ni/Y_2O_3 surface

3.2.2 Effect of Electrocodeposition Parameters

Among the nanoparticles that have been attempted, Al_2O_3 nanoparticles offer the best performance in terms of dispersion and incorporation. A further study on the effect of electrocodeposition parameters was conducted for Ni/Al_2O_3 nanocomposite.

3.2.2.1 Nanoparticle Concentration

The nanoparticle concentration in the electrolyte plays an important role in dispersion and incorporation. The concentration of Al_2O_3 nanoparticles was increased from 10 g/L to 20 g/L to investigate the electrocodeposition behaviors of the nanoparticles. Figure 3-7 shows SEM micrographs of electrocodeposited Ni/Al_2O_3 at increased concentration of Al_2O_3 nanoparticles in electrolyte (20 g/L). More Al_2O_3 nanoparticles were incorporated at increased concentration, when compared with the Ni/Al_2O_3 electrocodeposited at original concentration (10 g/L) in Figure 3-3. In addition, more clusters of Al_2O_3 nanoparticles can be observed at the increased concentration.

The nanoparticles agglomerate more significantly because collision rate between the nanoparticles is increased.

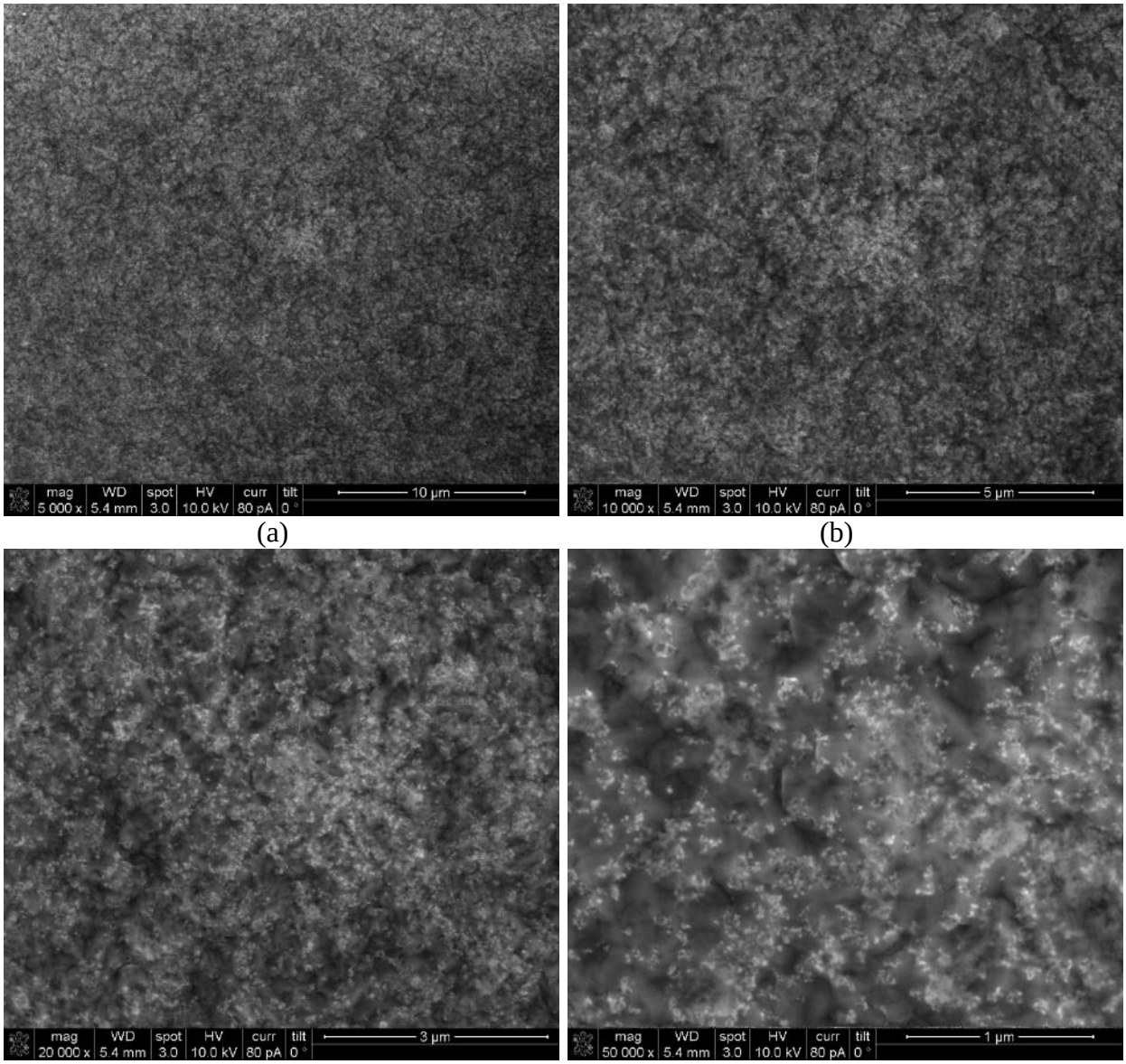

(a) (b)

(c) (d)

Figure 3-7 SEM micrographs of electrocodeposited Ni/Al_2O_3 at increased concentration of Al_2O_3 nanoparticles in electrolyte (20 g/L)

3.2.2.2 Ultrasonication Amplitude

The acoustic intensity of ultrasonication is proportional to the square of oscillation amplitude given the material and the frequency. Therefore, the amplitude is key parameter to determine the strength of ultrasonication. In order to study the effect of the ultrasonication amplitude on the electrocodeposition process, the amplitude was increased from 23 μm to 32 μm with the nanoparticle concentration (10 g/L Al_2O_3). Figure 3-8 shows some of SEM micrographs of electrocodeposited Ni/Al_2O_3 at increased ultrasonication amplitude (32 μm). As compared with Ni/Al_2O_3 obtained at low amplitude in Figure 3-3, the dispersion of the Al_2O_3 nanoparticles was almost the same and the incorporation amount is decreased.

However, the distribution of the nanoparticles is not uniform at increased ultrasonication amplitude. Figure 3-8 shows one part of the sample, which represents a decent placement of nanoparticles. Figure 3-9 shows another part of the same sample, in which no nanoparticle could be observed.

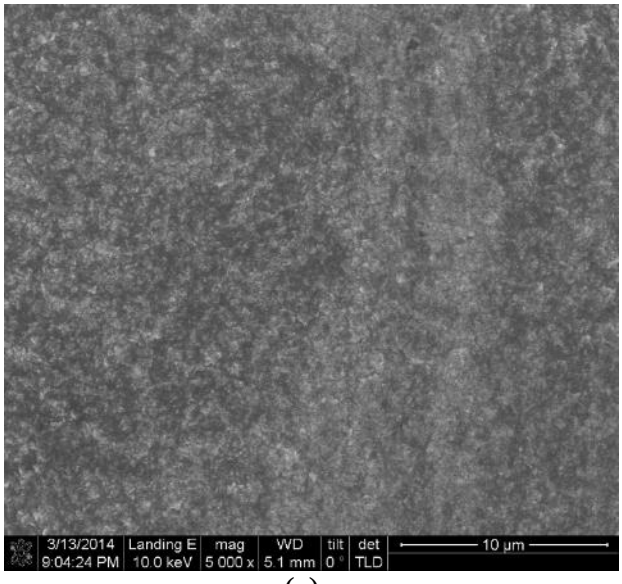

(a)

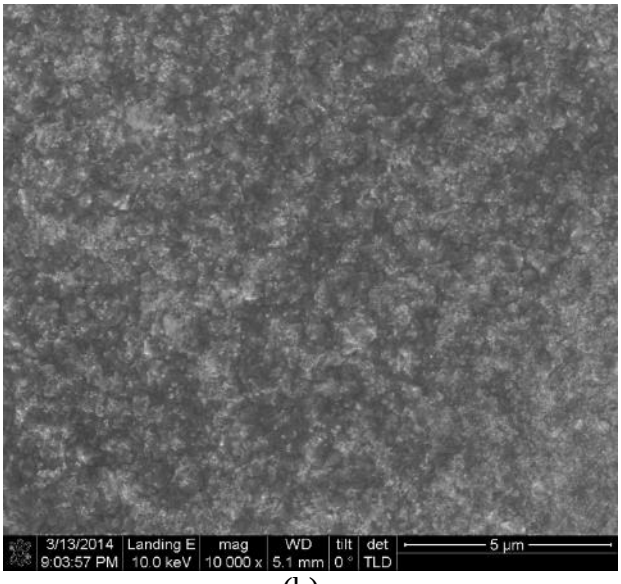

(b)

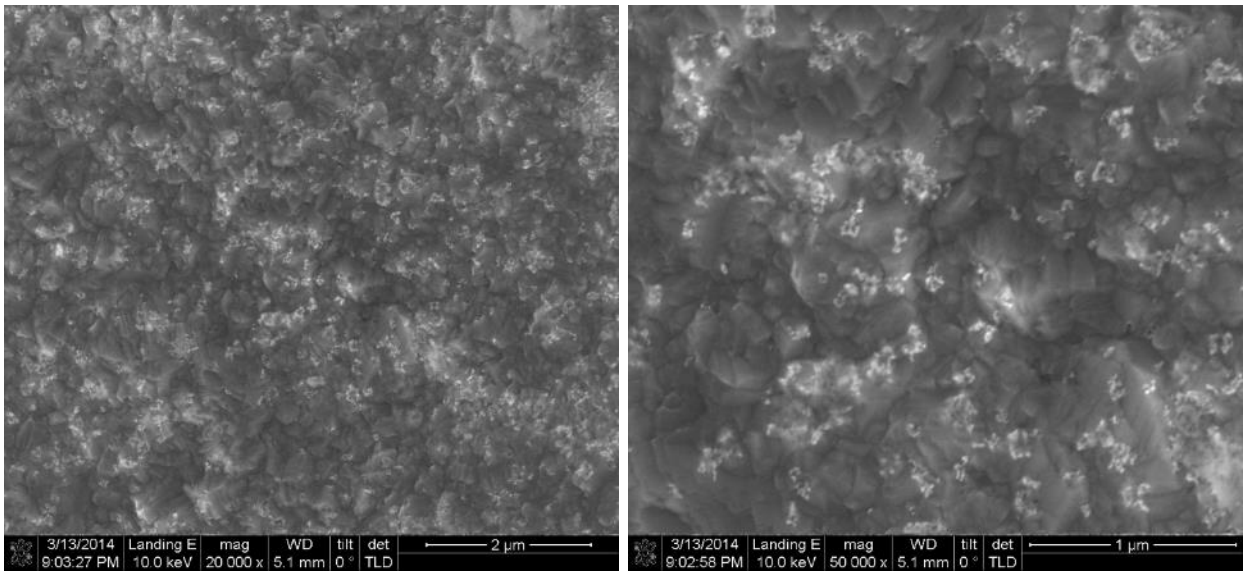

(c) (d)

Figure 3-8 SEM micrographs of electrocodeposited Ni/Al_2O_3 at increased ultrasonication amplitude (32 µm)

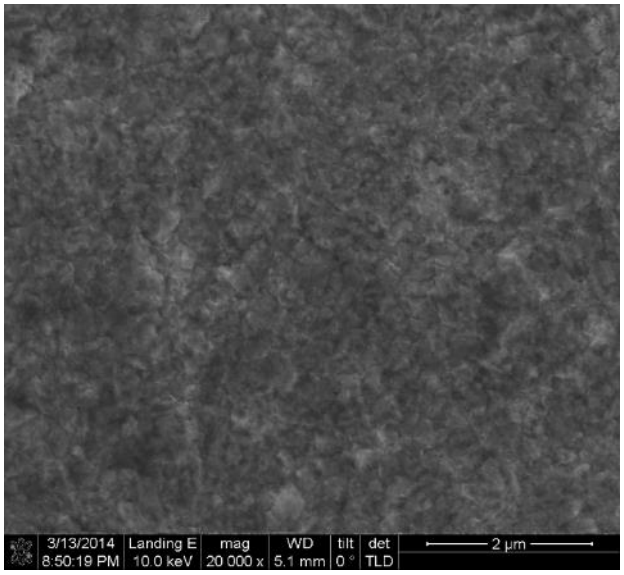

Figure 3-9 Issue of electrocodeposition of Ni/Al_2O_3 at increased ultrasonication amplitude: non-uniform distribution of nanoparticles

In summary, the Ni/Al_2O_3 nanocomposite in Figure 3-3 that is obtained at the concentration of 10 g/L and the ultrasonication amplitude of 23 µm provides the best results in terms of

dispersion and incorporation fraction of nanoparticles. More in-depth studies were carried out on this particular sample.

3.2.3 Characterization of the Ni/Al_2O_3 Nanocomposite

Further characterizations were conducted on the Ni/Al_2O_3 deposit. The characterizations include microstructural study on the cross section and Vickers hardness tests.

3.2.3.1 Cross Section

Figure 3-10 shows the SEM images of the fractured cross section of electrocodeposited Ni/Al_2O_3. By characterization of the cross section of the Ni/Al_2O_3 coating, it shows Al_2O_3 nanoparticles were evenly present all over the entire sample, which suggests a uniform incorporation process.

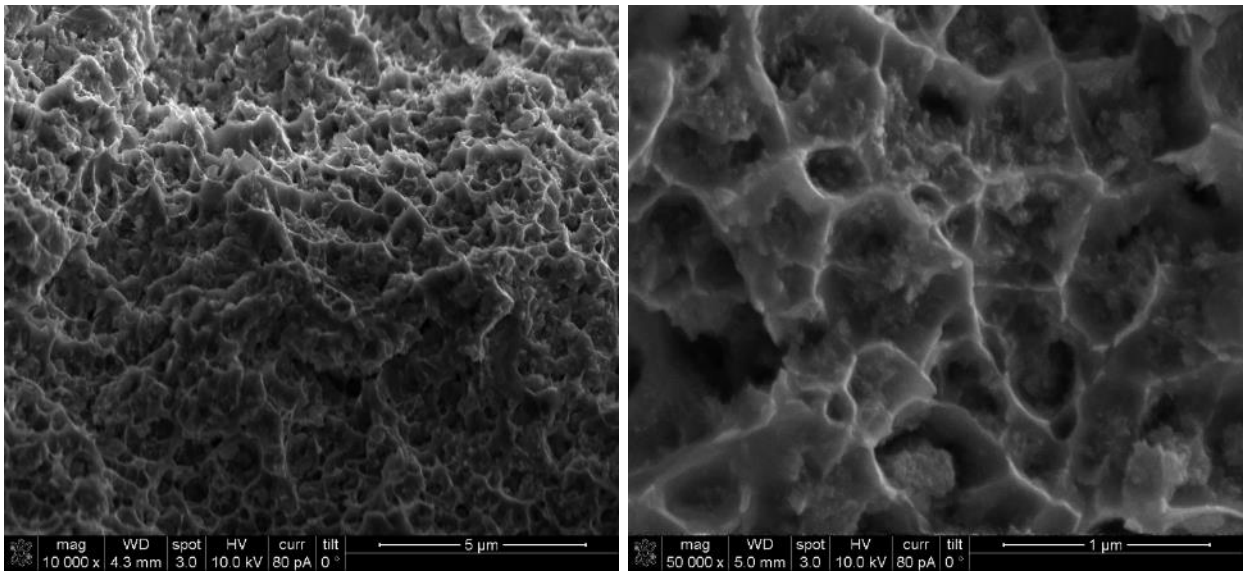

(a) (b)

Figure 3-10 Fracture surface (cross section) of electrocodeposited Ni/Al_2O_3

3.2.3.2 Microhardness

In order to prepare samples with reasonable thickness for Vickers hardness tests, both the electrodeposition current and time were doubled: the current density was increased to 2 A/dm^2 and the time was increased to 4 h. Al 6061 alloy substrates were used as the cathodes for deposition. The box plots based on five hardness measurements are shown in Figure 3-12. The average Vickers hardness (HV0.05) of pure nickel was 153.9 kg/mm^2 and that of Ni/Al_2O_3 nanocomposite was 267.1 kg/mm^2, which is corresponding to 73.6 % enhancement.

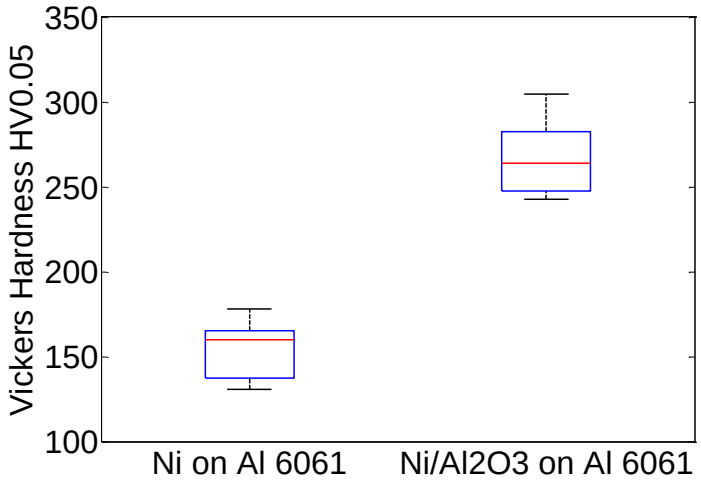

Figure 3-11 Comparison of microhardness between Ni and Ni/Al_2O_3 coatings on Al 6061 alloy

3.3 SUMMARY

Metal matrix nanocomposites were prepared by electrocodeposition with the assistance of ultrasonic cavitation. Various types of nanoparticles were experimented under same conditions, including Al_2O_3, SiC, ZrO_2, and Y_2O_3. All the nanoparticles were fairly well dispersed. The incorporation amount of the nanoparticles is the highest for Al_2O_3, medium for SiC and ZrO_2, but

only minimal for Y_2O_3. The effects of electrocodeposition parameters were further studied on Ni/Al_2O_3 system. The best results in terms of dispersion and incorporation fraction were obtained at an Al_2O_3 concentration of 10 g/L and an ultrasonication amplitude of 23 μm. Finally, in-depth characterizations of the Ni/Al_2O_3 sample were carried out. The SEM observation of the cross section of the sample showed that the distribution of nanoparticles was highly uniform across the entire sample. The microhardness tests showed the addition of Al_2O_3 nanoparticles significantly enhanced the mechanical properties of the base nickel.

CHAPTER 4. MEASUREMENTS OF OPTICAL AND THERMOPHYSICAL PROPERTIES OF MMNCS

To fundamentally study laser melting of metal matrix nanocomposites (MMNCs), especially the nanoparticles-induced difference during the process, it is crucial to gain knowledge on the optical and thermophysical properties of MMNCs, which will determine the heat transfer and fluid flow process and thus the microstructures and the performance. However, these properties are mostly not available. Therefore, experimental measurements of the essential optical and thermophysical properties were performed on the MMNCs of interests, i.e., Ni/Al_2O_3 and Ni/SiC. The measured properties will be used to understand the laser melting of MMNCs using analytical and numerical heat transfer and fluid flow models, which can provide valuable insights to reveal the effects of nanoparticles on laser melting.

4.1 REFLECTIVITY

When a laser irradiates on the surface of a bulk metallic material, a fraction of the energy is reflected and the rest part is absorbed by a thin surface layer. The absorbed part is the energy input into the material by the incident light. The energy input and laser beam diameters will determine the laser fluence, which is crucial for laser-assisted manufacturing processes.

To describe the absorption and reflection behaviors, the absorptivity (A) and reflectivity (R) of a material at a certain wavelength are respectively defined as the ratios of the absorbed and reflected energies to the incident energy. Since an infrared light cannot transmit through bulk

metals and alloys, the incident energy is either reflected or absorbed. Therefore, the sum of the absorptivity and reflectivity is simply one, i.e., $A + R = 1$.

The absorptivity or reflectivity is usually available for popular engineering materials. However, for metal matrix nanocomposites as an emerging class of materials, the effects of nanoparticles on the absorption and reflection behaviors have not been studied. Presence of nanoparticles in metals, especially on or near surface, will affect the laser absorption since the nanoparticles would introduce a large number of scattering sites for electromagnetic waves and the nanoparticles can have different optical properties from the matrix. It is of both scientific and technical interests to study the effects of nanoparticles on the optical properties of nanocomposites. The effective reflectivity of metal matrix nanocomposite was experimentally measured and compared with that of the corresponding pure metal.

4.1.1 Sample Preparation

In order to eliminate the effect of surface roughness on the reflectivity measurement, optically smooth samples were prepared by electroplating on silicon wafers. Pure Ni and Ni/Al_2O_3 nanocomposite samples were fabricated using a process flow as shown in Figure 4-1. Firstly, a chromium adhesion layer (30 nm) and a gold seed layer (50 nm) were deposited on silicon wafer by electron beam evaporation. Pure Ni or Ni/Al_2O_3 nanocomposite was then electrodeposited with the method described earlier in Chapter 3. The concentration of Al_2O_3 nanoparticles used for preparation of Ni/Al_2O_3 nanocomposite was 10 g/L. Finally, the silicon wafer was etched out using potassium hydroxide solution (30 wt. %) at 85 °C, after which the chromium layer was etched out by a commercial chromium etchant (Cr-7S) and the gold layer by a gold etchant (TFA). The

surface roughnesses of the Ni and Ni/Al_2O_3 were measured with white light interferometry. Five measurements were carried for each sample. The resultant surface roughnesses of both Ni and Ni/Al_2O_3 were less than 20 nm, which were much smaller than the laser wavelength of interest (1070 nm). Therefore, the effect of surface roughness on the reflectivity is negligible.

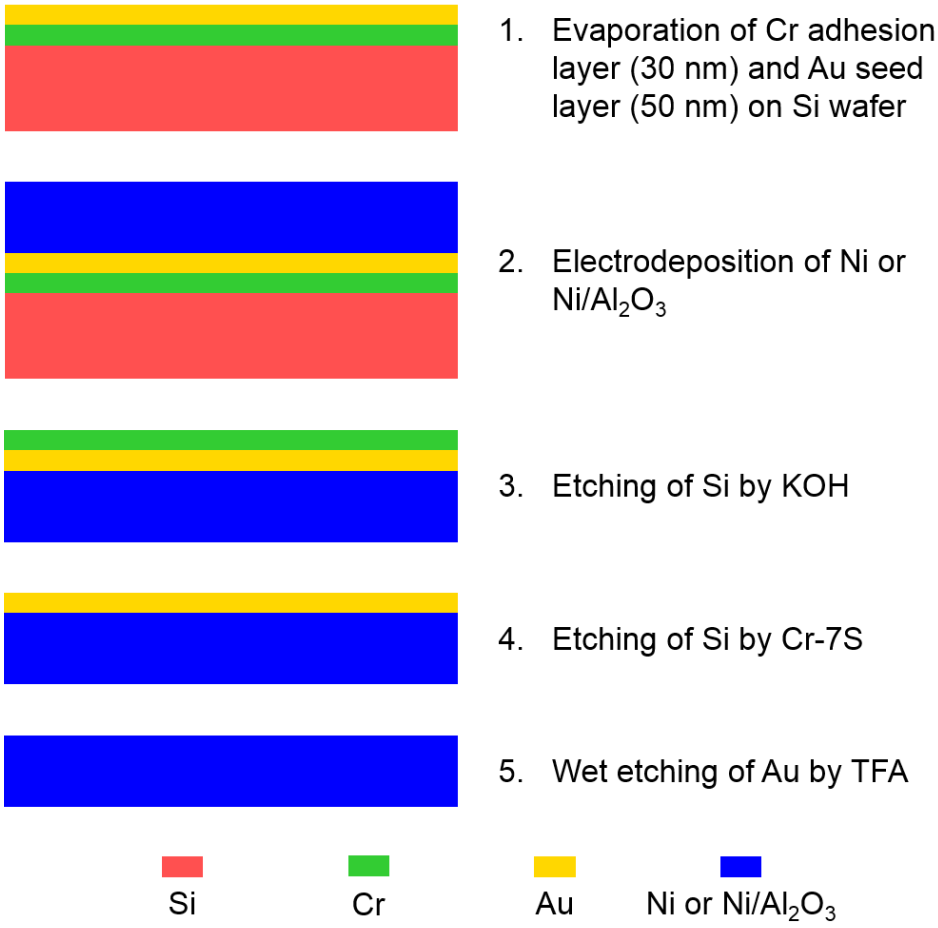

Figure 4-1 Process flow for preparation of pure Ni and Ni/Al_2O_3 nanocomposite samples

The microstructure of the Ni/Al_2O_3 nanocomposite was characterized with scanning electron microscopy (SEM). The SEM micrographs of the nanocomposite surface are shown in Figure 4-2. The microstructure of the Ni/Al_2O_3 nanocomposite herein obtained using the silicon wafer is very similar to that prepared on the aluminum alloy substrate in Chapter 3. The bright

phases are the Al_2O_3 particles, which are uniformly distributed in the dark Ni matrix. In addition, the nanoparticles are well dispersed. The volume fraction of Al_2O_3 nanoparticles was estimated to be 1.8 ± 0.3 vol. %. The consistent, excellent quality of the nanocomposite and its surface is important to ensure a reliable measurement of laser reflectivity on MMNCs.

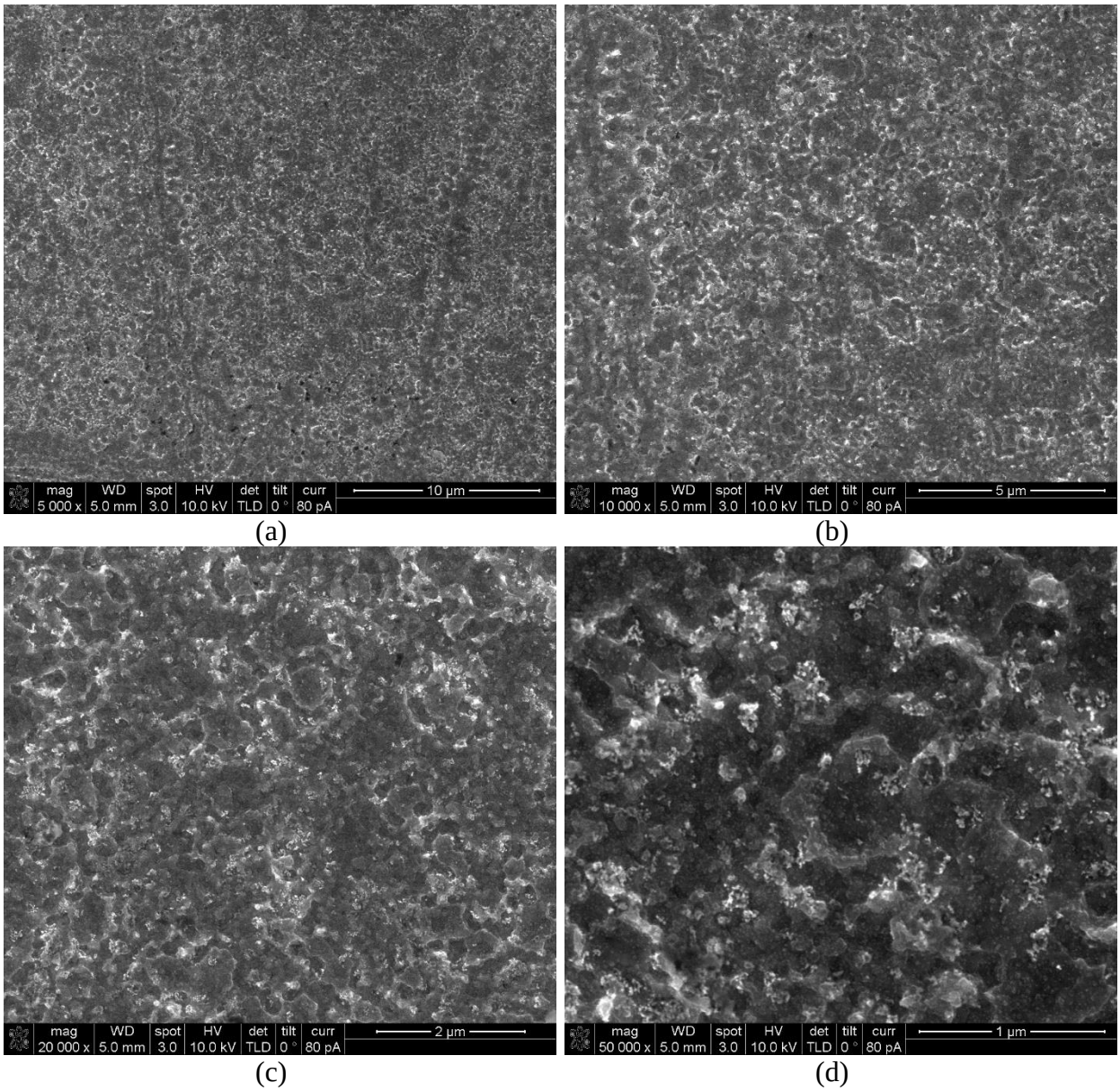

(a) (b)

(c) (d)

Figure 4-2 SEM micrographs of electrocodeposited Ni/Al_2O_3 surface after silicon wafer etching

4.1.2 Experimental Setup

Reflectivities of pure Ni and Ni/Al_2O_3 nanocomposite were experimentally determined using a power sensor to measure the incident and reflected powers. The laser incident angle is set at 45°. The experimental setup is schematically shown in Figure 4-3. According to Fresnel's equations, the dependence of reflectivity of circularly or randomly polarized light on the incident angle is negligible from 0° to 45°. Figure 4-4 shows the calculated dependence of the reflectivity of pure Ni on the incident angle at the wavelength of 1070 nm using Fresnel's equations. The reflectivity of circularly or randomly polarized light is the mean between the values of transverse-magnetic and transverse-electric waves. Because the laser to be used in this study is randomly polarized, the measurement results are applicable for a large range of incidence directions, including normal incidence.

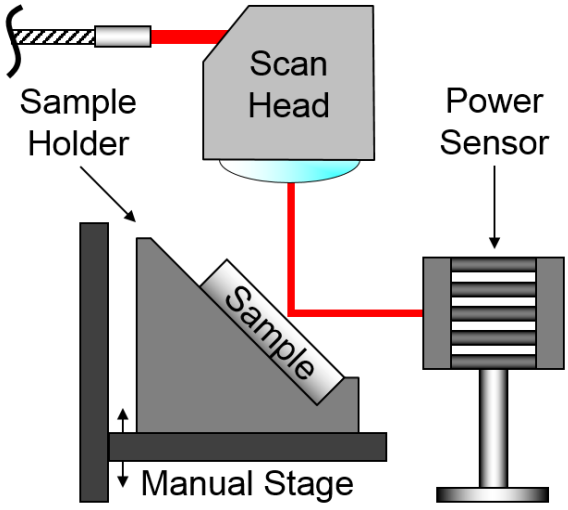

Figure 4-3 Experimental setup for reflectivity measurement

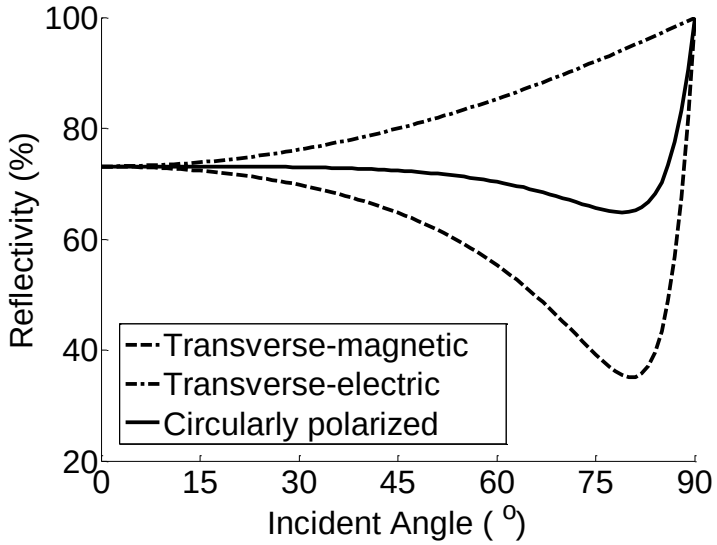

Figure 4-4 Dependence of the reflectivity of pure Ni on incident angle

4.1.3 Experimental Results

Before measuring the reflectivities of the materials of interest, the measurements were carried out on a silicon wafer to validate the experimental method because the optical properties of silicon wafer are well established for comparison. The measurements were conducted at five different incident power levels and each was repeated three times. The power measurement results are shown in Tables 4-1 and 4-2. Although there is mismatch between the commanded power and the actual incident power due to the calibration error of the laser, especially at low power levels, the standard deviation is very small for both the incident and reflected power at each commanded power, indicating an excellent repeatability in the power measurement. The average reflected power is highly proportional to the average incident power, as shown in Figure 4-5. The reflectivity of the silicon wafer can be determined by linear regression. The reflectivity is about 31.7 % with a coefficient of determination (R^2) of 0.9993, which agrees well the reported value (31.1%) [Li 1993].

Table 4-1 Measurements of the incident power on the silicon wafer

Commanded Power (W)	Measured Incident Power (W)			Average (W)	Standard Deviation (W)
	Test No. 1	Test No. 2	Test No. 3		
2	2.85	2.86	2.86	2.86	0.01
4	4.90	4.90	4.90	4.90	0.00
6	6.92	6.92	6.92	6.92	0.00
8	8.96	8.96	8.96	8.96	0.00
10	10.98	10.97	11.01	10.99	0.02

Table 4-2 Measurements of the reflected power from the silicon wafer

Commanded Power (W)	Measured Reflected Power (W)			Average (W)	Standard Deviation (W)
	Test No. 1	Test No. 2	Test No. 3		
2	0.93	0.92	0.9	0.92	0.02
4	1.55	1.57	1.6	1.57	0.03
6	2.16	2.17	2.18	2.17	0.01
8	2.83	2.81	2.79	2.81	0.02
10	3.49	3.54	3.5	3.51	0.03

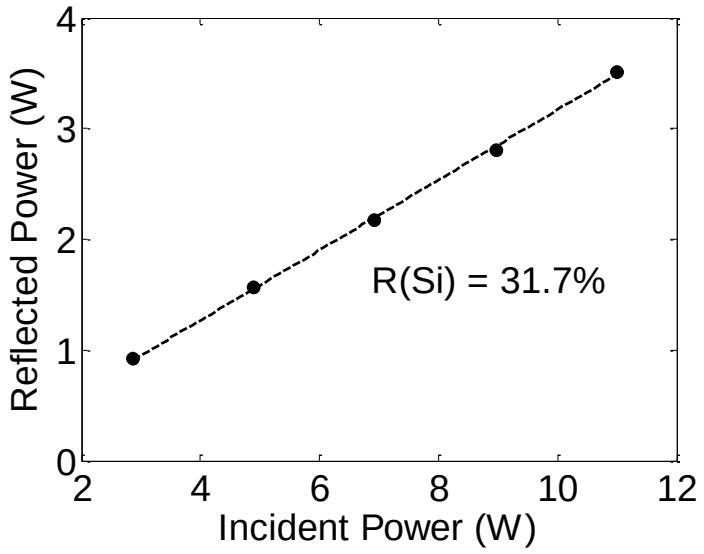

Figure 4-5 Measurement of reflectivity of silicon wafer

After the validation of this experimental method, the measurements were then conducted on pure Ni and Ni/Al_2O_3 nanocomposite samples prepared by the electroplating process. Similar to the case of silicon wafer, the reflected power is proportional to the incident powder for both Ni and Ni/Al_2O_3 as shown in Figure 4-6. By linear regression, the reflectivities of Ni and Ni/Al_2O_3 are determined to be 67.4 % and 65.8 %, respectively. The reflectivity of Ni/Al_2O_3 nanocomposite is only slightly different than that of pure Ni probably because the portion of Al_2O_3 nanoparticles is small and Al_2O_3 is transparent at this wavelength (1070 nm). More rigorous study (both theoretical and experimental) would be of interests to understand the exact effect of different nanoparticles on light reflection and absorption behavior of nanocomposites.

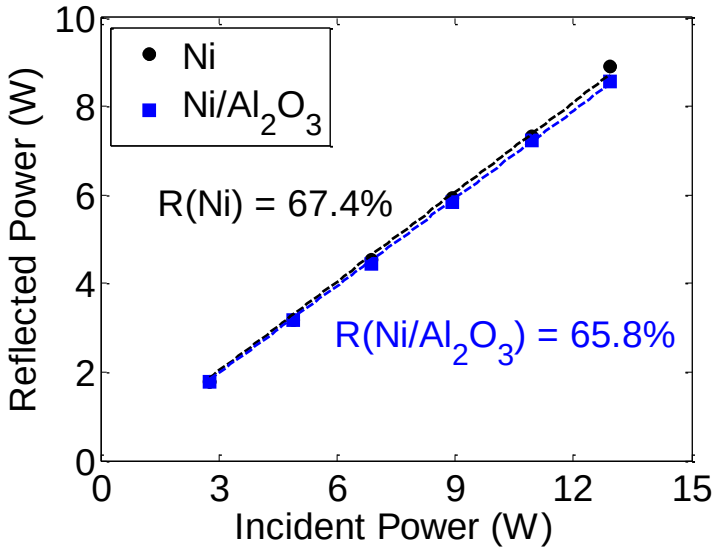

Figure 4-6 Measurement of reflectivities of pure Ni and Ni/Al_2O_3 nanocomposite

4.2 SURFACE TENSION AND VISCOSITY

Surface tension and viscosity are two of the most important properties for fluid dynamics. Nonetheless, these critical fluid properties are not available for most metal matrix nanocomposites (MMNCs). Conventionally, surface tension can be measured by various techniques, such as sessile

and pendant drop tests, while viscosity can be measured by viscometers or rheometers. However, measurements of surface tension and viscosity of high-temperature metal melts are rather difficult by traditional methods. Therefore, an innovative measurement system is developed based on the accessible laser system, inspired by the so-called oscillating drop method [Rhim 1999]. This method is advantageous in many aspects:

- It measures surface tension and viscosity simultaneously.
- It is a non-contact technique and thus introduces minimal contaminations.
- A small amount of sample is needed.

4.2.1 Working Principle

The oscillating drop method is based on the damped oscillation of a liquid droplet about its sphere, where surface tension determines the natural frequency and the viscosity determines the damping constant [Rhim 1999]. Therefore, surface tension and viscosity can be measured by analysis of the droplet motions, which is generally achieved by recording of the motions using a high speed camera. Oscillations of an isolated drop can occur in different modes from 1 to infinity. The first mode is always omitted since it only represents the translational movements of the drop. The second mode, representing the axisymmetric oscillations of the drop, is often observed. The higher modes are usually neglected because they damp out much faster than the second mode. Hence, in reality, only the second mode oscillation of the drop is used to determine its surface tension and viscosity. In this case, the diameter of the drop as a function of time is given by,

$$d(t) = d_0 + ae^{-\Gamma t}\sin(2\pi f t + \phi) \qquad (4-1)$$

where d and d_0 are the instantaneous and equilibrium droplet diameters, t is the time, a is the initial amplitude of the oscillation, Γ is the damping constant, f is the oscillation frequency, and ϕ is the initial phase. The natural frequency and the damping constant are respectively related to the surface tension and the viscosity,

$$f = \sqrt{\frac{8\sigma}{3\pi m}} \qquad (4-2)$$

$$\Gamma = \frac{10\pi d_0 \mu}{3m} \qquad (4-3)$$

where σ, μ, and m are surface tension, viscosity and mass of the droplet. Therefore, the surface tension and the viscosity can be determined by the oscillation frequency and the damping constant, which can be obtained by analyzing the second mode oscillation of the droplet.

4.2.2 Experimental Method

Bulk (~1 mm in thickness) metal matrix nanocomposites samples were obtained by electrocodeposition for an extended time (80 hours) under the same experimental conditions as discussed in Chapter 3. Both Ni/Al_2O_3 and Ni/SiC nanocomposite samples were prepared for testing. The samples were then cut and ground to the desired shapes (~2 mm × 2 mm × 0.5mm) for measurements.

The oscillating drop method has several variants, including free falling drop, levitated drop, and micro-gravity drop. Free falling drop method is used in this study because it is easy to implement and free of external perturbation. The new measurement setup is developed as schematically shown in Figure 4-7. A fiber laser with a wavelength of 1070 nm is used to melt the

sample while a linear solenoid is used to initiate the free falling motion of the melt drop. The laser and the linear solenoid are synchronized. Continuous laser heating is carried out at a power of 80 W and a beam diameter of ~1 mm for 2.0 s. The temperature of the sample was determined as ~1500 °C by C-type thermocouple. Immediately after the laser heating ends, the solenoid is activated to force the molten sample flow through an alumina tube with a diameter of ~1.65 mm, introducing initial deformation on the droplet. During the falling period after the drop is freed from the alumina tube, a high speed camera is used to record the damped oscillations of the droplet at a frame rate of 9900 fps, which is at least 10 times of the oscillation frequency of the drop in this study. Eventually, the droplet falls on a cold alumina plate and is collected for mass measurement. The whole process occurs in a transparent chamber filled with argon gas to avoid oxidation.

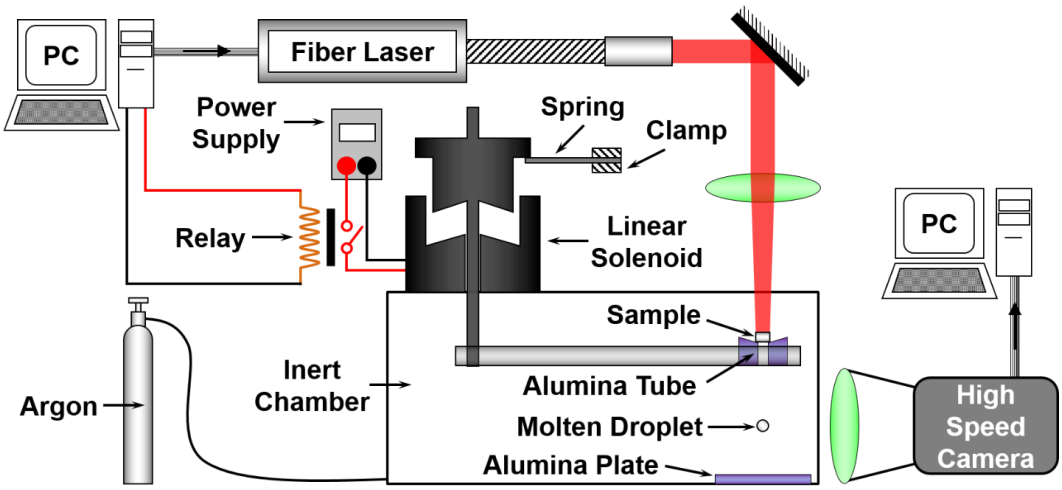

Figure 4-7 Experimental setup for measurement of surface tension and viscosity

4.2.3 Image Processing and Analysis

Image processing is carried out using ImageJ software. Grayscale images corresponding to each frames of a video is converted into the binary format and then processed through morphological erosion and dilation to remove the noise on the droplet contour. Figure 4-8 presents

typical image processing results from the measurement on pure nickel as an example, which clearly shows the oscillations of the droplet. The instantaneous diameter of droplet is a key parameter of interest and can be obtained by an elliptical fitting of the droplet contour. Figure 4-9 shows the droplet diameter as a function of the time from the measurement on pure nickel, where the curve in black is based on the experimental data while the one in blue is the fitting curve using Equation (4-1). By this non-linear curve fitting, the natural frequency and the damping constant can be obtained to determine the surface tension and the viscosity using Equations (4-2) and (4-3).

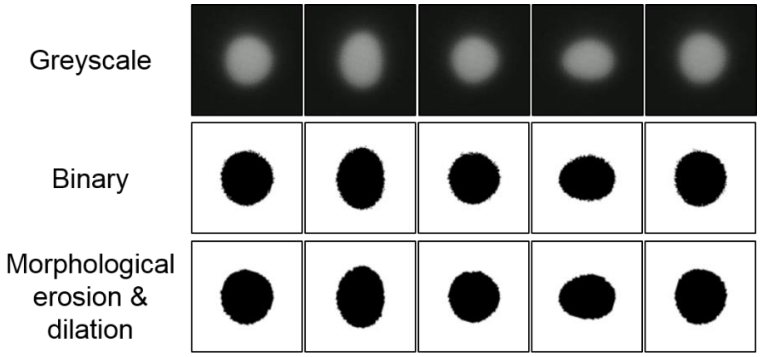

Figure 4-8 Image processing

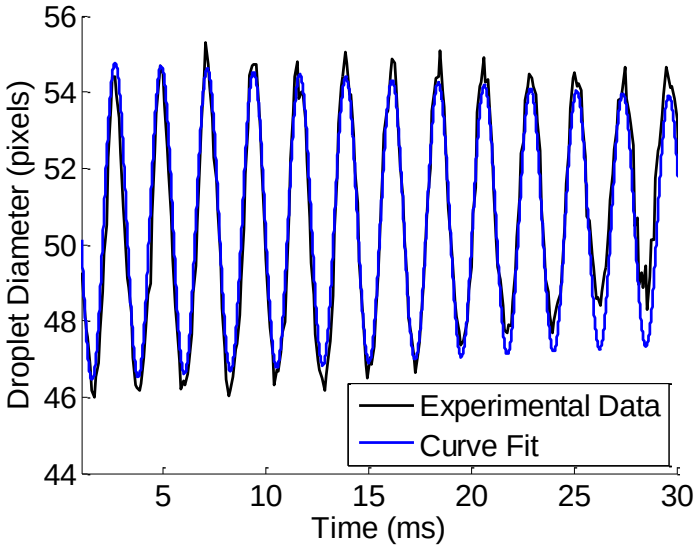

Figure 4-9 Droplet diameter as a function of the time

4.2.4 Experimental Results

Based on the method described above, the surface tension and viscosity were measured on Ni/Al_2O_3 and Ni/SiC nanocomposites as well as pure Ni for comparison. Three tests were performed for each material. The average values and standard deviations were calculated, as shown in Figures 4-10 and 4-11. The surface tension and viscosity of pure Ni match well with those reported from literature [Mills 2002]. The experimental results show that the introduction of nanoparticles into the base metal reduces the surface tension but increases the. It is possible that the nanoparticles in the metal reduce the metallic bonds in the base metal such that the surface tension decreases. A higher viscosity in the nanocomposites is expected since solid nanoparticles are introduced into the liquid metal.

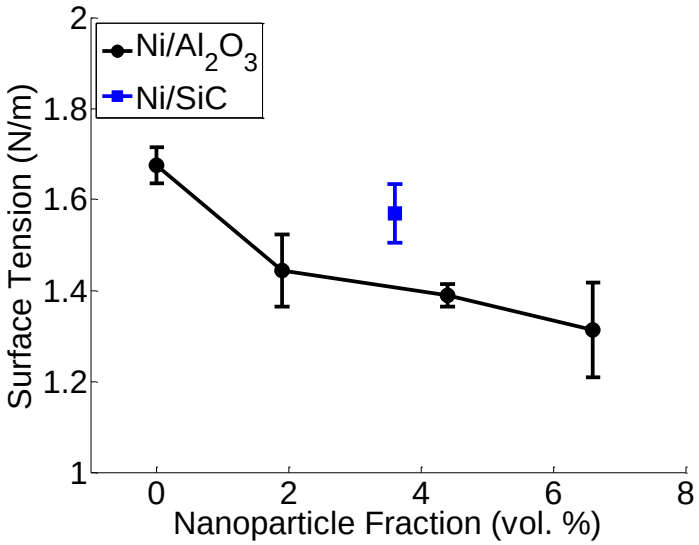

Figure 4-10 Surface tension of pure Ni, Ni/Al_2O_3 and Ni/SiC

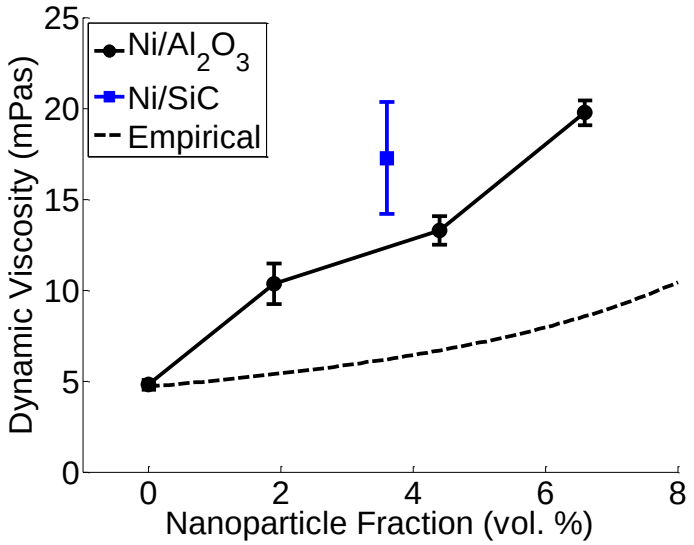

Figure 4-11 Viscosity of pure Ni, Ni/Al_2O_3 and Ni/SiC

Although other studies showed a similar phenomenon of increasing viscosity with nanoparticle additions, the dependence of the effective viscosity on nanoparticle fraction in this study does not follow the empirical correlation obtained from experiments on water- and organics-based nanofluids [Corcione 2011]. It is of remarkable interest to develop more capable models to predict effective surface tension and viscosity of metal matrix nanocomposites (MMNCs). A higher viscosity is beneficial for some laser materials processing techniques, such as laser polishing. Firstly, it is expected that the thermocapillary flow could be suppressed with a higher viscosity since it would be more difficult for the surface tension gradient to overcome viscous stress. Less ripple features would be introduced by suppressing thermocapillary flows and thus surface roughness would be reduced. In addition, the enhanced viscosity would increase the damping efficiency in the capillary regime and therefore the surface roughness could be reduced more significantly. The effect of nanoparticles on laser polishing will be experimentally studied.

4.3 HEAT CAPACITY

The heat capacity is the amount of heat required to raise the temperature by one degree on an object or substance. It is an important thermophysical property for laser heating and cooling. The introduction of nanoparticles can possibly change the heat capacity of the metal. However, the heat capacity data of the nanocomposites of interests are not available. Therefore, both theoretical and experimental studies are conducted to determine the heat capacity of MMNCs.

4.3.1 Theoretical Study

To simplify the theoretical model, the matrix and the nanoparticles are considered as isolated systems when the temperature of a nanocomposite is raised. This assumption is valid if there is no chemical interaction between the matrix and the nanoparticles and the phase transformation behaviors are not altered by each other. The effective heat capacity of the nanocomposite can then be simply calculated as a weighted average of the heat capacities of constituent phases, which is given by

$$c_{P,nc} = \varphi c_{P,np} + (1-\varphi)c_{P,m} \qquad (4-4)$$

where $c_{P,nc}$, $c_{P,np}$, and $c_{P,m}$ are the specific heat capacity of the nanocomposite, the nanoparticles, and the matrix, respectively, and φ is the mass fraction of the nanoparticles. It also can be expressed in terms of the volume fraction.

$$c_{P,nc} = \frac{\psi\rho_{np}c_{P,np} + (1-\psi)\rho_m c_{P,m}}{\psi\rho_{np} + (1-\psi)\rho_m} \qquad (4-5)$$

where ψ is the volume fraction of the nanoparticles, and ρ_{np} and ρ_m are the density of the nanoparticle and the matrix, respectively.

The effective heat capacities of Ni/Al_2O_3 (4.4 vol. %) and Ni/SiC (3.6 vol. %) are estimated based on the specific heat data of Ni, Al_2O_3 and SiC available. Figure 4-12 shows the specific heat capacities of Ni, Al_2O_3 and SiC from literature [Mills 2002, Chase 1998, Snead 2007]. Both nanoparticles (Al_2O_3 and SiC) have much higher specific heat capacities than the matrix (Ni). Theoretically, the effective specific heat capacities of the nanocomposites will be higher than the base metal. Figure 4-13 shows the predicted specific heat capacities of Ni/Al_2O_3 and Ni/SiC nanocomposites in comparison with that of Ni. The specific heat capacities of Ni/Al_2O_3 and Ni/SiC are only slightly higher than that of Ni, indicating that small fractions of nanoparticles do not significantly alter the heat capacities. It is predicted that the specific heat capacity of Ni/Al_2O_3 and Ni/SiC at room temperature is 1.8 % and 0.8 % higher than that of Ni, respectively.

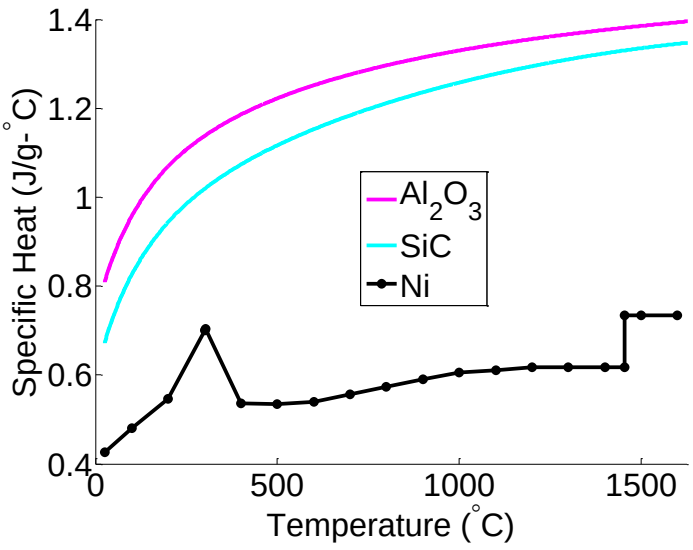

Figure 4-12 Heat capacities of Ni, Al_2O_3 and SiC from literature

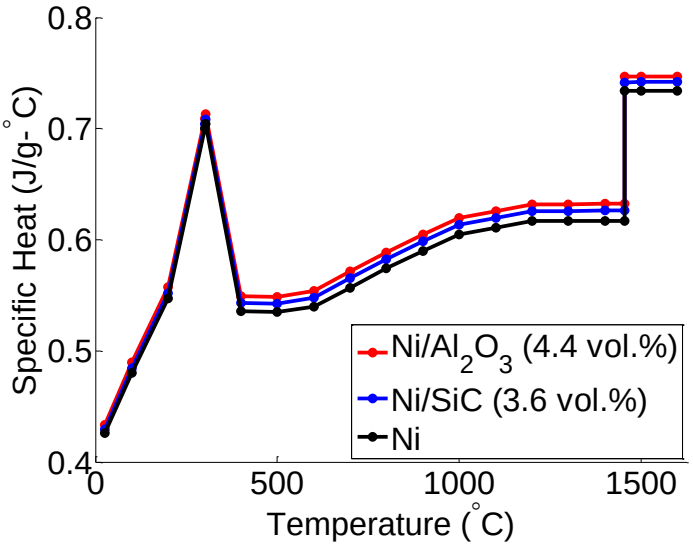

Figure 4-13 Predicted heat capacities of Ni/Al_2O_3 and Ni/SiC in comparison with that of Ni

4.3.2 Experimental Measurement

Differential scanning calorimetry (DSC) is the standard method to measure heat capacity. Commercial DSC equipment (Perkin Elmer Diamond DSC with Intracooler II) was used to experimentally measure the heat capacities of Ni/Al_2O_3 and Ni/SiC nanocomposites as well as Ni for reference at a temperature scan rate of 10 °C/min. The samples were prepared with the same method as used in the surface tension and viscosity measurements. Three DSC tests were conducted for each material, and the average values and standard deviations were then calculated. The specific heat of pure nickel at room temperature was measured to be 0.424 J/g-K in this study. This measurement result agrees well with the value from literature [Mills 2002], 0.426 J/g-K, which validates the experimental method. The experimental results of specific heat measurements at room temperature are shown in Figure 4-14, which sees little significant difference in specific heat among Ni, Ni/Al_2O_3 and Ni/SiC. The variation coefficients, i.e., the standard deviation divided by the mean, of the measurements range from 1.8 % to 3.2 %. These measurement

uncertainties are larger than the predicted differences in the specific heat between the nanocomposites and the base metal. Thus it is believed that the specific heat differences introduced by nanoparticles are not significant.

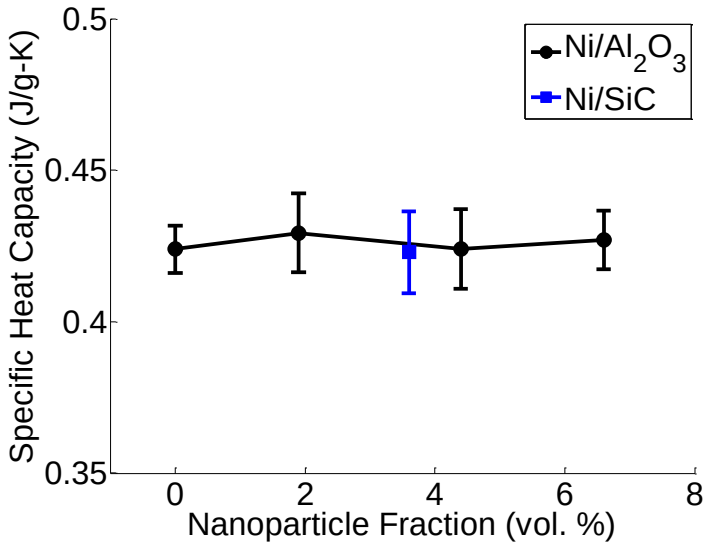

Figure 4-14 Measured specific heat of Ni, Ni/Al_2O_3 and Ni/SiC

4.4 THERMAL CONDUCTIVITY AND DUFFUSIVITY

Thermal conductivity (k) and diffusivity (α) are the thermophysical properties that characterize the capabilities of a material to conduct and diffuse heat, and they are related by volumetric heat capacity (ρc_P).

$$k = \alpha \rho c_P \qquad (4-6)$$

These thermophysical properties determine some crucial outcomes of laser melting process such as the heating and cooling rates, the melt depth and duration, the size of heat affected zone, and thus the microstructure and material performance. It is possible that the introduction of nanoparticles can modify the thermal conductivity and diffusivity since the nanoparticles have

different thermophysical properties from the base metal and introduce interfacial thermal resistance and scattering of energy carriers (i.e., electrons and phonons). Both theoretical and experimental studies are conducted to better understand the nanoparticle effects on thermal conductivity and diffusivity in this study.

4.4.1 Theoretical Prediction

Theoretical prediction of the effective thermal conductivity of a composite material has been investigated for decades because it is motivated by intriguing applications, such as the development of thermoelectric materials and the thermal conductivity enhancement for polymers by the introduction of particles. Therefore, several theoretical, empirical, and semi-theoretical models have been proposed to predict effective thermal conductivity of composites [Nan 1997, Ordonez-Miranda 2011, Faroughi 2015].

Nan et al. introduced an effective medium approach that considered the interfacial thermal resistance between the matrix and the reinforcing phases, and the theory was experimentally validated on various material systems [Nan 1997], making it the most widely accepted method so far. In order to predict the effective thermal conductivity of nanoparticles reinforced materials, i.e., nanocomposites, Faroughi et al. modified the effective medium approach to consider the scattering of the electrons and phonons by nanoparticles [Faroughi 2015]. As a result of combining both Nan's and Faroughi's work, the effective thermal conductivity of a nanocomposite can be expressed as follows.

$$\frac{k_{nc}}{k_m} = \frac{1 + 2X\psi}{1 - X\psi} \qquad (4-7)$$

where k_{nc} and k_m are the thermal conductivity of the nanocomposite and the corresponding base metal respectively, ψ is the volume fraction of the nanoparticles, and X is an intermediate parameter that is given by

$$X = \frac{1 - \frac{k_m}{k_{np}} - \frac{R_{th}k_m}{a}}{1 + \frac{2k_m}{k_{np}} + \frac{2R_{th}k_m}{a}} \quad (4-8)$$

where k_{np} is the thermal conductivity of the nanoparticles, R_{th} is the interfacial thermal resistance between the matrix and the nanoparticles, and a is the radius of the nanoparticles. The thermal conductivities of the matrix and nanoparticles in a nanocomposite are different from those of the homogeneous bulk materials due to the scattering of electrons and phonons by nanoparticles, and thus should be modified in order to be used in Equations (4-7) and (4-8). The heat conduction is contributed by two distinct energy carriers, electrons and phonons, and the effect of nanoparticles on the thermal conductivity by each carrier can be calculated as follows.

$$k_{m,i} = \frac{k_{m,i,bulk}}{1 + \frac{3\psi\Gamma_{m,i,bulk}}{4a}} \quad (4-9)$$

$$k_{np,i} = \frac{k_{np,i,bulk}}{1 + \frac{\Gamma_{np,i,bulk}}{a}} \quad (4-10)$$

where i stands for the energy carrier (either electron or phonon), $bulk$ denotes that a parameter is evaluated based on a bulk material, and Γ is the mean free path of a carrier. With these modified thermal conductivities from Equations (4-9) and (4-10), the scattering effects induced by nanoparticles are included.

In summary, this prediction model for effective thermal conductivity considers all the effects introduced by nanoparticles that are known so far:

- the difference in thermal conductivity between the matrix and the nanoparticles
- the interfacial thermal resistance between the matrix and the nanoparticles
- the scattering of electrons and phonons by nanoparticles

The effective thermal conductivities of Ni/Al_2O_3 nanocomposites with different nanoparticle sizes and fractions were predicted using this method and compared with experimentally measured results. The thermal conductivity of Ni and Al_2O_3 used for this prediction model is 90 W/m-K and 30 W/m-K, respectively. The thermal resistance between Ni and Al_2O_3 of 4.25×10^{-9} m^2K/W is used [Liu 1995]. Figure 4-15 shows the predicted thermal conductivity of Ni/Al_2O_3 as a function of nanoparticle fraction at a radius of 25 nm. In order to evaluate the influence of nanoparticle scattering on the thermal conductivity, the predictions were performed both with and without considering the scattering effects, i.e., Equations (4-9) and (4-10), which are shown as curves in black and blue in Figure 4-15, respectively. Without the scattering effect, the effective thermal conductivity decreases as the nanoparticle fraction increases, which makes sense because the thermal conductivity of Ni is larger than that of Al_2O_3 and the incorporation of nanoparticles introduces an interfacial thermal resistance. With the scattering effect considered, the reduction of thermal conductivity is even more significant, which is also reasonable because the scattering of electrons and phonons decreases the thermal conductivity of each phase.

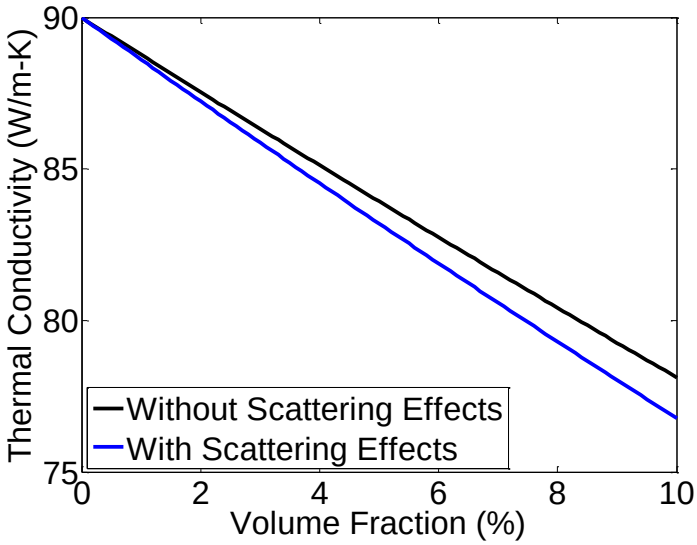

Figure 4-15 Predicted thermal conductivity of Ni/Al_2O_3 as a function of nanoparticle fraction at a radius of 25 nm

In order to study the effect of nanoparticle size on the thermal conductivity of a nanocomposite, the prediction was also carried out with various nanoparticle sizes at a fraction of 4.4 vol. %. Again, this specific nanoparticle fraction was chosen for comparison with experimental measurements. The prediction results are presented in Figure 4-16. At the same fraction of nanoparticles, the effective thermal conductivity deceases with decreasing nanoparticle size since the smaller nanoparticles result in more scattering on the energy carriers and induce more interfacial area for more thermal resistance. It should be noted that the scattering effect becomes dominant at small nanoparticle sizes (e.g. less than 20 nm), where a considerate reduction in thermal conductivity would be realized.

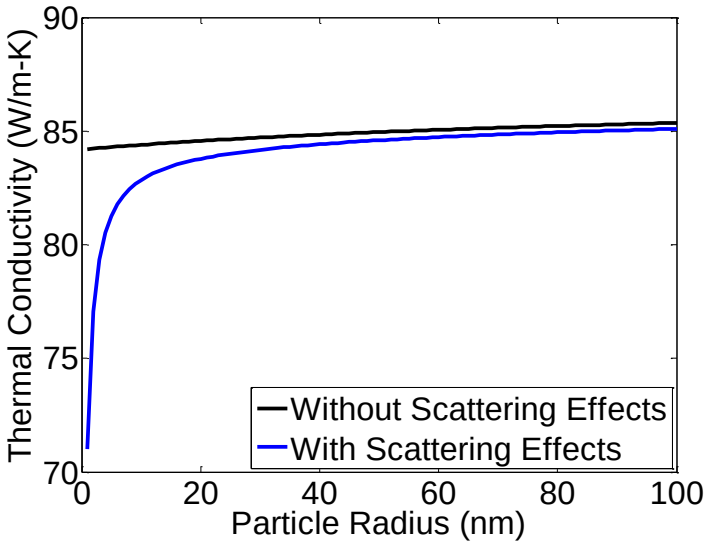

Figure 4-16 Predicted thermal conductivity of Ni/Al2O3 as a function of nanoparticle size at a fraction of 4.4 vol. %

4.4.2 Experimental Measurement

In order to experimentally determine the effective thermal conductivity of the nanocomposites and examine the prediction model, thermal conductivity and diffusivity measurements were carried out using the flash method, which is a standard approach to measure thermal properties [Parker 1961]. The experimental setup is schematically shown in Figure 4-17. A laser pulse is irradiated on the front side of the sample and the resultant transient temperature on the back side is monitored by a K-type thermocouple. A photodiode embedded in the laser system is used to measure the temporal profile of the laser pulse. Both the signals from the thermocouple and the photodiode are acquired by a computer through a data acquisition (DAQ) system. Eventually, the half time of temperature rise at the back side of the sample is used to determine the thermal diffusivity, and the thermal conductivity can be further calculated with the knowledge of volumetric heat capacity by following Equation (4-6).

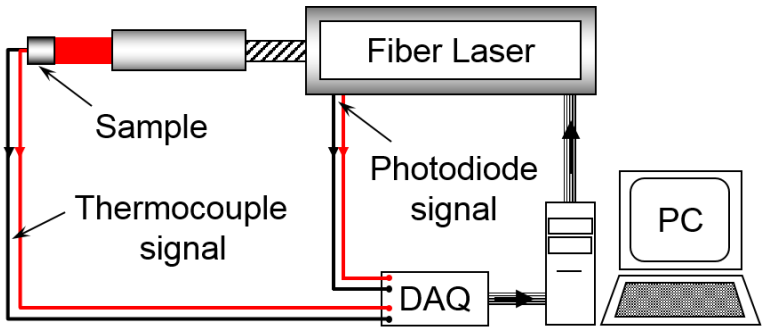

Figure 4-17 Experimental setup for measurements of thermal diffusivity and conductivity

The working principle of the flash method is based on an analytical solution to heat flow equation under the boundary conditions listed below.

(1) The pulse of light is much shorter than the characteristic time of heat diffusion.

(2) The heat diffusion is one-dimensional in the sample, i.e., parallel to the laser beam.

(3) The sample is adiabatic during the measurement.

(4) The sample is homogeneous.

(5) The sample is opaque to light source and to thermal radiation.

The flash method is preferred in many applications because these boundary conditions are relatively easy to realize. With these assumptions satisfied, the temperature on the back side can be analytically resolved as a function of temperature.

$$T(t) = \Delta T \left[1 + 2\sum_{n=1}^{\infty}(-1)^n \, exp\left(-\pi^2 n^2 \frac{t}{t_c}\right)\right] \qquad (4-11)$$

where T is the temperature, t is the time., ΔT is the maximum temperature rise, and t_c is the characteristic time of heat diffusion. The maximum temperature rise ΔT is given by the total heat

input Q divided by the heat capacity of the sample, C, i.e, $\Delta T = Q/C$. The characteristic time of heat diffusion t_c is given by the square of the length of the sample, L^2, divided by the thermal diffusivity α, i.e., $t_c = L^2/\alpha$. The solution can be further simplified by a normalization of the parameters.

$$\Theta(t') = \Delta T \left[1 + 2\sum_{n=1}^{\infty}(-1)^n \, exp(-\pi^2 n^2 t')\right] \qquad (4-12)$$

where Θ is the normalized temperature, $\Theta = T/\Delta T$, and t' is the normalized time, $t' = t/t_c$. The normalized temperature as a function of the normalized time is calculated and plotted in Figure 4-18. The temperature profile has three stages: the temperature remains nearly constant at the beginning of the pulse heating because the heat has not diffused to the back side yet, and then it increases rapidly and finally reaches the maximum. The time at which the normalized temperature rise reaches the half of the maximum is generally used to measure the thermal diffusivity. The half time can be determined from Equation (4-12), which results in $t'_{0.5} = 0.139$, namely, $t_{0.5} = 0.139t_c = 0.139L^2/\alpha$. If the half time $t_{0.5}$ can be experimentally obtained base on the temperature measurements, the thermal diffusivity α can be measured in turn, i.e., $\alpha = 0.139L^2/t_{0.5}$. Accordingly, the thermal conductivity k can be calculated, i.e., $k = \alpha\rho c_P$.

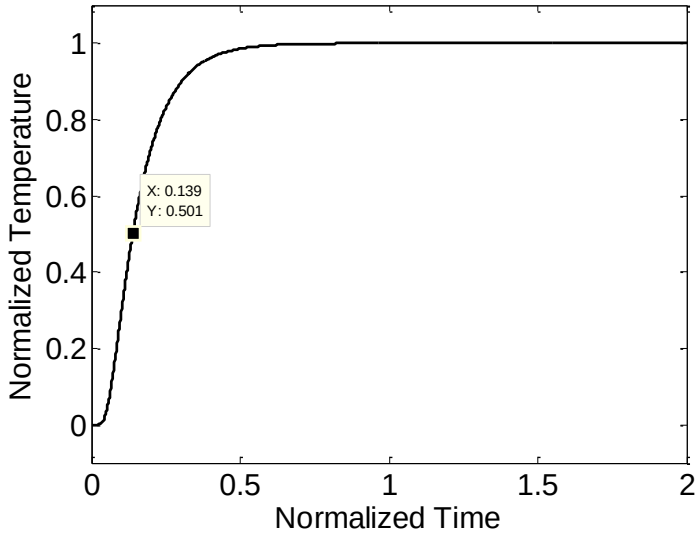

Figure 4-18 The normalized temperature as a function of the normalized time

In order to make accurate measurements of thermal diffusivity and conductivity, the boundary conditions that are responsible for the heat diffusion solution must be fulfilled during experimentation. The first assumption was satisfied by using a short laser pulse (~0.1 s), which is much shorter than the heat diffusion time (>10 s). Although the spatial distribution of the laser intensity is a Gaussian function, the sample was made with a small cross section and a large length such that the heat diffusion time was much smaller in the transverse than the longitudinal directions, resulting in a one-dimensional heat transfer. To fulfil the third condition, the sample was surrounded by a thermal insulation tape. Since the *effective* thermal diffusivity and conductivity of a nanocomposite are of primary interests in this study, the sample can be considered as homogenous although it is made of multiple phases. The last assumption is valid for metallic materials as they have large extinction coefficients. With all the boundary conditions satisfied, the measurements of thermal diffusivity and conductivities were performed on Ni/Al_2O_3 and Ni/SiC as well as Ni for reference. The typical photodiode and the thermocouple signals obtained during

a measurement on Ni/Al_2O_3 are shown in Figure 4-19 as an example. It can be observed that the laser pulse was significant shorter than the heat diffusion time as required by the first assumption. In addition, the measured temperature profile matches exactly with the analytical solution in Figure 4-18, which validated the second and third assumptions.

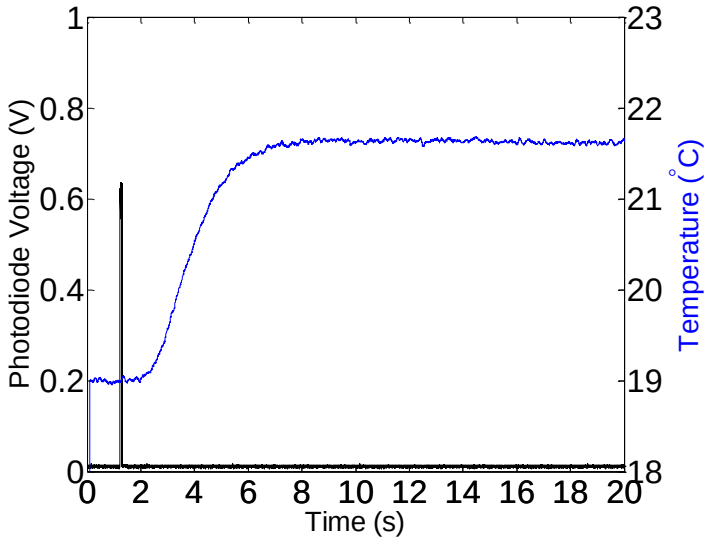

Figure 4-19 Measured photodiode and thermocouple signals

The half time was measured from the temperature profile and then the thermal diffusivity and conductivity were determined. Five measurements were carried out for each material, and the average value and the standard deviations were calculated, which are shown in Figures 4-20 and 4-21. The thermal conductivity of pure Ni was measured as 91.7±2.8 W/m-K, which agrees well with the standard value (90 W/m-K) from the reference [Mills 2002]. Both thermal diffusivity and conductivity of Ni/Al_2O_3 decrease as the nanoparticle fraction increases as predicted by the effective medium theory. In fact, the predicted thermal conductivity of Ni/Al_2O_3 in Figure 4-15 matches well with the measured one in Figure 4-21. It suggests that the prediction model works well for the nanocomposites systems and thus can be used to estimate the effective thermal

conductivity of the metal matrix nanocomposites. It should be noted that the addition of SiC nanoparticles also decreases the thermal conductivity despite that the bulk SiC has a much higher thermal conductivity (490 W/m-K [Snead 2007]) than Ni. It is likely that the effect of interfacial thermal resistance and the scattering of energy carriers dominate in the Ni/SiC nanocomposites.

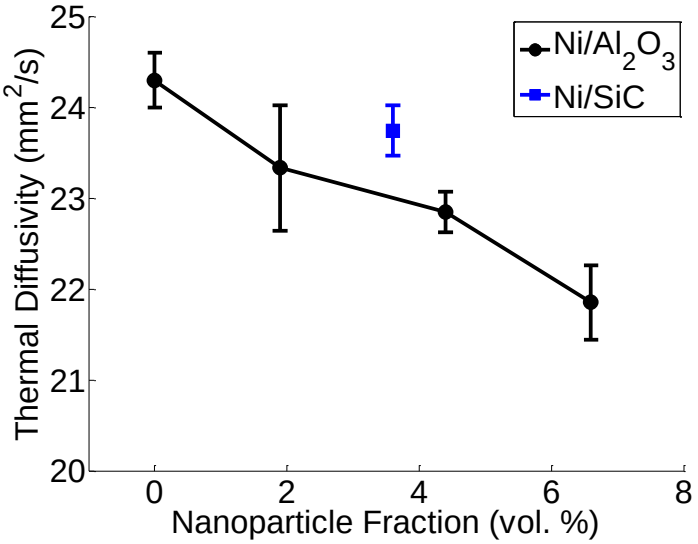

Figure 4-20 Thermal diffusivity of pure Ni, Ni/Al_2O_3 and Ni/SiC

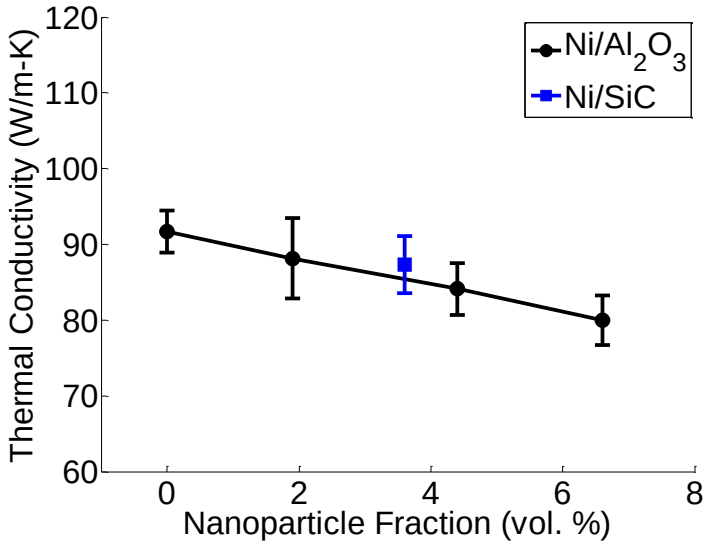

Figure 4-21 Thermal conductivity of pure Ni, Ni/Al_2O_3 and Ni/SiC

It is expected that the reduced thermal conductivity will affect heat transfer during laser heating and cooling to modify the microstructures and properties of the materials. The specific effects will be studied in detail later.

4.5 SUMMARY

Optical and thermophysical properties of Ni/Al_2O_3 and Ni/SiC nanocomposites were experimentally determined, including reflectivity, surface tension, viscosity, heat capacity, and thermal conductivity. The measurements showed that the reflectivity and specific heat of the MMNCs were similar to those of the base metals. However, the thermal conductivity and surface tension of the MMNCs are lower than those of the base metal. Moreover, the viscosity of the MMNCs was significantly higher than that of the base metal. With all these essential properties available, it is extremely beneficial to fundamentally understand the effects of nanoparticles on the laser melting process. Theoretical and experimental studies will be conducted to understand how these altered thermophysical properties would affect the laser melting process and whether some existing limits of laser melting can be overcome.

CHAPTER 5. ANALYTICAL AND EXPERIMENTAL STUDIES ON THERMOCAPILLARY FLOW

With the measured optical and thermophysical properties, theoretical study was performed prior to laser melting experiments in order to provide insights and guidance for experimental design. Firstly, analytical and experimental studies were conducted on Ti6Al4V and a semi-theoretical model was developed to predict the magnitude of thermocapillary flows during laser melting. Ti6Al4V was chosen to establish the model due to three reasons: (a) there had been considerable studies on this material [Ma 2013, Vadali 2013, Pfefferkorn 2013], (b) laser melting of alloys was less complex than that of metal matrix nanocomposites (MMNCs), and (c) its optical and thermophysical properties were readily available from literature. The surface geometries introduced by thermocapillary flows on MMNCs were then predicted using the model and compared with experimental results.

5.1 ANALYTICAL STUDY

The objective of the analytical study is to define and derive a dimensionless number as a function of material properties and process parameters to quantify the magnitude of thermocapillary flow in laser melting. A dimensionless number, called the normalized average displacement of a liquid particle in a single laser pulse, is proposed and derived via analytical heat transfer and fluid flow equations.

5.1.1 Modeling Approach

In pulsed laser melting processes, a short duty cycle is usually used. Therefore it is reasonable to assume that the material cools down to its initial temperature (room temperature in the current work) before being heated by the next laser pulse. Transient heat transfer simulations that include laser heating and heat dissipation phases support this assumption [Ma 2013]. Hence, modeling surface melting induced by a single laser pulse and subsequent solidification is sufficient to represent the process. Both the fluid flow and heat transfer models will base on a single pulse. To simplify the model, the material is assumed homogeneous and isotropic. The material properties are assumed constant (temperature independent). Chemical reaction is assumed not to occur since a protective gas is generally applied during laser melting. Ablation is not modelled because laser melting is conducted below the boiling temperature. The pressure and shear stress of the shielding gas and the recoil pressure due to the evaporation of the liquid metal have a negligible effect on the melt pool for the experimental design used in this study. Hence, these effects are not included in the model. The following sections will present the two separate analytical models for fluid flow (thermocapillary flow) and heat transfer of the laser-induced melt pool.

5.1.2 Fluid Flow Model

To quantify the extent (magnitude) of thermocapillary flow, the following features and phenomena must be taken into account: the melt pool geometry (shape, depth and width), the driving force (surface tension gradient), the resistant force (viscous stress), the average velocity, and the flow duration. A useful parameter for quantification of thermocapillary flow should cover the effect of the above-mentioned features and phenomena as much as possible and be easily

derived and calculated from analytical models. In addition, a dimensionless number will be ideal because it can be applied more broadly. In this work, the normalized average displacement of a liquid particle is defined as the key dimensionless parameter to describe the extent of thermocapillary flow. More specifically, it is the average displacement (averaged over the melt duration) of a liquid particle divided by the melt pool radius:

$$l_n = \frac{\overline{v_s}\,\overline{t_m}}{\overline{r_m}} \qquad (5-1)$$

where, $\overline{v_s}$ is the average surface velocity as shown in Figure 5-1, $\overline{t_m}$ is the average melt duration, and $\overline{r_m}$ is the average melt pool radius also shown in Figure 5-1. All the *average* values in this work are averaged over the melt duration if not specifically stated. The dimensionless number is actually the displacement of a liquid particle relative to the melt radius, hence indicative of the amount of liquid particles that reach the boundary and thus the extent of the melt pool flow.

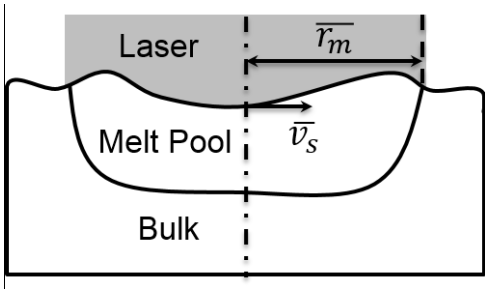

Figure 5-1 Schematics of thermocapillary flow during laser melting

In Equation (5-1), $\overline{v_s}$ can be approximated by considering the force balance that governs thermocapillary flow. Assuming a flat surface,

$$-\frac{d\sigma}{dT}\frac{\partial T}{\partial r} = \mu\frac{\partial v_r}{\partial z} \qquad (5-2)$$

where σ is the surface tension, T is the temperature, r and z are the positions, μ is the dynamic viscosity, and v_r is the velocity in the radial direction. The left hand side of Equation (5-2) is the surface tension gradient: the driving force of thermocapillary flow. The right hand side of Equation (5-2) represents viscous stress, the force resisting the movement of liquid. The partial derivatives in Equation (5-2) can be approximated by the corresponding average values.

$$\frac{\partial v_r}{\partial z} \approx \frac{\overline{v_s}}{\overline{d_m}} \tag{5-3}$$

$$\frac{\partial T}{\partial r} \approx \frac{\overline{\Delta T}}{\overline{r_m}} \tag{5-4}$$

where, $\overline{d_m}$ is the average melt depth, and $\overline{\Delta T}$ is the average surface temperature difference between the center and the boundary of the melt pool. Combining Equations (5-1)–(5-4), the normalized average displacement is expressed as:

$$l_n = -\frac{d\sigma}{dT}\frac{\overline{\Delta T}\,\overline{d_m}\,\overline{t_m}}{\mu\overline{r_m}^2} \tag{5-5}$$

To calculate l_n with Equation (5-5), the values of $\overline{\Delta T}$, $\overline{d_m}$, $\overline{t_m}$ and $\overline{r_m}$ will be determined from the analytical heat transfer model.

5.1.3 Heat Transfer Model

The objective of the heat transfer model is to calculate the transient temperature field of the melt pool and consequently the values of $\overline{\Delta T}$, $\overline{d_m}$, $\overline{t_m}$ and $\overline{r_m}$ can be determined. The analytical model of heat transfer in laser melting accounts for phase change using the equivalent heat capacity method. The equivalent volumetric heat capacity $c_V{}'$ is defined as:

$$c_V{}' = \rho(c_p + \frac{L}{T_b - T_0}) \qquad (5-6)$$

where, ρ is the density, c_p is the specific heat capacity, L is the specific latent heat, T_b is the boiling temperature, and T_0 is the initial temperature. This method assumes that latent heat is evenly distributed from the initial temperature to boiling temperature. The equivalent heat capacity would be a fairer estimate if the maximum temperature was used instead of boiling temperature in Equation (5-6). The present method underestimates the heat capacity in the liquid phase because the maximum temperature is less than the boiling temperature in laser melting. But it overestimates the heat capacity in the solid phase because $c_V{}' = \rho c_p$ for solid. These two effects will cancel each other to some extent.

The heat conduction is assumed to be one-dimensional, which is valid if

$$\alpha\tau \ll {r_b}^2 \qquad (5-7)$$

where, α is the thermal diffusivity, τ is the pulse duration, and r_b is the laser beam radius. Equation (5-7) is satisfied for most materials if $\tau < 10\ \mu s$ and $r_b > 10\ \mu m$, which are common operational conditions for the experimental design in this work. The advective heat transfer in the liquid phase and the heat losses from convection and radiation on the surface are neglected since they are not significant when compared with heat conduction into the bulk of a part. Laser irradiation is considered as a surface heat source because metal alloys have high absorptive index. The schematic of the model is shown in Figure 5-2.

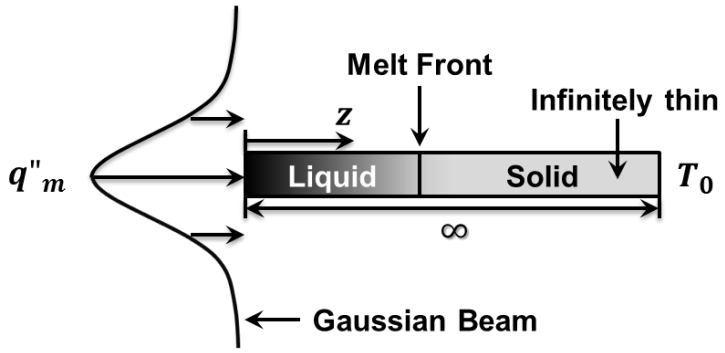

Figure 5-2 Schematics of one-dimensional heat transfer model of laser melting

Based on the assumptions, the transient temperature field is governed by the one-dimensional conduction equation:

$$\frac{\partial T}{\partial t} = \alpha \frac{\partial^2 T}{\partial z^2} \qquad (5-8)$$

where, t is the time, z is the position (depth from the surface), and the z-axis points into the material and $z = 0$ at the surface. The boundary conditions are surface heating given by Fourier's law and constant temperature at infinite depth:

$$-k\frac{\partial T}{\partial t}(z = 0, t) = \alpha_A q"(t) \qquad (5-9)$$

$$T(z = \infty, t) = T_0 \qquad (5-10)$$

where, k is the thermal conductivity, α_A is the laser absorptivity, and $q"$ is the laser-induced heat flux. Assuming laser power is constant during a laser pulse, $q"(t)$ is expressed as:

$$q"(t) = \begin{cases} q"_m, & 0 \le t \le \tau \\ 0, & t > \tau \end{cases} \qquad (5-11)$$

where, $q"_m$ is the laser heat flux while laser pulse is on. For a Gaussian laser intensity distribution with a beam radius r_b at $1/e^2$, laser heat flux at the center of the beam is:

$$q"_m = \frac{2P}{\pi {r_b}^2} \qquad (5-12)$$

where, P is the laser power. The initial condition defines the temperature of the entire domain at the moment the laser pulse starts,

$$T(z, t=0) = T_0 \qquad (5-13)$$

By solving Equations (5-8)–(5-13), while the laser pulse is on ($0 \le t \le \tau$), the temperature field is given by:

$$T = \frac{4\alpha_A P\sqrt{t}\, I_{erfc}\left(\frac{z}{2\sqrt{\alpha t}}\right)}{\pi {r_b}^2 {c_V}'\sqrt{\alpha}} + T_0 \qquad (5-14)$$

where, $I_{erfc}(x)$ is the integral of the complementary error function. Numerical values of $I_{erfc}(x)$ are tabulated [Abramovitz 1970, Carlslaw 1988]. After the laser pulse ends ($t > \tau$), the temperature field is given by superposition of a power input starting at $t = 0$ and the same but negative power input starting at $t = \tau$:

$$T = \frac{4\alpha_A P\left[\sqrt{t}\, I_{erfc}\left(\frac{z}{2\sqrt{\alpha t}}\right) - \sqrt{t-\tau}\, I_{erfc}\left(\frac{z}{2\sqrt{\alpha(t-\tau)}}\right)\right]}{\pi {r_b}^2 {c_V}'\sqrt{\alpha}} + T_0 \qquad (5-15)$$

Knowing the transient temperature field from Equations (5-14) and (5-15), the values of $\overline{\Delta T}$, $\overline{d_m}$, $\overline{t_m}$ and $\overline{r_m}$ can be determined.

5.1.3.1 Average Surface Temperature Difference

$\overline{\Delta T}$ is the average surface temperature difference between the center and the boundary of the melt pool. The temperature at the melt pool boundary remains constant and is equal to the melting temperature T_m. The surface temperature at the center of the melt pool increases from T_m to a maximum T_{max} and then decreases from T_{max} to T_m. If the average boundary temperature is T_m and the average center temperature is assumed to be the arithmetic average between T_m and T_{max}, $\overline{\Delta T}$ is given by:

$$\overline{\Delta T} = \frac{T_{max} - T_m}{2} \qquad (5-16)$$

The maximum temperature occurs at the center ($r = 0$) of the melt pool surface ($z = 0$) at the end of a laser pulse ($t = \tau$). Substituting $r = 0$, $z = 0$, $t = \tau$ and $T = T_{max}$ in Equation (5-14),

$$T_{max} = \frac{4\alpha_A P}{\pi^{1.5} {r_b}^2 {c_V}'} \sqrt{\frac{\tau}{\alpha}} + T_0 \qquad (5-17)$$

For simplicity, temperature is normalized in the following way:

$$\Theta = \frac{T - T_0}{T_n} = \frac{T - T_0}{T_{max} - T_0} \qquad (5-18)$$

where, Θ is the normalized temperature and T_n is the normalizing temperature and chosen as the maximum temperature change.

$$T_n = T_{max} - T_0 = \frac{4\alpha_A P}{\pi^{1.5} {r_b}^2 {c_V}'} \sqrt{\frac{\tau}{\alpha}} \qquad (5-19)$$

In this manner, $\overline{\Delta T}$ can be expressed as:

$$\overline{\Delta T} = \frac{(1 - \Theta_m)T_n}{2} \qquad (5-20)$$

where, Θ_m is the normalized melting temperature as following:

$$\Theta_m = \frac{T_m - T_0}{T_n} \qquad (5-21)$$

5.1.3.2 Average Melt Pool Radius

As the result of a single laser pulse, the melt pool radius increases from zero to a maximum r_m, and then decreases to zero again. As a first approximation, r_m is assumed equal to the laser beam radius, r_b.

$$r_m = r_b \qquad (5-22)$$

The average melt pool radius is assumed half of the maximum:

$$\overline{r_m} = \frac{r_b}{2} \qquad (5-23)$$

5.1.3.3 Average Melt Depth and Melt Duration

As with the average melt pool radius, the average melt depth is taken as half of the maximum value. The average melt duration is defined as full width at half maximum [Perry 2009a]. Unfortunately, explicit solutions to melt depth and duration are not available because the complementary error function is present. However, the dimensionless average melt depth d'_m and melt duration t'_m only depend on Θ_m if they are normalized in the following ways:

$$\overline{d'_m} = \frac{\overline{d_m}}{\sqrt{\alpha\tau}} \qquad (5-24)$$

$$\overline{t'_m} = \frac{\overline{t_m}}{\tau} \quad (5-25)$$

$\overline{d'_m}$ and $\overline{t'_m}$ are obtained for various Θ_m and fitted by exponential functions (Figure 5-3). The coefficients of determination R^2 are 0.98 and 0.99 for $\overline{d'_m}$ and $\overline{t'_m}$, respectively. The fitting functions are:

$$\overline{d'_m} = 2.28exp(-3.78\Theta_m) \quad (5-26)$$

$$\overline{t'_m} = 11.30exp(-5.02\Theta_m) \quad (5-27)$$

Combining Equations (5-24)–(5-27), the complete analytical solutions for average melt depth and melt duration can be obtained.

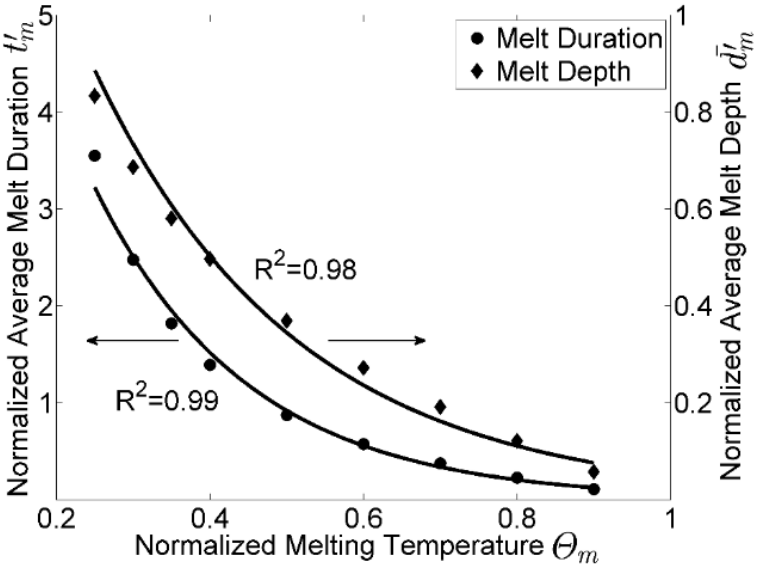

Figure 5-3 Normalized average melt duration and normalized average melt depth as a function of normalized melting temperature

5.1.4 Calculation of Normalized Average Displacement

Combining the heat transfer and fluid flow models, i.e., substituting Equations (5-19), (5-20) and (5-23)–(5-27) into Equation (5-5), the normalized average displacement is given by:

$$l_n = -18.51\frac{d\sigma}{dT}\frac{\alpha_A P\tau^2}{\mu c_V' r_b^4}(1-\Theta_m)exp(-8.80\Theta_m) \qquad (5-28)$$

All the values that determine the dimensionless number l_n in Equation (5-28) are either material properties or process parameters except the dimensionless melting temperature Θ_m. However, Θ_m can be determined by Equations (5-19) and (5-21) with material properties or process parameters. Therefore, derivation of the normalized average displacement is complete. Given a material, the normalized average displacement l_n is a function of laser power, pulse duration and beam radius. The relationship between the dimensionless number l_n and laser parameters for Ti6Al4V is plotted in Figure 5-4. Constant material properties are used for these calculations as listed in Table 5-1. The dimensionless number l_n increases as laser power and pulse duration increase and beam radius decreases; it is most sensitive to beam radius and least sensitive to laser power.

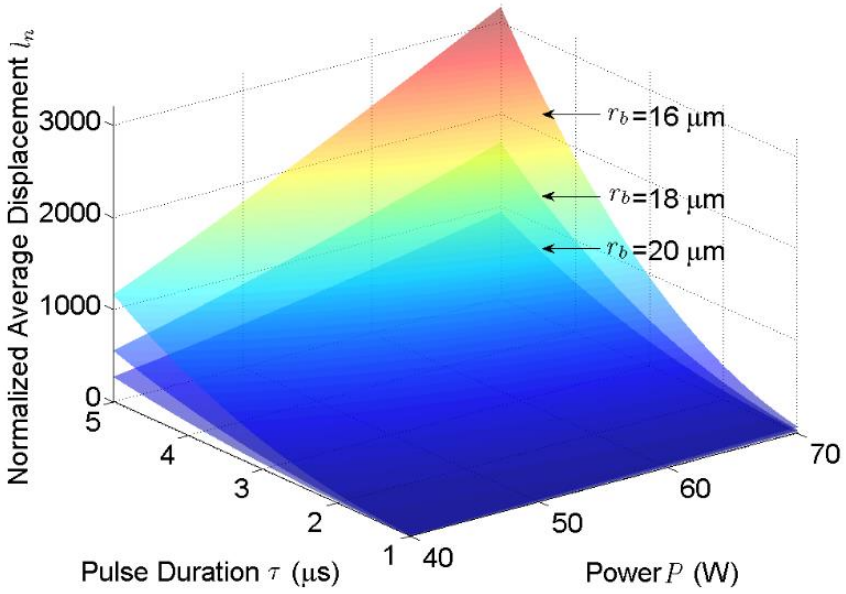

Figure 5-4 Normalized average displacement as a function of laser power (P), pulse duration (τ), and beam radius (r_b) for Ti6Al4V

Table 5-1 Material properties of Ti6Al4V used in this study

Surface Tension Coefficient (N/m-K)	-0.26×10^{-3}	[Smithells 2004]
Dynamic Viscosity (Pa-s)	5×10^{-3}	[Rai 2007]
Thermal Conductivity (W/m-K)	31	[Mills 2002]
Equivalent Volumetric Heat (J/m^3-K)	2.43×10^{6}	[Mills 2002]
Thermal Diffusivity (m^2/s)	1.26×10^{-5}	[Mills 2002]
Laser Absorptivity	0.54	[Kwon 2012]
Initial (Room) Temperature (K)	298	-
Melting Temperature (K)	1928	[Rai 2007]

5.2 EXPERIMENTAL STUDY

5.2.1 Experimental Method

Laser melting experiments on Ti6Al4V alloy were carried out with various process parameters. Initial surfaces on the Ti6Al4V samples were produced using micro end milling with a 2-flute, 1-mm-diameter, tungsten-carbide (WC) tool at a spindle speed of 40,000 rpm and 800 mm/min feed rate. The basic experimental setup for laser melting is illustrated in Figure 5-5. A 1070 nm fiber laser (SPI Lasers, Model: SP-200C-W-S6-A-B) was used for experimentation. The laser was directed into a scan head (ScanLab HurryScan 14 mm) to allow for high-speed, two-dimensional scan at a beam velocity of up to 1.5 m/s. The scan head was controlled by a ForeSight control card (LasX Industries) and furnished with an f-theta objective (Linos f-theta-Ronar, Model: 4401-302-000-20/21) with a focal length of 100 mm. A z-axis manual stage was used to adjust the laser spot size and accommodate samples of various thicknesses.

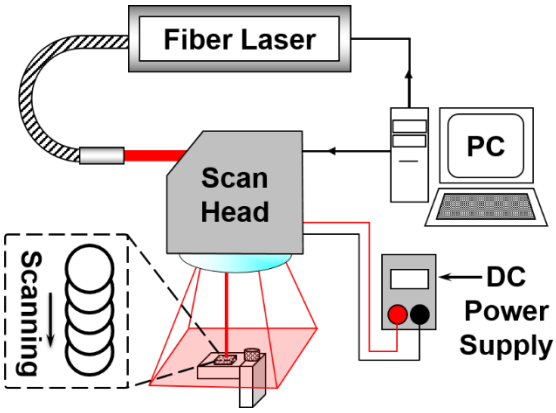

Figure 5-5 Experimental setup for laser melting

Surface profiles were measured using a white light interferometer. The interferometry technique also captures the tilt of a surface. The mean plane was computed with the method of least squares. The height data were plotted after subtraction of the mean plane. The surface topography of a micro milled Ti6Al4V sample is shown in Figure 5-6 as an example.

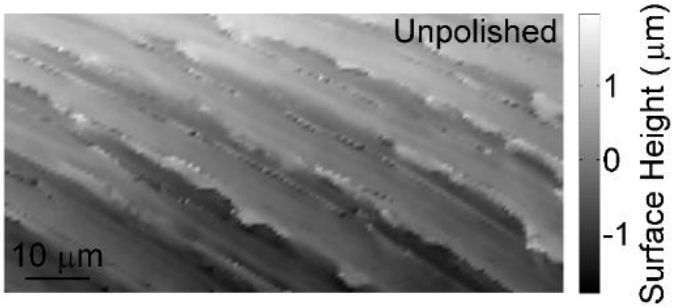

Figure 5-6 Surface topography of a micro milled Ti6Al4V sample

5.2.2 Experimental Results

Figure 5-7 shows the surface profiles of Ti6Al4V samples melted with various laser beam radii (17.7−24.0 μm), and constant pulse duration (1.56 μs) and power (48.6 W). The magnitude of surface features introduced by thermocapillary flow decreases significantly as the laser beam radius increases. While the beam radius increases to 24.0 μm, the introduced features are barely

visible and thus the surface profile is dominated by the original machined features. The experimental measurements herein agree well with the prediction of the extent (magnitude) of thermocapillary flow from the present model.

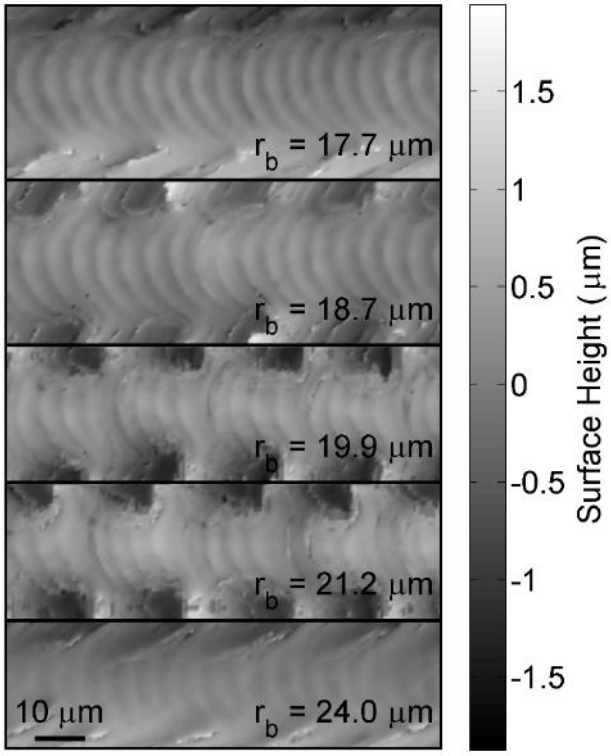

Figure 5-7 Surface profiles after laser melting with various laser beam radii (r_b), and constant pulse duration (1.56 μs) and power (48.6 W)

Figure 5-8 shows the polished surface profiles of Ti6Al4V samples with various pulse durations (2.40−4.20 μs), and constant beam radius (21.2 μm) and power (25.0 W). The magnitude of the introduced surface features increases as the pulse duration increases, which also matches the prediction from the model.

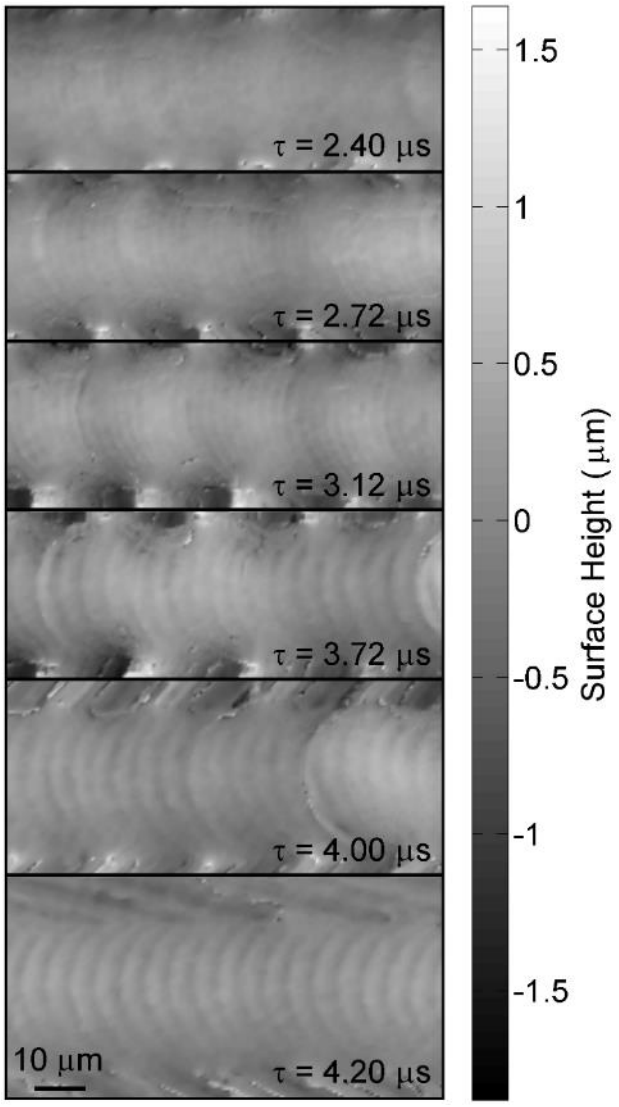

Figure 5-8 Surface profiles after laser melting with various laser pulse durations (τ), and constant beam radius (21.2 μm) and power (25.0 W)

Figure 5-9 shows the effect of laser power (46.0–68.4 W) on the polished surface profiles with constant beam radius (21.2 μm) and pulse duration (1.56 μs). The introduced features become more and more significant as the laser power increases, which again agrees with what the model predicts.

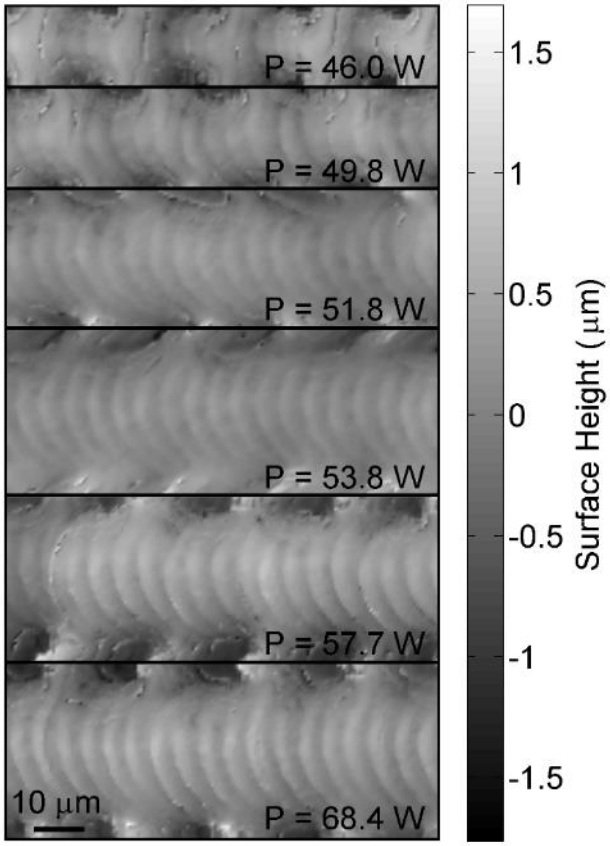

Figure 5-9 Surface profiles after laser melting with various laser powers (*P*), and constant beam radius (21.2 μm) and pulse duration (1.56 μs)

5.3 CORRELATION BETWEEN THE ANALYTICAL MODEL AND THE EXPERIMENTAL RESULTS

To experimentally quantify the extent (magnitude) of thermocapillary flow in laser melting, the geometrical parameters of the features introduced by thermocapillary flow can be evaluated. A line profile of laser melted surface is shown in Figure 5-10 as an example, which is taken along the center line of a laser melting mark. As a first approximation, the line profile can be modelled as a periodic triangle function, which can be defined by the wavelength and the slope. The wavelength is the laser scan velocity divided by pulsing frequency, independent of thermocapillary flow. The slope is the more important piece of information that indicates the extent (magnitude)

of thermocapillary flow [Pfefferkorn 2013]. The slope of the introduced features increases as the magnitude of thermocapillary flow increases. The slope of the introduced features was acquired based on the frequency spectrum of the line profile and compared with the calculated dimensionless number, normalized average displacement.

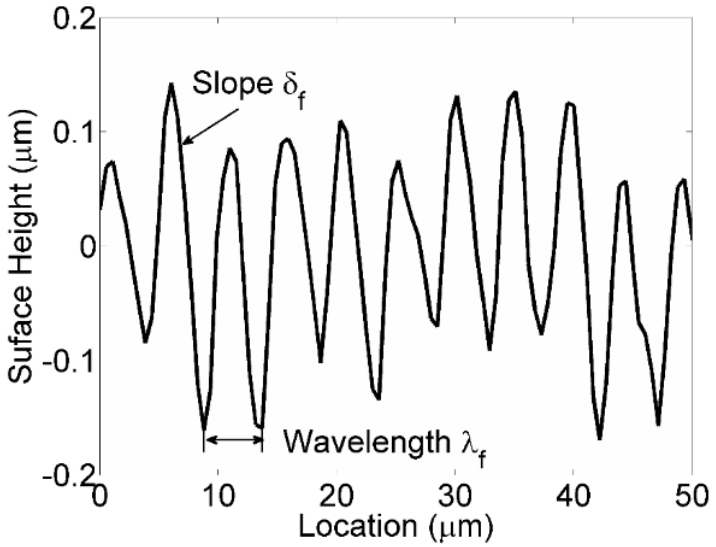

Figure 5-10 A line profile of laser melting mark

Figures 5-11, 5-12, and 5-13 show the comparisons between the normalized average displacement l_n (predicted) and the introduced feature slope δ_f (measured) as functions of laser beam radius, pulse duration and power, respectively. The values of the introduced feature slope were calculated based on the experimentally measured surface profiles shown in Figures 5-7, 5-8, and 5-9. As shown in the plots, l_n and δ_f follow almost the same curve in all the cases.

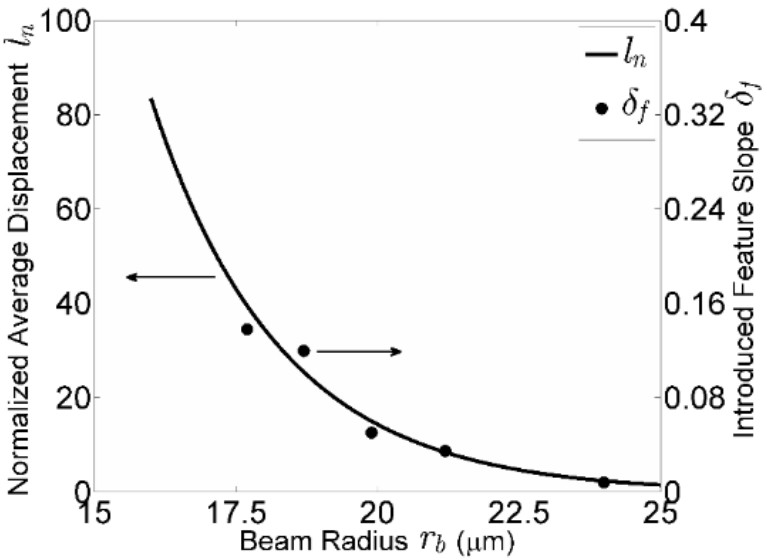

Figure 5-11 Normalized average displacement and introduced feature slope as functions of laser beam radius (1.56 μs pulse duration and 48.6 W power)

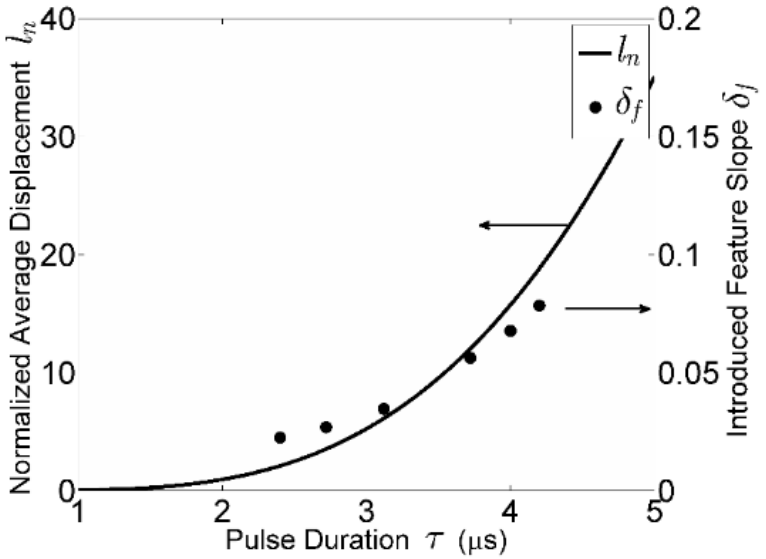

Figure 5-12 Normalized average displacement and introduced feature slope as functions of laser pulse duration (21.2 μm beam radius and 25.0 W power)

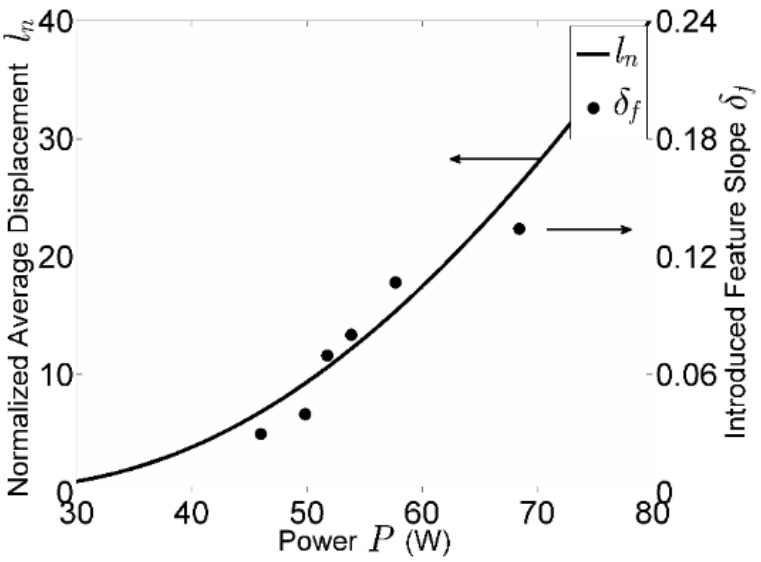

Figure 5-13 Normalized average displacement and introduced feature slope as functions of laser power (21.2 μm beam radius and 1.56 μs pulse duration)

As shown in Figures 5-11, 5-12, and 5-13, l_n and δ_f appear to be closely correlated since they follow highly similar trends as a function of all three laser parameters. Figure 5-14 plots δ_f as a function of l_n and a linear fit with a proportional coefficient. The coefficient of determination R^2 is 0.80, which indicates a strong correlation between l_n and δ_f. The fitting function is given by:

$$\delta_f = 0.00445 l_n \qquad (5-29)$$

The high quality of fitting confirms that l_n is an indicator for δ_f and thus the extent (magnitude) of thermocapillary flow. As mentioned, in the presence of thermocapillary flow, the liquid metal move outward from the center of the melt pool, and resolidifies, piles up and forms a ridge at the boundary of the melt pool. The additional features introduced by thermocapillary flow are actually due to overlaps of these solidified ripples. Since the normalized average displacement describes the amount of the material that has moved during melting, it is not surprising to see the

strong relationship between the normalized average displacement and the introduced feature slope. A greater normalized displacement indicates more material that has moved from the center to the boundary of the melt pool, and thus a steeper ripple and eventually a greater slope of the introduced features.

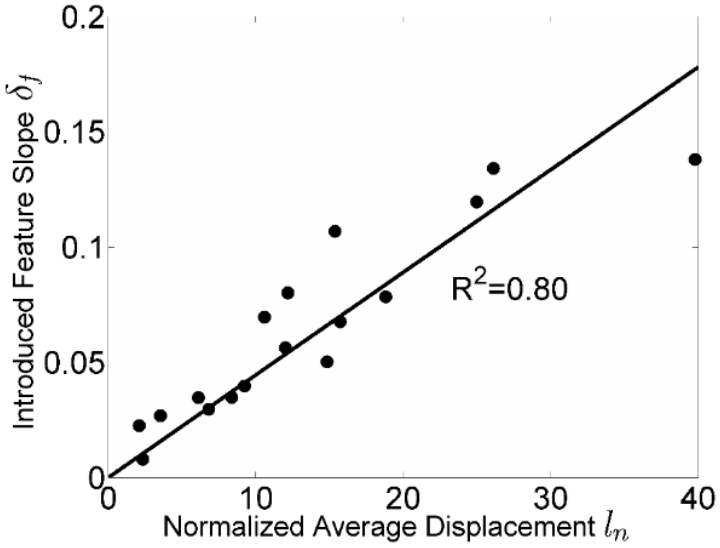

Figure 5-14 Introduced feature slope as a function of normalized average displacement

5.4 PREDICTION OF SURFACE PROFILE

Since there is a strong relationship between the dimensionless number l_n and the introduced feature slope δ_f, the relationship can be directly used to predict the slope δ_f. With the knowledge of the slope, it is straightforward to predict the geometry of the features introduced by thermocapillary flow because the wavelength of the periodic triangle function is simply the laser scan velocity divided by pulsing frequency. Eventually, the surface roughness that is contributed by the thermocapillary flows can be predicted. The residual surface roughness from the original asperities is not predicted in this model, and therefore the model predicts the lower bound of the roughness.

The prediction of the surface roughness induced by thermocapillary flows was performed on pure Ni and Ni/Al_2O_3 nanocomposites with various nanoparticle fractions. The measured optical and thermophysical properties were used as the input parameters for the model. The process parameters used in the model are the actual ones that would be used for the validation of the model, including a scan velocity of 0.4 m/s, a pulsing frequency of 100 kHz, and a melt pool diameter of 30 μm. The predicted and measured surface profiles are shown in Figure 5-15.

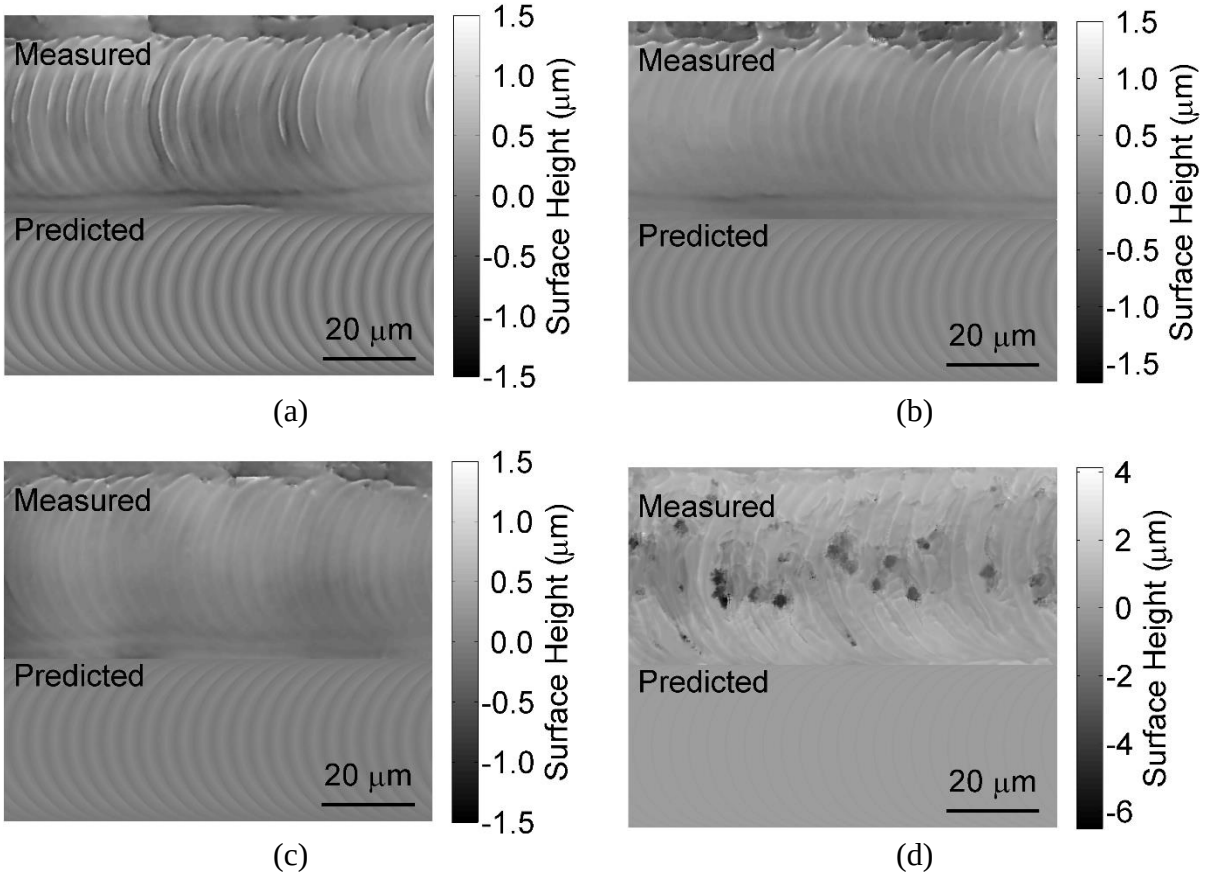

Figure 5-15 Predicted and measured surface profiles: (a) pure Ni, (b) Ni/Al_2O_3 (1.9 vol. %), (c) Ni/Al_2O_3 (4.4 vol. %), and (d) Ni/Al_2O_3 (6.6 vol. %)

The predicted and measured surface profiles match well in all cases except for Ni/Al_2O_3 (6.6 vol. %) on which many voids are present after laser melting. It is believed that the large

amount of Al_2O_3 nanoparticles in this material might have agglomerated during laser melting, ejected from the melt pool and then decomposed under direct laser heating to form the porosity on the surface. The ejection process could have disturbed the melt pool flow and therefore resulted in random surface profiles in the area adjacent to the holes. The exact mechanism responsible for the porosity formation requires further rigorous investigation. Nonetheless, in the other cases where porosity did not occur, the predicted surface profiles agree well with measured ones. It is even more convincing to compare the surface roughness values calculated from the surface profiles with the measured ones as shown in Figure 5-16. Again, the predicted and measured roughnesses match well except for the nanocomposites with the high nanoparticle fraction. The comparison between the predicted and measured results suggests that the prediction model works well, at least at low fractions of nanoparticles.

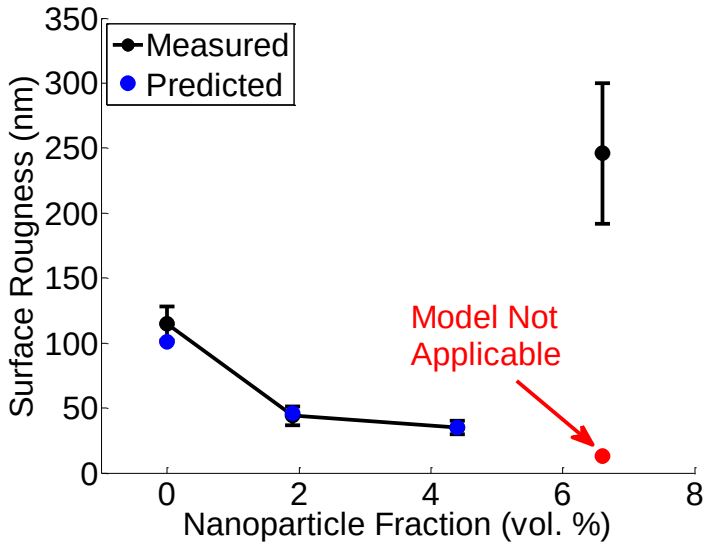

Figure 5-16 Predicted and measured surface roughnesses

The model successfully predicted the difference between Ni and Ni/Al_2O_3 at low nanoparticle fractions using the measured optical and thermophysical properties. As shown in

Figure 5-16, the surface roughness of Ni/Al_2O_3 (1.9 vol. % or 4.4 vol. %) is much lower than that of Ni, validating that the thermocapillary flows are suppressed by the addition of nanoparticles. The nanoparticles significantly increased the viscosity of the melt to resist the flows induced by surface tension gradient. As reviewed in Chapter 2, the thermocapillary flow plays an important role in laser polishing process as an emerging application of laser melting. The suppression of thermocapillary flows extends the capillary regime of laser polishing, which would result in a much smoother surface. Therefore, it is possible to break the existing limit of laser polishing by the introduction of nanoparticles. A more rigorous study on laser melting of Ni/Al_2O_3 (4.4 vol. %) will be presented in Chapter 6 since this nanoparticle fraction provides the best surface finish in the preliminary study.

5.5 SUMMARY

An analytical heat transfer and fluid flow model was derived to calculate the normalized average displacement of a fluid particle to quantify the magnitude of thermocapillary flow. The normalized average displacement is a dimensionless number which is an indicator of the amount of the moved material and thus the deformation of the surface profile. Experimental results showed that the thermocapillary flow increased as the laser beam radius decreased, and the pulse duration and the power increased, which agreed with the predictions from the model. The normalized average displacement and the measured slope of the features introduced by thermocapillary flow were found to be strongly correlated, and a correlation was obtained by linear regression.

The correlation was then used to predict the surface profiles introduced by thermocapillary flows and the corresponding surface roughnesses on Ni and Ni/Al_2O_3 (1.9 vol. %, 4.4 vol. % and

6.6 vol. %). Both the predictions and the measurements showed that the thermocapillary flows were successfully suppressed by addition of nanoparticles. The suppression of thermocapillary flows can potentially provide great benefits to laser polishing process and even break the existing limit, which will be investigated in next chapter.

CHAPTER 6. LASER MELTING OF METAL MATRIX NANOCOMPISTES

Systemic laser melting experiments were conducted at various laser fluences to explore the feasibility of tuning heat transfer and fluid flow process by nanoparticles to improve the surface finish. The experiments were carried out on electroplated pure nickel samples at first to characterize the fundamental limit of laser polishing on nickel. Then, Ni/Al_2O_3 (4.4 vol. %) nanocomposite samples were laser melted with the same parameters. Topography and microstructure characterizations were finally performed to study the effects of nanoparticles on the process.

6.1 EXPERIMENTAL METHOD

6.1.1 Laser Melting

The experimental setup of laser melting is schematically shown in Figure 6-1. A 1070 nm, 200 W fiber laser (SPI Lasers SP-200C-A-S6-A-C) was used for laser melting experiments. The laser was directed into a scan head (ScanLab HurryScan III 14 mm) to allow for a high-speed scan at a beam velocity of up to 2.0 m/s. The scan head was controlled by a PCI control card and furnished with an f-theta objective with a focal length of 163 mm. The laser was pulsed at 100 kHz with a pulse duration of 1.5 μs. The laser beam diameter was set at about 30 μm. Area polishing was achieved by a raster scan with a line spacing of 4 μm and a scan speed of 0.4 m/s. Argon flow was applied during laser polishing to minimize sample surface oxidation. Both pure Ni and Ni/Al_2O_3 nanocomposite (4.4 vol. %) were laser polished to investigate the effects of Al_2O_3

nanoparticles on polishability of Ni. Laser polishing experiments were conducted at different energies with other parameters fixed to seek for the optimal polishing parameter for each sample.

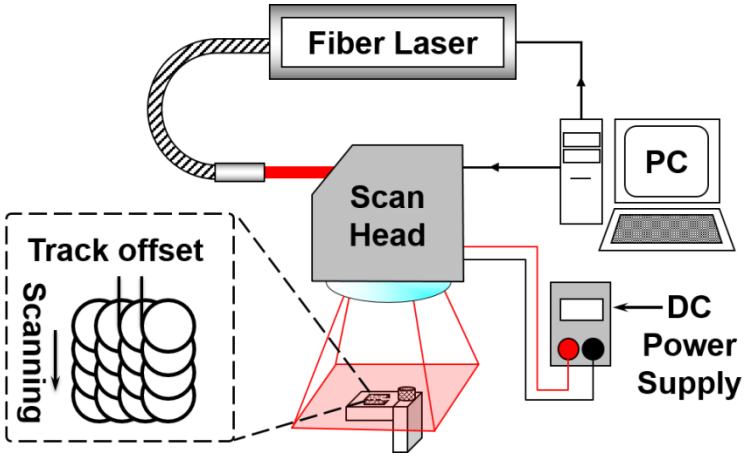

Figure 6-1 Experimental setup for laser melting

6.1.2 Characterization

The surface topographies of pure Ni and Ni/Al_2O_3 nanocomposite before and after laser melting were inspected with a white light interferometer. The metric for evaluating the polishing effectiveness was the arithmetic average roughness (Sa) based on area measurement, which was calculated according to the ASME standard [ASME 2009]. Areal surface roughness (e.g., Sa) is preferable to linear surface roughness (e.g., Ra) because it characterizes the surface topography over an entire area. Five measurements were made at different locations for each sample and the average value was taken to diminish the location variation effect.

Micro/nano-structures of samples were characterized using scanning electron microscopy (SEM) with energy dispersive X-ray spectroscopy (EDS/EDX). The EDS analysis was used to determine the fraction of Al_2O_3 nanoparticles incorporated in the Ni matrix. To characterize the

cross section of the laser processed region, a focused ion beam (FIB) system was used to cut the sample for in-situ SEM and FIB characterizations.

6.2 SURFACE TOPOGRAPHY

Laser melting experiments with various pulse energies were carried out on Ni and Ni/Al_2O_3 samples. The effects of nanoparticles on melt pool flows can be directly revealed by the specific surface topographies of Ni and Ni/Al_2O_3 after laser melting. Figure 6-2 shows the representative surface topographies of Ni and Ni/Al_2O_3 samples before laser melting, with the surface height data (Z) represented by different colors in reference to the X-direction and Y-direction. The Ni/Al_2O_3 nanocomposite is rougher than the pure Ni although they were deposited under the same condition. The average surface roughness of Ni over five locations is 254 nm while that of Ni/Al_2O_3 is 323 nm. The difference is probably due to the distortion of the electrical field in electrodeposition by the addition of Al_2O_3 nanoparticles.

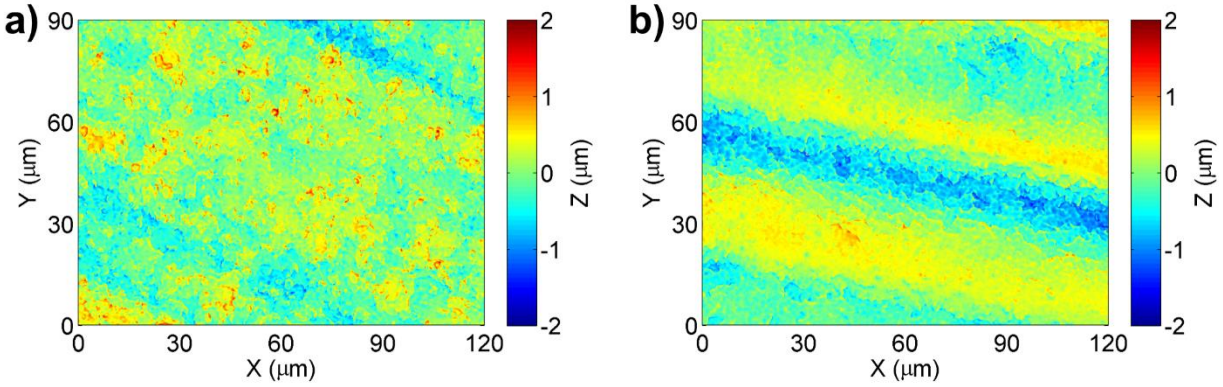

Figure 6-2 Surface topographies of (a) pure Ni and (b) Ni/Al_2O_3 before laser melting

Figure 6-3 shows the typical surface topographies of Ni and Ni/Al_2O_3 samples that were laser melted at the lowest pulse energy used in this study (0.10 mJ). The melt pool of the Ni/Al_2O_3

nanocomposite was more significantly melted than the pure Ni. The Ni/Al_2O_3 nanocomposite has a lower thermal conductivity than pure Ni and thus can accumulates more heat near the surface, which increases the melt duration so that the capillary waves damp down more for a smoother surface. In addition, the presence of nanoparticles increases the viscosity of the molten metal, which also results in more damping of capillary waves for further smoothening of surface asperities. In short, the more significant smoothening on Ni/Al_2O_3 than on Ni should be attributed to the nanoparticles-enabled reduction of thermal conductivity and enhancement of viscosity.

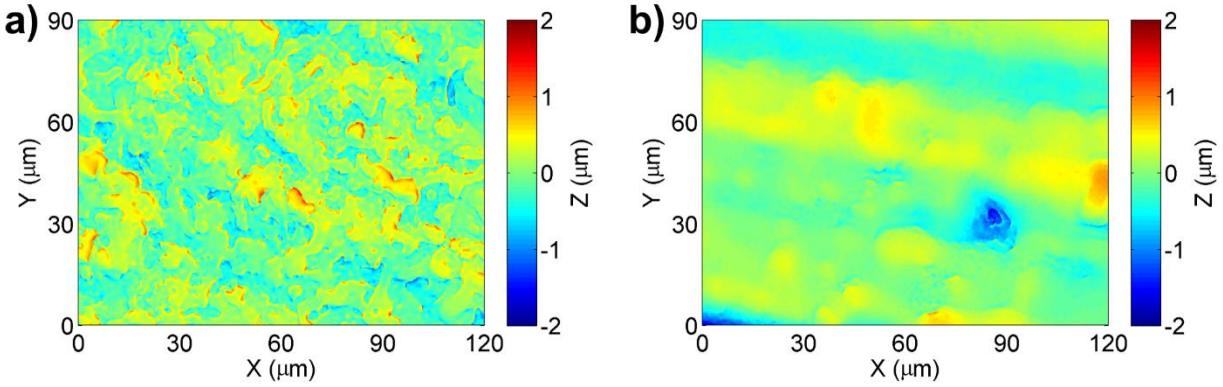

Figure 6-3 Surface topographies of (a) pure Ni and (b) Ni/Al_2O_3 laser melted at 0.10 mJ per pulse

Figure 6-4 shows the surface topographies of Ni and Ni/Al_2O_3 melted at a higher energy (0.14 mJ). As compared with those in Figure 6-3, the surface asperities were more significantly reduced because the increased energy results in a longer melt duration for surface wave damping. After melted under the same condition, the Ni/Al_2O_3 sample has smaller average surface roughness than the pure Ni sample. Although the laser melted surfaces in Figure 6-4 were much smoother than the original surfaces in Figure 6-2, some low-frequency asperities still remained.

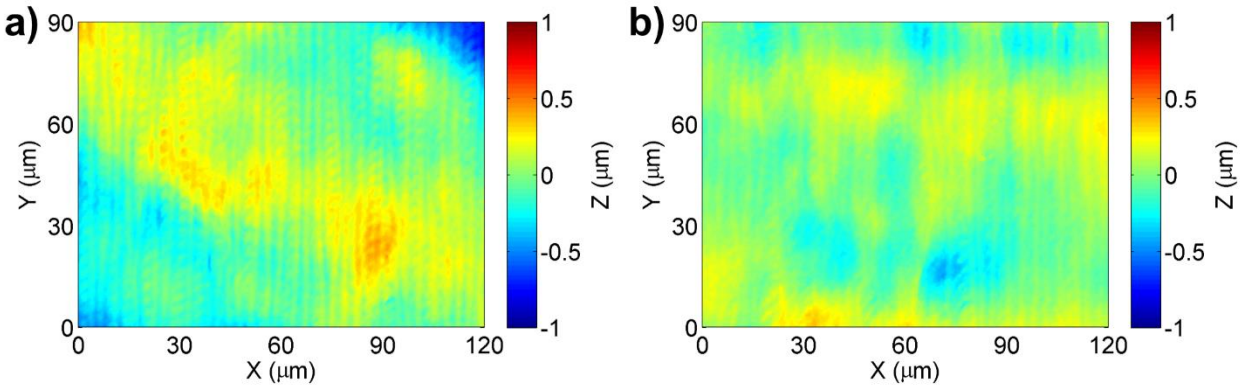

Figure 6-4 Surface topographies of (a) pure Ni and (b) Ni/Al_2O_3 laser polished at 0.14 mJ per pulse

The surface topographies of Ni and Ni/Al_2O_3 samples polished at an even higher energy (0.18 mJ) are shown in Figure 6-5. The increased energies induced more significant melting such that the low-frequency asperities are considerably reduced. However, the smoothening mechanisms for Ni and Ni/Al_2O_3 samples are different: thermocapillary regime for the Ni sample but capillary regime for the Ni/Al_2O_3 sample. Noticeably, by a comparison between Figures 6-5a and 6-5b, laser melting introduced more significant ripples in pure Ni than in Ni/Al_2O_3 by thermocapillary flows in the melt pools. To realize the thermocapillary flow, the surface tension gradient along the radial direction of the melt pool has to overcome the viscous force of the molten metal. Since Al_2O_3 nanoparticles increased the viscosity, it was more difficult to form thermocapillary flow in the melt pool of Ni/Al_2O_3 than that of Ni. Thus the addition of Al_2O_3 nanoparticles hindered the onset of thermocapillary flow and enlarged the processing window of capillary regime. This is of great significance in laser polishing. The extended capillary regime smoothens the surface more at almost no extra cost while the thermocapillary regime introduces artificial ripples/asperities in addition to smoothening.

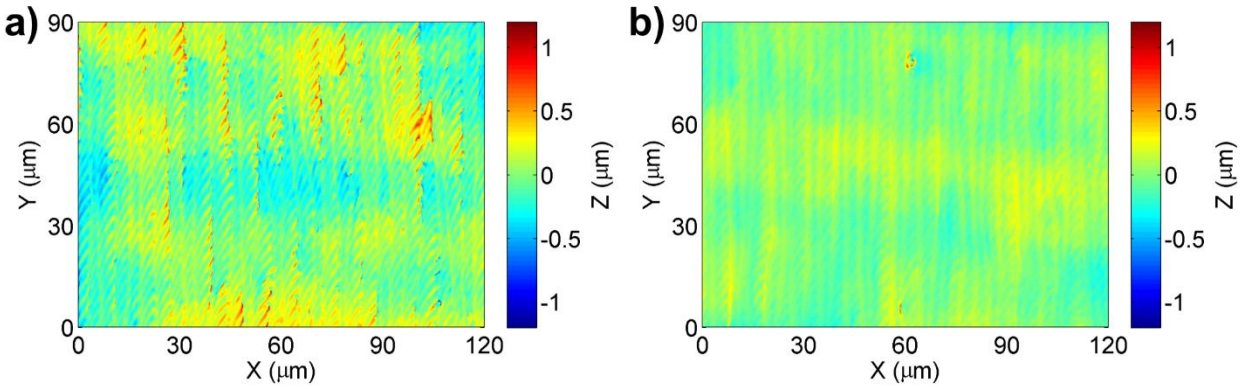

Figure 6-5 Surface topographies of (a) pure Ni and (b) Ni/Al_2O_3 laser polished at 0.18 mJ per pulse

As the laser pulse energy was further increased, the surface roughness of Ni decreased while that of Ni/Al_2O_3 increased, as shown in Figure 6-6. By a comparison between Figures 6-5a and 6-6a, the Ni surface was smoothened with the higher laser energy since the low-frequency asperities were reduced more significantly by a stronger thermocapillary flow. The pulse energy of 0.22 mJ was the optimal parameter for the pure Ni sample because a further increase in the pulse energy would induce a rougher surface due to the excessive ripples introduced by thermocapillary flows. In the case of Ni/Al_2O_3, as the pulse energy was increased from 0.18 mJ to 0.22 mJ, it triggered the onset of thermocapillary flows. The thermocapillary flow at 0.22 mJ played a role in roughening instead of smoothening since the Ni/Al_2O_3 surface was already smooth at 0.18 mJ.

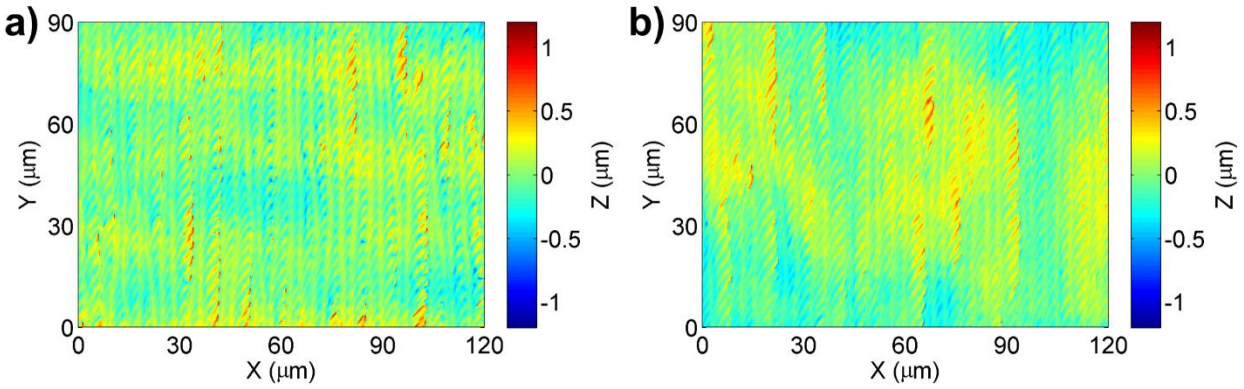

Figure 6-6 Surface topographies of (a) pure Ni and (b) Ni/Al_2O_3 laser polished at 0.22 mJ per pulse

6.3 SURFACE ROUGHNESS

Surface roughnesses were determined based on the measured topographies Ni and Ni/Al_2O_3 samples laser processed at various fluences. For a fair comparison, the roughnesses were further normalized by the original surface roughness of each material before laser melting. A normalized roughness value of less than 1 indicates that the laser melted surface is smoother than the original surface. Figure 6-7 shows the normalized surface roughnesses of Ni and Ni/Al_2O_3 as functions of laser energy. The surface roughness curves of Ni and Ni/Al_2O_3 follow a similar trend with increasing pulse energy. At the capillary regime at low laser energies, the melt duration increases and the surface becomes smoother as the energy increases. While at the thermocapillary regime at high laser energies, thermocapillary flows not only smoothens a surface by radial melt pool flow but also roughens the surface by the induced ripples.

The minimum values mean the best polishing results. The least normalized roughness achieved on Ni and Ni/Al_2O_3 is 0.42 and 0.22, respectively. The addition of Al_2O_3 nanoparticles in laser melting process reduced the normalized roughness nearly by a factor of two due to the

fluid dynamics tuning in the melt pool by nanoparticles. In terms of absolute roughness, with the optimal processing parameters, the surface roughness of Ni and Ni/Al_2O_3 was reduced from 254 nm to 107 nm and from 323 nm to 72 nm, respectively. The key results on laser melting of Ni and Ni/Al_2O_3 samples are listed in Table 6-1.

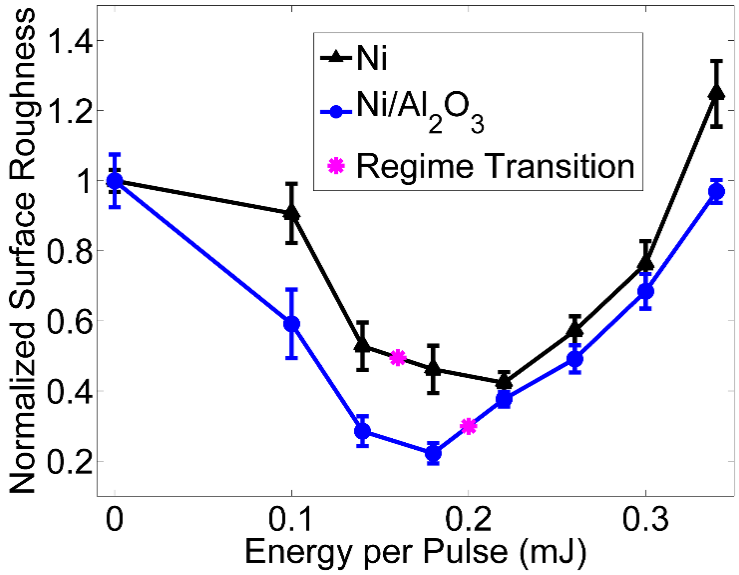

Figure 6-7 Normalized surface roughness of pure Ni and Ni/Al_2O_3 as a function of laser pulse energy

Table 6-1 Key results on laser polishing of Ni and Ni/Al_2O_3

Material	Original roughness (nm)	Pulse energy (mJ)	Melting regime	Achievable roughness (nm)	Normalized roughness
Ni	254	0.22	Thermocapillary	107	0.42
Ni/Al_2O_3	323	0.18	Capillary	72	0.22

Figures 6-8 and 6-9 show the spatial frequency spectra of the Ni and Ni/Al_2O_3 surfaces at various laser pulse energies. The spatial frequency spectra are cross sections of two-dimensional fast Fourier transforms (FFTs) of the surface height data from the topographic data. The X-

direction is perpendicular to the raster scan lines while the Y-direction is parallel to the scan tracks. The spectra at different laser pulse energies are presented with an offset to allow for better visibility.

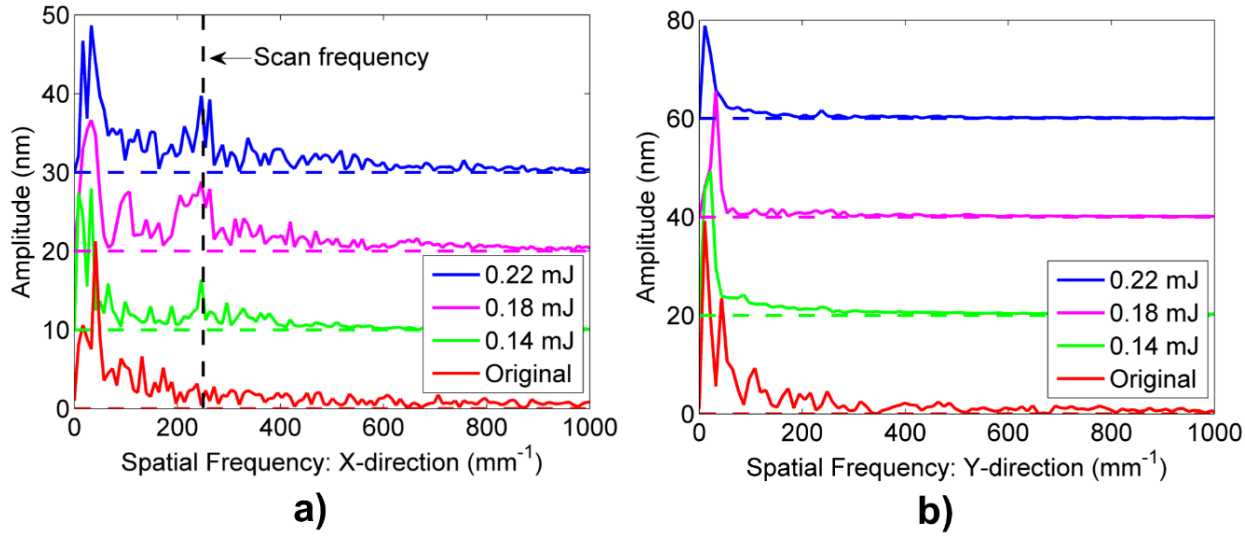

Figure 6-8 Spatial frequency spectra of Ni surface before and after laser melting at various pulse energies: (a) X-direction and (b) Y-direction

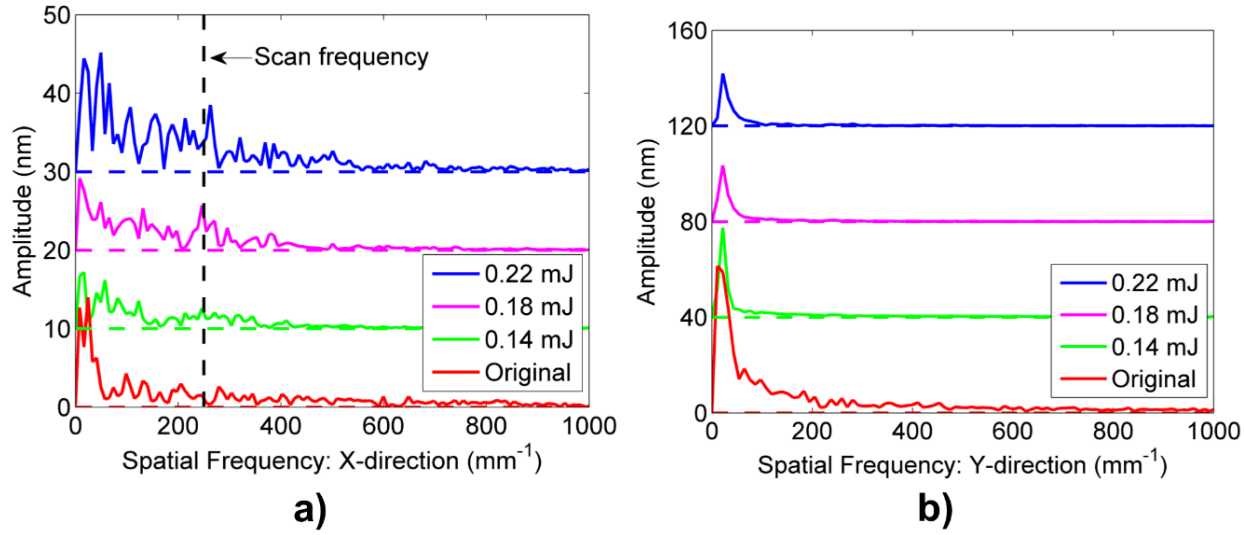

Figure 6-9 Spatial frequency spectra of Ni/Al_2O_3 surface before and after laser melting at various pulse energies: (a) X-direction and (b) Y-direction

For the surface roughnesses of the original surfaces of Ni and Ni/Al_2O_3, the asperities from the Y-direction spectra (Figures 6-8b and 6-9b) contribute most. As the laser pulse energy increases, the original asperities are reduced in the Y-direction spectra, but artificial features appear in the X-direction spectra, especially at the high laser pulse energies (e.g., 0.22 mJ). There exist optimal processing parameters to reach the minima in Figure 6-7.

The resultant surface topography by laser melting is dictated by the melt pool flow. Viscosity plays a crucial role in both the capillary and thermocapillary regimes. Since the introduction of nanoparticles increases the viscosity of the liquid metal, the melt pool dynamics can be controlled by nanoparticles. In this study, the nanoparticles enhance viscous damping in the capillary regime, resulting in a smoother surface on Ni/Al_2O_3 than on Ni, as shown in Figure 6-7. In addition, the nanoparticles suppress thermocapillary flows by increasing viscosity and thus enlarge the processing window of the capillary regime, which is clearly illustrated by the analysis of the spatial frequency spectra in Figures 6-8 and 6-9. The transition laser pulse energy between the capillary and thermocapillary regimes of Ni and Ni/Al_2O_3 can be determined by examining the characteristic asperities introduced by thermocapillary flows. If thermocapillary flows appear, a peak would be introduced to the spatial frequency spectra at the frequency associated with the scan line spacing. The offset between scan lines in the laser melting experiments was 4 μm, which is corresponding to a spatial frequency of 250 mm^{-1} as marked as black dashed lines in Figures 6-8a and 6-9a. The peaks at this certain spatial frequency can be considered as the signature of the thermocapillary flows. The frequency could be slightly off due to possible positioning errors of the scan head and measurement errors by the white light interferometer. In Figure 6-8a for the case of Ni, the peak is not visible at the laser pulse energy of 0.10 mJ, but initiated at 0.14 mJ and fully developed at 0.18 mJ and higher laser pulse energies. In Figure 6-9a for the case of Ni/Al_2O_3, the

peak is initiated only at the laser pulse energy of 0.18 mJ and fully developed at 0.22 mJ. Therefore, the transition energy between two regimes was defined as 0.14~0.18 mJ in Ni while 0.18~0.22 mJ in Ni/Al_2O_3. This provides a solid evidence that the thermocapillary flow is suppressed by nanoparticles and therefore the processing window of the capillary regime is extended.

Due to the higher viscosity by adding nanoparticles, the best polishing on Ni/Al_2O_3 was achieved in the capillary regime, which smoothened the asperities of almost all frequencies and reduced the surface roughness significantly. On pure Ni, the capillary regime polishing is less effective since only the high frequency asperities are effectively smoothened. Thermocapillary flows would be needed to polish the low-frequency features on Ni, but artificial asperities (i.e. ripples) are introduced, thereby resulting in a higher surface roughness than Ni/Al_2O_3. The significant improvement in surface finish by Al_2O_3 nanoparticles suggests that it is effective to control fluid dynamics by nanoparticles and thus to break some existing limits of laser material processing.

6.4 MICROSTRUCTURE

Figure 6-10 shows scanning electron microscopy (SEM) micrographs of the surface on Ni/Al_2O_3 nanocomposite laser melted at the pulse energy of 0.18 mJ. The bright particles are the Al_2O_3 phases. As compared with the Ni/Al_2O_3 nanocomposite microstructure before laser melting, the amount of Al_2O_3 particles is decreased after laser melting. In the raster scan process, the laser scan speed and the track offset were set to obtain ~80% overlap in both directions (i.e., parallel and perpendicular to the scan tracks). Hence the sample was actually melted and solidified multiple times (~5 times in each direction, i.e., ~10 times in total). Due to the repetitive laser melting for

temperatures above 2000 °C, some of the Al_2O_3 nanoparticles might have decomposed into Al and O atoms and dissolved in the molten Ni. The dissolved Al probably partially evaporated while the remaining Al could re-precipitate as Al_2O_3. It is also possible that some Al_2O_3 nanoparticles agglomerated and ejected from the melt pool. It is of interests for a future study on how some Al_2O_3 nanoparticles vanish during laser melting. While partial Al_2O_3 nanoparticles disappeared, the remaining nanoparticles still played an important role in the enhancement of the viscosity of the melt.

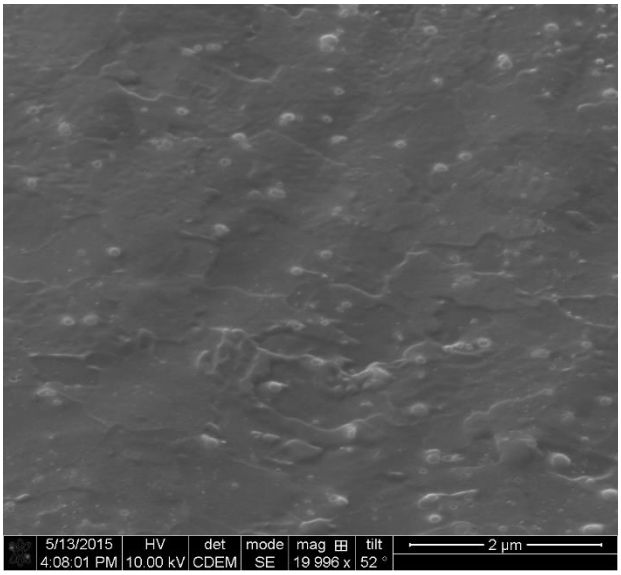

Figure 6-10 Surface of the laser melted Ni/Al_2O_3 nanocomposite

To characterize the cross section of the laser melted samples, the laser melted region was cut using focused ion beam (FIB). The SEM micrographs of the cross section of Ni and Ni/Al_2O_3 laser melted at the pulse energy of 0.18 mJ are shown in Figures 6-11 and 6-12, respectively.

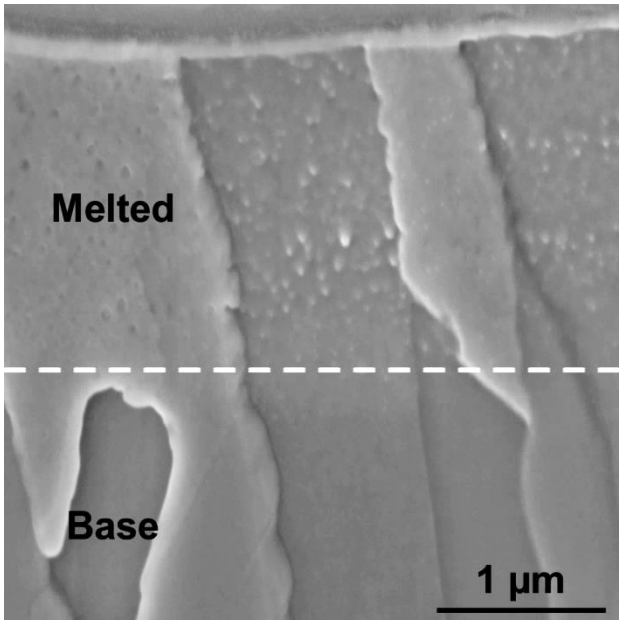

Figure 6-11 SEM micrograph of Ni cross section

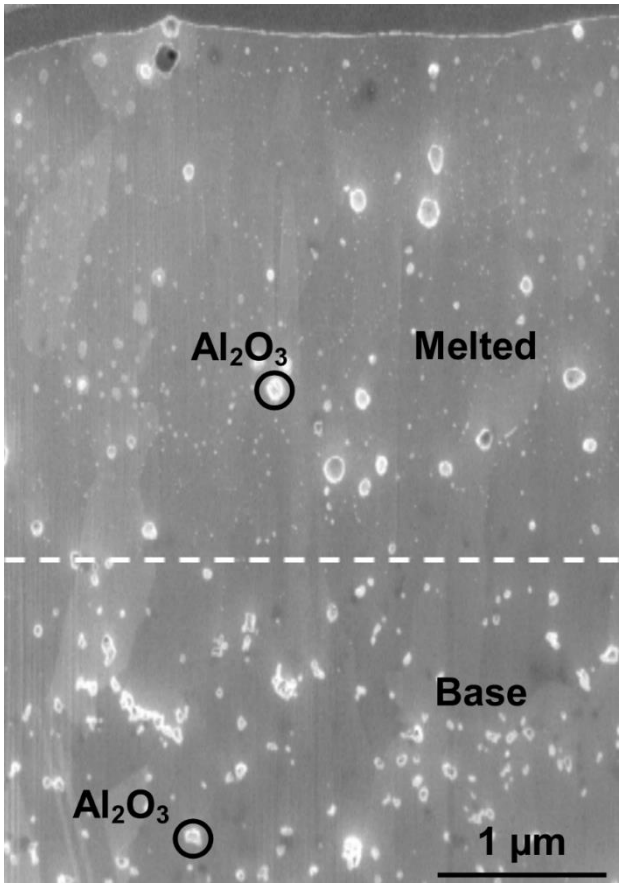

Figure 6-12 SEM micrograph of Ni/Al_2O_3 cross section

In both materials, the microstructure of the laser melted zone is different from the unmelted zone. The boundaries are marked by white dashed lines in the figures. It should be noted that the thin layer at the very top is a platinum coating deposited to protect the sample surface of interest during FIB cutting. In the pure Ni sample, there exist many tiny features induced by FIB process. In the Ni/Al_2O_3 nanocomposite sample, the amount of nanoparticles in the melted zone is less than in the unmelted zone.

It is quite interesting that the melt depth of the Ni/Al_2O_3 nanocomposite is much deeper than that of pure Ni. It could be attributed to two mechanisms: (a) the nanoparticles suppress the thermocapillary flows and thus diminish convective heat transfer within the melt pool and (b) the nanoparticles reduce the thermal conductivity and thus decrease the conductive heat transfer.

Further characterization by FIB imaging reveals surprising results. Ion beam can induce channeling contrast from different grains because the penetration depth of the ions is related to the crystallographic orientation of the grain, which makes FIB a powerful tool to characterize grain structures. Figures 6-13 shows an FIB micrograph of the Ni cross section. Three zones can be defined based on the distinguishable grain structures. The grains in the melted zone (MZ) and the heat affected zone (HAZ) are significantly larger than those in the unaffected region. It should be noted that the original sample prepared by electroplating is a nanocrystalline material. By inspection of the grain sizes, a boundary can be determined between the HAZ and the unaffected zone. A careful examination reveals that the grains on the top region (MZ) are actually tilted/distorted from those in the HAZ. The tilting/distorting of the grains in MZ is probably due to the asymmetric heating/cooling due to the raster scan of the laser. Similarly, the MZ and the HAZ of the Ni/Al_2O_3 can be determined as shown in Figure 6-14. The sizes of the MZs obtained

from the FIB images (Figures 6-13 and 6-14) agree well with those from the SEM graphs (Figures 6-11 and 6-12).

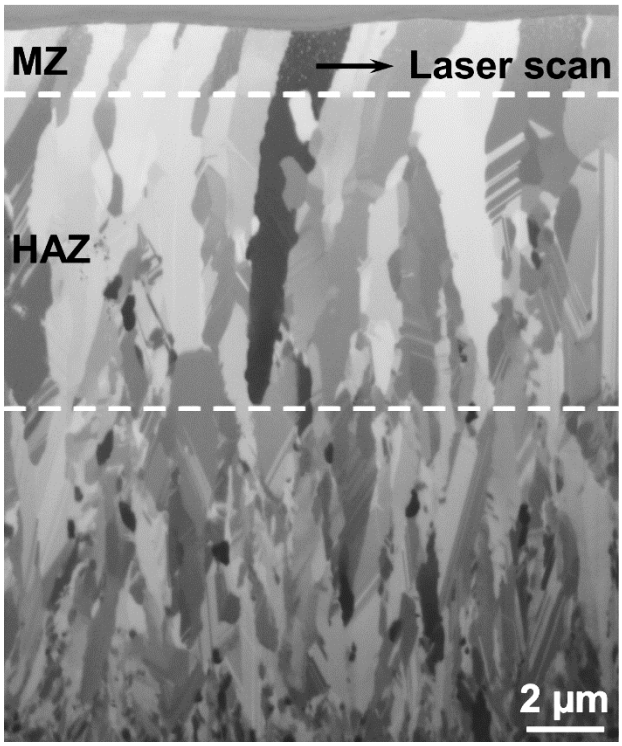

Figure 6-13 FIB micrograph of Ni cross section showing the melted zone (MZ) and the heat affected zone (HAZ)

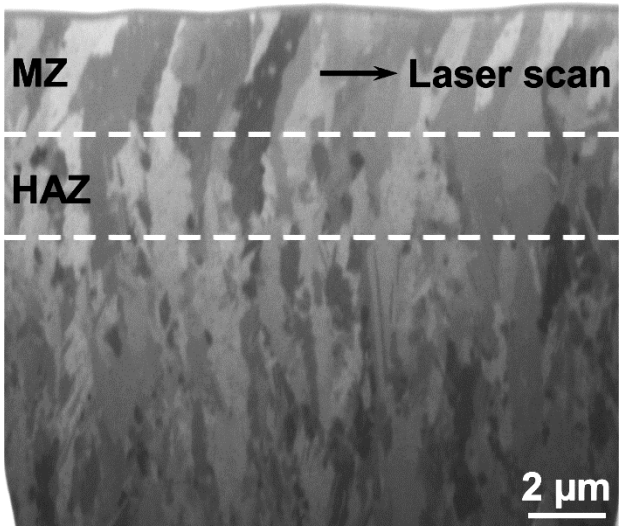

Figure 6-14 FIB micrograph of Ni/Al_2O_3 cross section showing the melted zone (MZ) and the heat affected zone (HAZ)

By a further study on the grain structures of laser melted Ni and Ni/Al_2O_3 in Figures 6-13 and 6-14, it is surprising to see that the HAZ size of the Ni/Al_2O_3 is remarkably smaller than that of Ni. It is believed that nanoparticles effectively inhibited the grain growth during laser heating and cooling. The nominal temperature of Ni for grain growth is only about 418 °C [Wang 2014] while that of Ni/Al_2O_3 is 800 °C which was determined by transmission electron microscopy (TEM) equipped with in-situ heating. Furthermore, the grains of Ni/Al_2O_3 grow more slowly than those of Ni because nanoparticles can restrict the grain growth by Zener pining effect.

It is of tremendous scientific and technical interests to increase the MZ while decrease the HAZ for numerous melting processes, such as laser welding and laser additive manufacturing, where the size of HAZ is a serious problem. It is of great potential to tune the sizes of MZ and HAZ by nanoparticles in other manufacturing processes for tremendous impacts.

6.5 NUMERICAL SIMULATION

To better understand why nanoparticles induced a larger melted zone (MZ) but a smaller heat affected zone (HAZ), numerical simulations were performed. A coupled heat transfer and fluid flow model, developed and validated for laser melting of metals in previous study [Ma 2013], was modified by inserting the newly measured effective optical and thermophysical properties as input parameters to account for the effects of nanoparticles.

In the model, the transient temperature field can be predicted as a function of time and location, and therefore the evolution of the MZ and the HAZ can be calculated. The prediction results in the cross section of Ni and Ni/Al_2O_3 samples are shown in Figure 6-15. Key data for MZ and HAZ for both Ni and Ni/Al_2O_3 samples is listed Table 6-2. Although the predicted sizes of the

MZ and the HAZ do not exactly match with the experimental results for the Ni/Al_2O_3 sample, the conclusion is clear: the MZ is increased while the HAZ is decreased by the nanoparticles. The numerical model successfully captures the effect of heat transfer and flow fluid on the microstructure development when the effect of nanoparticles on optical and thermophysical properties is considered. The small mismatch is probably due to the fact that the exact temperature-dependent properties of the nanocomposite are not available for the simulation and the Zener pinning effect is not considered in the model.

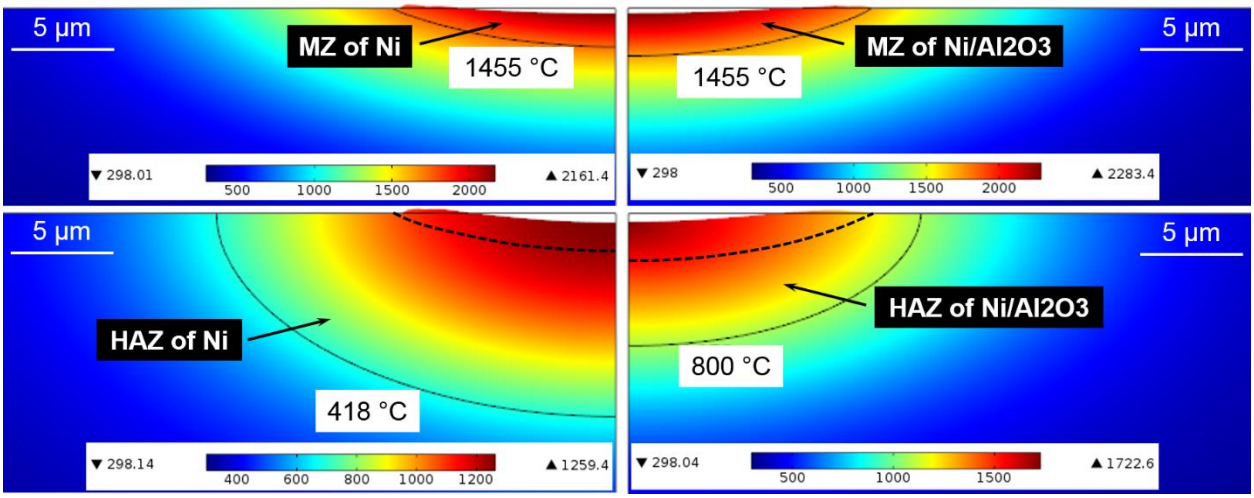

Figure 6-15 Simulated melted zone (MZ) and heat affected zone (HAZ) of Ni and Ni/Al_2O_3

Table 6-2 Key results on laser polishing of Ni and Ni/Al_2O_3

Sample	Melted zone size (μm)		Heat affected zone size (μm)		Grain growth temperature (°C)
	Measured	Predicted	Measured	Predicted	
Ni	1.9	1.8	8.3	8.1	418
Ni/Al_2O_3	3.1	2.3	2.7	4.1	800

Moreover, the numerical simulation is insightful to understand the mechanisms responsible for the evolution of distinguished microstructures. Firstly, from the simulation, the maximum

surface temperature of Ni/Al_2O_3 is higher than that of Ni, validating the hypothesis that the nanoparticles facilitate the heat accumulation more near the surface. In addition, the predicted maximum fluid velocity is reduced by a factor of two with the presence of nanoparticles, indicating that the nanoparticles suppress thermocapillary flows.

6.6 SUMMARY

The control of heat transfer and fluid flow by nanoparticles was successfully demonstrated using laser polishing as an example. The fundamental limit in laser polishing was overcome by tuning the melt pool dynamics via nanoparticles. With nanoparticles modifying the thermophysical properties, the onset of thermocapillary flows was shifted to allow a wider processing window for the capillary regime. In addition, the smoothening efficiency in capillary regime was enhanced because of the increased viscosity by nanoparticles. As a consequence of both effects, capillary regime was already powerful enough to smoothen the asperities on the Ni/Al_2O_3 nanocomposites to achieve a normalized surface roughness of 0.22, much lower than the minimum value achieved in pure Ni, i.e., 0.42. The microstructural and numerical studies showed the nanoparticles diminished the heat dissipation for a deeper melted zone (MZ). The nanoparticles also restricted the grain coarsening for a much smaller heat affected zone (HAZ). The control of microstructures by nanoparticles will bring tremendous impact if this new phenomenon can be extended to other materials processing technologies. Through thermophysical property tuning by nanoparticles, it opens another pathway to optimize a manufacturing process and adds another degree of freedom to broaden its capability and application space.

CHAPTER 7. CONCLUSIONS

The study is motivated by the rapidly growing interests in the development of metal matrix nanocomposites (MMNCs) and the lack of fundamental knowledge of how laser interacts with MMNCs. The research is also inspired by an intriguing hypothesis that the introduction of nanoparticles could break fundamental limits of laser melting processes. The specific research objective is to investigate the specific effects of nanoparticles on optical and thermophysical properties, heat transfer and fluid flow processes, and eventually on surface property and microstructure produced by laser melting.

Ultrasonic assisted electrocodeposition was used to prepare MMNCs samples in this study. Various nanoparticles were used for electrocodeposition experiments, including Al_2O_3 (50 nm) SiC (45–55 nm), ZrO_2 (40 nm), and Y_2O_3 (30–45 nm). The Al_2O_3 nanoparticles resulted in the best outcomes in terms of dispersion and incorporation. The Al_2O_3 nanoparticles were uniformly distributed and dispersed across the entire sample. Vickers hardness tests showed that the Ni/Al_2O_3 (4.4 vol. %) was 73.6 % harder than the pure Ni.

Experimental and theoretical studies were carried out to investigate the effects of nanoparticles on the optical and thermophysical properties of MMNCs, including reflectivity, surface tension, viscosity, heat capacity, and thermal conductivity. Firstly, using a power meter, the reflectivity of Ni/Al_2O_3 (1.8 vol. %) was measured to be 65.8 % while pure Ni was at 67.4%. %. It is probably due to the fact that Al_2O_3 is transparent at the wavelength of 1070 nm and the fraction of Al_2O_3 in the nanocomposite is not high. In order to determine the surface tension and viscosity of MMNCs, an innovative measurement system was developed based on the accessible laser

system, inspired by the so-called oscillating drop method. The surface tensions of Ni/Al_2O_3 (4.4 vol. %) and Ni/SiC (3.6 vol. %) at ~1500 °C were 1.39 ± 0.03 N/m and 1.57 ± 0.06 N/m, respectively, slightly lower than that of pure Ni, 1.68 ± 0.04 N/m. The viscosities of these Ni/Al_2O_3 and Ni/SiC MMNCs at ~1500 °C were 13.3 ± 0.8 mPa·s and 17.3 ± 3.1 mPa·s, respectively, significantly higher than that of pure Ni, 4.8 ± 0.3 mPa·s. Differential scanning calorimetry was used to determine the heat capacity of the same MMNCs. The specific heat capacities of the Ni/Al_2O_3 and Ni/SiC at room temperature were 424 ± 13 J/(kg·K) and 423 ± 14 J/(kg·K), respectively, not substantially different from that of pure Ni, 424 ± 8 J/(kg·K). The insignificant difference in heat capacity between the nanocomposites and the base nickel agrees well with the theoretical perditions. It is likely that the fraction of nanoparticles is not high enough, or the size of nanoparticle not small enough, to considerably change the effective heat capacity. An experimental setup was developed to measure thermal conductivity based on the laser flash method. The thermal conductivities of these Ni/Al_2O_3 and Ni/SiC MMNCs at room temperature were 84.1 ± 3.4 W/(m·K) and 87.3 ± 3.4 W/(m·K), respectively, slightly less than that of pure Ni, 91.7 ± 2.8 W/(m·K). The reduction in the thermal conductivity can be attributed to that the nanoparticles introduce interfacial resistance and energy carriers scattering. A theoretical model was introduced to predict the thermal conductivity of MMNCs based on the effective medium approximation theory. The prediction results match well with the measurements. The optical and thermophysical properties of MMNCs had not been determined before this work. The developed experimental and theoretical approaches enable an open access to these properties for the first time, and could be applied to other MMNCs as well.

To study how these nanoparticles-modified properties affect laser melting process, especially the melt pool dynamics, an analytical heat transfer and fluid flow model was developed

to predict the temperature field and thermocapillary flows in the melt pool. The model was applied to Ni/Al_2O_3 nanocomposites of different nanoparticle fractions and pure Ni as a reference. The analytical results showed that thermocapillary flows were greatly suppressed by the addition of nanoparticles mainly because of the viscosity enhancement by nanoparticles, and therefore the corresponding surface asperities were reduced. The predictions agree well with the experimental measurements using white-light interferometer. This study suggested the laser melting of Ni/Al_2O_3 (4.4 vol. %) resulted in the best surface finish.

Systematic laser polishing experiments at various laser pulse energies were conducted on Ni/Al_2O_3 (4.4 vol. %) and pure Ni for comparison. The experimental results showed that the nanoparticles-enabled suppression of thermocapillary flows extended the processing window of the capillary regime for significantly improved surface smoothening. In addition, the viscosity enhancement by the nanoparticles also increased the effectiveness of laser polishing in the capillary regime because of an enhanced viscous damping of the capillary oscillations. The surface roughness of the Ni/Al_2O_3 was reduced from 323 nm to 72 nm with the optimal laser polishing parameters while that of pure Ni only from 254 nm to 107 nm. The normalized surface roughness was decreased by nearly a factor of two with the help of nanoparticles. The nanoparticles were capable of effective control of melt pool dynamics to break the fundamental limit of laser polishing.

The microstructural study on the cross section of the laser processed region was highly interesting. By the addition of the 4.4 vol. % Al_2O_3 nanoparticles, the laser melted zone (MZ) depth was increased from 1.9 μm to 3.1 μm while the heat affected zone (HAZ) size was significantly reduced from 8.3 μm to 2.7 μm, surprisingly. To further understand these remarkable changes in microstructures, numerical simulations of laser melting were performed using the

newly measured optical and thermophysical properties. It suggests that the nanoparticles inhibit the heat transfer and thus enhance heat accumulation within the surface layer to reduce the MZ depth. The nanoparticles also restrict the grain growth and thus raise the grain growth temperature to shrink HAZ. It is of great potential to tune the sizes of MZ and HAZ by nanoparticles in other manufacturing processes for tremendous impacts.

In summary, the work in this dissertation has established systematic theoretical and experimental methodologies to study laser melting of MMNCs. The study has significantly advanced the fundamental knowledge on how laser interacts with MMNCs. Under the guidance of the fundamental knowledge, some existing limits of laser melting have been successfully overcome, which will broaden its processing capability and application space.

CHAPTER 8. RECOMMENDATIONS FOR FUTURE WORK

The work presented in this dissertation is a major step forward in the fundamental understanding and development of laser processing of metal matrix nanocomposites (MMNCs). Many facets of the process have been explored, and it suggests that nanoparticles can be an effective way to tailor the thermophysical properties and thus the outcomes of laser processing. To further understand the laser interaction with MMNCs and tremendously expand its application space, future research is needed.

8.1 MEASUREMENTS OF TEMPERATURE-DEPENDENT PROPERTIES

The study on the effects of nanoparticles on the optical and thermophysical properties is one of the key contributions of this work. However, the measurements of the properties were mainly carried out at a single temperature (or the temperature might not have been accurately determined). It would be more interesting to obtain temperature-dependent properties by extending the measurement techniques developed in this research. If successful, it would allow for a better understanding of the process physics and a more accurate analytical or numerical modeling of the process.

8.2 FURTHER STUDY ON THE MECHANISM OF NANOPARTICLE VANISHING

In the microstructural study on the laser processed region of the MMNCs, it was evident that some nanoparticles vanished after laser melting. The exact mechanism still remains unclear. It is important to investigate why the nanoparticles vanish during laser melting. The knowledge

will be crucial for precise control of the nanoparticle effect on the process. Experimentations with different nanoparticles and base materials at various laser energy levels can be carried out and then the resultant microstructures can be analyzed to reveal the underlying mechanism of nanoparticle vanishing. The relationship among process parameters, behaviors of the nanoparticles, microstructure evolution, and material properties can be established.

8.3 CHARACTERIZATION OF MECHANICAL PROPERTIES

Multi-scale mechanical properties are of significance for future study, especially to understand the property differences among melted zone, heat affected zone, and unprocessed zone. Nanoindenter can be used to precisely study the spatial distribution of mechanical properties at micro- and nano-scales. The mechanical behavior of the laser processed region can also be characterized by so-called “Picoindenter”, which is an advanced micro/nano-mechanical testing system and capable of compression tests on pillars with diameters from 70 nm to 5 μm. Moreover, SEM and TEM characterizations can be conducted in-situ to observe the testing process. Yield strength, plastic strain, Young’s modulus, and microstructure evolution during deformation can be obtained. The test results will be essential to understand the relationships among processing, microstructures and properties.

8.4 EXTENTION TO VARIOUS MANUFACTURING PROCESSES

The nanoparticle approach is successfully demonstrated as an effective way to tune the thermophysical properties for laser melting. It is highly promising that this methodology would be readily extended to other manufacturing processes to control the sizes of melt depth and heat

affected zone, refine microstructures, and improve material performance. It has great potential as a transformative manufacturing approach if the knowledge can be successfully transferred to other processes such as laser welding and laser additive manufacturing.

REFERENCES

- [Abramovitz 1970] Abramovitz, M., and Stegun, I.A., 1970, *Handbook of Mathematical Functions*, Dover, New York, US.

- [Arsenault 1991] Arsenault, R.J., Wang, L. and Feng, C.R., 1991, "Strengthening of Composites due to Microstructural Changes in the Matrix," *Acta Metallurgica et Materialia*, Vol. 39(1), pp. 47–57.

- [ASME 2009] American Society of Mechanical Engineers (ASME), 2009, *Surface Texture: Surface Roughness, Waviness, and Lay*, ASME B46.1-2009 (Revision of ASME B46.1-2002).

- [Audebert 2002] Audebert, F., Prima, F., Galano, M., Tomut, M., Warren, P.J., Stone, I.C. and Cantor, B., 2002, "Structural Characterisation and Mechanical Properties of Nanocomposite Al-based Alloys," *Materials Transactions*, Vol. 43(8), pp. 2017–2025.

- [Bereznai 2003] Bereznai, M., Pelsöczi, I., Tóth, Z., Turzó, K., Radnai, M., Bor, Z., and Fazekas, A., 2003, "Surface Modifications Induced by ns and Sub-ps Excimer Laser Pulses on Titanium Implant Material," *Biomaterials*, Vol. 24, pp. 4197–4203.

- [Biedunkiewicz 2011] Biedunkiewicz, A., Biedunkiewicz, W., Figiel, P., and Grzesiak, D., 2011, "Preparation of Stainless Steel-TiC Composite by Selective Laser Melting," *Chemicke Listy*, Vol. 105, pp. 773–774.

- [Biedunkiewicz 2013] Biedunkiewicz, A., Biedunkiewicz, W., Figiel, P., Gabriel-Polrolniczak, U., Grzesiak, D., and Krawczyk, M., 2013, "Effect of Milling Time on

Thermal Treatment of TiC, TiB_2/steel Powders," *Journal of Thermal Analysis and Calorimetry*, Vol. 113, pp. 379–383.

- [Bindiya 2012] Bindiya, S., Basavanna, S., and Naik, Y.A., 2012, "Electrodeposition and Corrosion Properties of Zn-V_2O_5 Composite Coatings," *Journal of Materials Engineering and Performance*, Vol. 21, pp. 1879–1884.

- [Biswas 2012] Biswas, K., He, J., Blum, I.D., Wu, C.I., Hogan, T.P., Seidman, D.N., Dravid, V.P., Kanatzidis, M.G., 2012, "High-performance Bulk Thermoelectrics with All-scale Hierarchical Architectures," *Nature*, Vol. 489, p. 415.

- [Bordatchev 2014] Bordatchev, E.V., Hafiz, A.M.K., and Tutunea-Fatan, O.R., 2014, "Performance of Laser Polishing in Finishing of Metallic Surfaces," *Journal of Advanced Manufacturing Technology*, Vol. 73, pp. 35–52.

- [Borkar 2011] Borkar, T, and Harimkar, S.P., 2011, "Effect of Electrodeposition Conditions and Reinforcement Content on Microstructure and Tribological Properties of Nickel Composite Coatings," *Surface & Coatings Technology*, Vol. 205, pp. 4124–4134.

- [Bund 2007] Bund, A., Thiemig, D., 2007, "Influence of Bath Composition and pH on the Electrocodeposition of Alumina Nanoparticles and Nickel," *Surface & Coatings Technology*, Vol. 201, pp. 7092–7099.

- [Cao 2008] Cao, G., Konishi, H. and Li, X., 2008, "Mechanical Properties and Microstructure of Mg/SiC Nanocomposites Fabricated by Ultrasonic Cavitation Based Nanomanufacturing," *Journal of Manufacturing Science and Engineering*, Vol. 130, pp. 031105-1–031105-6.

- [Carlslaw 1988] Carlslaw, H.S., and Jaeger, J.C., 1988, *Conduction of Heat in Solids*, Clarendon, Oxford, UK.

- [Celis 1987] Celis, J.P., Ross, J.R., and Buelens, C., 1987, "A Mathematical Model for the Electrolytic Codeposition of Particles with a Metallic Matrix," *Journal of The Electrochemical Society*, Vol. 134, pp. 1402–1408.

- [Chandrappa 2012] Chandrappa, K.G., Venkatesha T.V., Nayana K.O., and Punithkumar M.K., 2012, "Generation of Nanocrystalline NiO Particles by Solution Combustion Method and its Zn-NiO Composite Coating for Corrosion Protection," *Materials and Corrosion*, Vol. 63, pp. 445–455.

- [Chase 1998] Chase Jr, M.W., 1998, "NIST-JANAF Thermochemical Tables," *Journal of Physical and Chemical Reference Data*, Monograph No. 9.

- [Chen 2005] Chen, H., Xu, C., Qu, J., Hutchings, I.M., Shipway, P.H., and Liu, J., 2005, "Sliding Wear Behaviour of Laser Clad Coatings Based upon a Nickel-based Self-fluxing Alloy Co-deposited with Conventional and Nanostructured Tungsten Carbide-cobalt Hardmetals," *Wear*, Vol. 259, pp. 801–805.

- [Chen 2006] Chen, L., Wang L., Zeng, Z., and Zhang, J., 2006, "Effect of Surfactant on the Electrodeposition and Wear resistance of Ni-Al_2O_3 Composite Coatings," *Materials Science and Engineering A*, Vol. 434, pp. 319–325.

- [Chen 2008a] Chen, H., Xu, C., Chen, J., Zhao, H., Zhang, L., and Wang, Z., 2008, "Microstructure and Phase Transformation of WC/Ni60B Laser Cladding Coatings during Dry Sliding Wear," *Wear*, Vol. 264, pp. 487–493.

- [Chen 2008b] Chen, C., Zhang, M., Chang, Q., Zhang, S., Ma, H., Yan, W., and Wang, M., 2008, "Laser Cladding of ZM5 Magnesium Base Alloy with Al+Nano-SiC Powder," *Lasers in Engineering*, Vol. 18, pp. 85–94.

- [Choudhury 2007] Choudhury R.A., Ezz, T., and Li, L., 2007, "Synthesis of Hard Nano-structured Metal Matrix Composite Boride Coatings Using Combined Laser and Sol-gel Technology," *Materials Science and Engineering A*, Vols. 445–446, pp. 193–202.

- [Choudhury 2008] Choudhury R.A., Ezz, T., Chatterjee, S., and Li, L., 2008, "Microstructure and Tribological Behaviour of Nano-structured Metal Matrix Composite Boride Coatings Synthesized by Combined Laser and Sol-gel Technology," *Surface & Coatings Technology*, Vol. 202, pp. 2817–2829.

- [Corcione 2011] Corcione, M., 2011, "Empirical Correlating Equations for Predicting the Effective Thermal Conductivity and Dynamic Viscosity of Nanofluids," *Energy Conversion and Management*, Vol. 52(1), pp. 789–793.

- [Crainic 2002] Crainic, N. and Marques, A.T., 2002, "Nanocomposites: a State-of-the-art Review," *Key Engineering Materials*, Vol. 230−232, pp. 656–659.

- [Dadbakhsh 2012] Dadbakhsh, S., and Hao, L., "Effect of Al Alloys on Selective Laser Melting Behaviour and Microstructure of in situ Formed Particle Reinforced Composites," *Journal of Alloys and Compounds*, Vol. 541, pp. 328–334.

- [Deguchi 2001] Deguchi, T., Imai, K., Matsui, H., Iwasaki, M., Tada, H., and Ito S., 2001, "Rapid Electroplating of Photocatalytically Highly Active TiO_2-Zn Nanocomposite Films on Steel," *Journal of Materials Science*, Vol. 36, pp. 4723–4729.

- [Faroughi 2015] Faroughi, S.A. and Huber, C., 2015, "Effective Thermal Conductivity of Metal and Non-metal Particulate Composites with Interfacial Thermal Resistance at High Volume Fraction of Nano to Macro-sized Spheres," *Journal of Applied Physics*, Vol. 117(5), pp. 055104-1–055104-8.

- [Feng 2007] Feng, Q., Li, T., Zhang, Z., Zhang, J., Liu, M., and Jin, J., 2007, "Preparation of Nanostructured Ni/Al_2O_3 Composite Coatings in High Magnetic Field," *Surface & Coatings Technology*, Vol. 201, pp. 6247–6252.

- [Figiel 2012] Figiel, P., Biedunkiewicz, and W., Grzesiak, D., 2012, "Oxidation Process of the Steel/nc-TiC Nanocomposites," *Journal of Thermal Analysis and Calorimetry*, Vol. 108, pp. 979–983.

- [Frade 2010] Frade, T., Bouzon, V., Gomes, A., and da Silva Pereira, M.I., 2010, "Pulsed-reverse Current Electrodeposition of Zn and Zn-TiO_2 Nanocomposite Films," *Surface & Coatings Technology*, Vol. 204, pp. 3592–3598.

- [Frade 2011] Frade, T., Gomes, A., da Silva Pereira, M.I., Alberts, D., Pereiro, R., and Fernández, B., 2011, "Studies on the Stability of Zn and Zn-TiO_2 Nanocomposite Coatings Prepared by Pulse Reverse Current," *Journal of The Electrochemical Society*, Vol. 158, pp. C63–C70.

- [Fransaer 1992] Fransaer, J., Celis, J.P., and Ross, J.R., 1992, "Analysis of the Electrolytic Codeposition of Non-Brownian Particles with Metals," *Journal of The Electrochemical Society*, Vol. 139, pp. 413–425.

- [Fusters 2008] Fustes, J., Gomes, A., and da Silva Pereira, M.I., 2008, "Electrodeposition of Zn-TiO_2 Nanocomposite Films-Effect of Bath Composition," *Journal of Solid State Electrochemistry*, (2008) Vol. 12, pp. 1435–1443.

- [Gallois 1981] Gallois, B., and Lupis, C.H.P., 1981, "Effect of Oxygen on the Surface Tension of Liquid Copper," *Metallurgical Transactions B*, Vol. 12B, pp. 549–557.

- [García-Lecina 2012] García-Lecina, E., García-Urrutia, I., Díez, J.A., Morgiel, J., and Indyka P., 2012, "A Comparative Study of the Effect of Mechanical and Ultrasound Agitation on the Properties of Electrodeposited Ni/Al_2O_3 Nanocomposite Coatings," *Surface & Coatings Technology*, Vol. 206, pp. 2998–3005.

- [Gomes 2005] Gomes, A., da Silva Pereira, M.I., Mendonca, M.H., and Costa, F.M., 2005, "Zn-TiO_2 Composite Films Prepared by Pulsed Electrodeposition," *Journal of Solid State Electrochemistry*, Vol. 9, pp. 190–196.

- [Gomes 2013] Gomes, A., Videira, A., Monteiro, O.C., Nunes, C.D., Carvalho, M.L., and Lopes, A.B., 2013, "Pulsed Current Electrodeposition of Zn-Ag_2S/TiO_2 Nanocomposite Films as Potential Photoelectrodes," *Journal of Solid State Electrochemistry*, Vol. 17, pp. 2349–2359.

- [Guglielmi 1972] Guglielmi, N., 1972, "Kinetics of the Deposition of Inert Particles from Electrolytic Baths," *Journal of The Electrochemical Society*, Vol. 119, pp. 1009–1012.

- [Gu 2009] Gu, D., Wang, Z., Shen, Y., Li, Q., and Li, Y., 2009, "In-situ TiC Particle Reinforced Ti-Al Matrix Composites: Powder Preparation by Mechanical Alloying and Selective Laser Melting behavior," *Applied Surface Science*, Vol. 255, pp. 9230–9240.

- [Gu 2010] Gu, D., Meiners, W., Hagedorn, Y., Wissenbach, K., and Poprawe, R., 2010, "Bulk-form TiC_X/Ti Nanocomposites with Controlled Nanostructure Prepared by a New Method: Selective Laser Melting," *Journal of Physics D: Applied Physics*, Vol. 43, pp. 295402-1–295402-7.

- [Gu 2011] Gu, D., Hagedorn, Y., Meiners, W., Wissenbach, K., and Poprawe, R., 2011, "Nanocrystalline TiC Reinforced Ti Matrix Bulk-form Nanocomposites by Selective Laser Melting (SLM): Densification, Growth Mechanism and Wear Behavior," *Composites Science and Technology*, Vol. 71, pp. 1612–1620.

- [Gu 2012] Gu, D., Meng, G., Li, C., Meiners, W., and Poprawe, R., 2012, "Selective Laser Melting of TiC/Ti Bulk Nanocomposites: Influence of Nanoscale Reinforcement," *Scripta Materialia*, Vol. 67, pp. 185–188.

- [Gu 2014] Gu, D., Wang, H., and Zhang, G., 2014, "Selective Laser Melting Additive Manufacturing of Ti-Based Nanocomposites: The Role of Nanopowder," *Metallurgical and Materials Transactions A*, Vol. 45, pp. 464–476.

- [Hafiz 2012] Hafiz, A.M.K., Bordatchev, E.V., Tutunea-Fatan, R.O., 2012, "Influence of Overlap between the Laser Beam Tracks on Surface Quality in Laser Polishing of AISI H13 Tool Steel," Journal of Manufacturing Processes, Vol. 14, pp. 425–434.

- [Heiple 1982] Heiple, C.R., and Roper, J.R., 1982, "Mechanism for Minor Element Effect on GTA Fusion Zone Geometry," *Welding Journal*, Vol. 61, pp. 97-s–102-s.

- [Hirosawa 2003] Hirosawa, S., Shigemoto, Y., Miyoshi, T. and Kanekiyo, H., 2003, "Direct Formation of $Fe_3B/Nd_2Fe_{14}B$ Nanocomposite Permanent Magnets in Rapid Solidification," *Scripta Materialia*, Vol. 48, pp. 839–844.

- [Islamgaliev 2001] Islamgaliev, R.K., Yunusova, N.F., Sabirov, I.N., Sergueeva, A.V. and Valiev, R.Z., 2001, "Deformation Behavior of Nanostructured Aluminum Alloy Processed by Severe Plastic Deformation," *Materials Science and Engineering A*, Vol. 319, pp. 877–881.

- [Ito 1999] Ito, S., Deguchi, T., Imai, K., Iwasaki, M., and Tada, H., 1999, "Preparation of Highly Photocatalytic Nanocomposite Films Consisting of TiO_2 Particles and Zn Electrodeposited on Steel," *Electrochemical and Solid-State Letters*, Vol. 2, pp. 440–442.

- [Jiang 2003] Jiang, Q.C., Li, X.L. and Wang, H.Y., 2003, "Fabrication of TiC Particulate Reinforced Magnesium Matrix Composites," *Scripta Materialia*, Vol. 48, pp. 713–717.

- [Kanagalasara 2012] Kanagalasara V., and Venkatesha, T.V., 2012, "Studies on Electrodeposition of Zn-MoS_2 Nanocomposite Coatings on Mild Steel and its Properties," *Journal of Solid State Electrochemistry*, Vol. 16, pp. 993–1001.

- [Khan 2011] Khan, T.R., Erbe, A., Auinger, M., Marlow, F., and Rohwerder, M., 2011, "Electrodeposition of Zinc-silica Composite Coatings: Challenges in Incorporating Functionalized Silica Particles into a Zinc Matrix," *Science and Technology of Advanced Materials*, Vol. 12, pp. 055005-1–055005-9.

- [Kim 2004] Kim, Y.G., Ryu, J.K., Kim, D.J., Kim, H.J., Lee, S., Cha, B.H., Cha, H., and Kim, C.J., 2004, "Microroughness Reduction of Tungsten Films by Laser Polishing

Technology with a Line Beam," *Japanese Journal of Applied Physics*, Vol. 43, pp. 1315–1322.

- [Kim 2006] Kim, S.J., Bang, I.C., Buongiorno, J., and Hu, L.W., 2006, "Effects of Nanoparticle Deposition on Surface Wettability Influencing Boiling Heat Transfer in Nanofluids," *Applied Physics Letters*, Vol. 89, p. 153107.

- [Kou 1985] Sindo, K., and Sun, D.K., 1985, "Fluid Flow and Weld Penetration in Stationary Arc Welds," *Metallurgical and Materials Transactions A*, Vol. 16, pp. 203–213.

- [Kruth 2005] Kruth, J-P., Mercelis, P., Van Vaerenbergh, J., Froyen, L., and Rombouts, M., 2005, "Binding Mechanisms in Selective Laser Sintering and Selective Laser Melting," *Rapid Prototyping Journal*, Vol. 11, pp. 26–36.

- [Kumar 2011] Kumar, M.K.P., Venkatesha, T.V., Pavithra, M.K., and Shetty, A.N., 2011, "The Fabrication, Characterization and Electrochemical Corrosion Behavior of Zn-TiO_2 Composite Coatings," *Physica Scripta*, Vol. 84, pp. 035601-1–035601-10.

- [Kumar 2012] Kumar, C.M.P., Venkatesha, T.V, and Chandrappa, K.G., 2012, "Effect of Surfactants on Co-deposition of B_4C Nanoparticles in Zn Matrix by Electrodeposition and its Corrosion Behavior," *Surface & Coatings Technology*, Vol. 206, pp. 2249–2257.

- [Kuo 2004] Kuo, S., Chen, Y., Ger, M., and Hwu, W., 2004, "Nano-particles Dispersion Effect on Ni/Al_2O_3 Composite Coatings," *Materials Chemistry and Physics*, Vol. 86, pp. 5–10.

- [Kwon 2012] Kwon, H., Baek, W., Kim, M., Shin, W., and Yoh, J., 2012, "Temperature-dependent Absorptance of Painted Aluminum, Stainless Steel 304, and Titanium for 1.07 mm and 10.6 mm Laser Beams," *Optics and Lasers in Engineering*, Vol. 50, pp. 114–121.

- [Lamikiz 2006] Lamikiz, A., Sánchez, J.A., López de Lacalle, L.N., del Pozo, D., and Etayo, J.M., 2006, "Surface Roughness Improvement Using Laser-Polishing Techniques," *Materials Science Forum*, Vol. 526, pp. 217–222.

- [Lamikiz 2007] Lamikiz, A., Sanchez, J.A., Lopez de Lacelle, L.N., del Pozo, D., Etayo, J.M., and López, J.M., 2007, "Laser Polishing Techniques for Roughness Improvement on Metallic Surfaces," *International Journal of Nanomanufacturing*, Vol. 1, pp. 490–498.

- [Landau 1959] Landau, L.D., and Lifshitz, E.M., 1959, *Fluid Mechanics*, Pergamon Press, Oxford, UK.

- [Li 1993] Li, H.H., 1993, "Refractive index of silicon and germanium and its wavelength and temperature derivatives," *Journal of Physical and Chemical Reference Data*, Vol. 9, pp. 561–658.

- [Li 2006] Li, M., He, Y., and Yuan, X., 2006, "Effect of Nano-Y_2O_3 on Microstructure of Laser Cladding Cobalt-based Alloy Coatings," *Applied Surface Science*, Vol. 252, pp. 2882–2887.

- [Li 2012a] Li, J., Chen, C., and Wang, D., 2012, "Surface Modification of Titanium Alloy with Laser Cladding RE Oxides Reinforced Ti3Al-matrix Composites," *Composites: Part B*, Vol. 43, pp. 1207–1212.

- [Li 2012b] Li, J., Chen, C., and Wang, D., 2012, "Effect of SiC/nano-CeO_2 on Wear Resistance and Microstructures of Ti_3Al/g-Ni Matrix Laser Cladded Composite Coating on Ti-6Al-4V Alloy," *Surface and Interface Analysis*, Vol. 44, pp. 559–564.

- [Liu 1995] Liu, D.M., Tuan, W.H., and Chiu, C.C., 1995, "Thermal Diffusivity, Heat Capacity and Thermal Conductivity in Al_2O_3-Ni Composite," *Materials Science and Engineering: B*, Vol. 31(3), pp. 287-291.

- [Low 2006] Low, C.T.J., Wills, R.G.A., and Walsh, F.C., 2006, "Electrodeposition of Composite Coatings Containing Nanoparticles in a Metal Deposit," *Surface & Coatings Technology*, Vol. 201, pp. 371–383.

- [Ma 2013] Ma, C., Vadali, M., Duffie, N.A., Pfefferkorn, F.E., and Li, X., 2013, "Melt Pool Flow and Surface Evolution during Pulsed Laser Micro Polishing of Ti6Al4V," *Journal of Manufacturing Science and Engineering*, Vol. 135, pp. 061023-1–061023-8.

- [Ma 2014] Ma, C., Vadali, Li, X., Duffie, N.A., and Pfefferkorn, F.E., 2014, "Analytical and Experimental Investigation of Thermocapillary Flow in Pulsed Laser Micropolishing," *Journal of Micro and Nano-Manufacturing*, Vol. 2(2), pp. 021010-1–021010-8.

- [Mai 2004] Mai, T.A., and Lim, G.C., 2004, "Micromelting and its Effects on Surface Topography and Properties in Laser Polishing of Stainless Steel," *Journal of Laser Applications*, Vol. 16, pp. 221–228.

- [Marella 1989] Marella P.F., Tuckerman D.B., and Pease, R.F., 1989, "Modeling of Laser Planarization of Thin Metal Films," *Applied Physics Letters*, Vol. 54, pp. 1109–1111.

- [Mills 2002] Mills, K. C., 2002, *Recommended Thermophysical Properties for Selected Commercial Alloys*, Woodhead Publishing Limited, Cambridge, UK.

- [Nan 1997] Nan, C.W., Birringer, R., Clarke, D.R., and Gleiter, H., 1997, "Effective Thermal Conductivity of Particulate Composites with Interfacial Thermal Resistance," *Journal of Applied Physics*, Vol. 81(10), pp. 6692–6699.

- [Nardone 1986] Nardone, V.C. and Prewo, K.M., 1986, "On the Strength of Discontinuous Silicon Carbide Reinforced Aluminum Composites," *Scripta Metallurgica*, Vol. 20(1), pp. 43–48.

- [Nelson 2009] Nelson, I.C., Banerjee, D., and Ponnappan, R., 2009, "Flow loop experiments using polyalphaolefin nanofluids," Journal of Thermophysics and Heat Transfer, Vol. 23, pp. 752-761.

- [Nemes 2013] Nemeş, P.I., Zaharescu, M, and Muresan, L.M., 2013, "Initial Corrosion Behavior of Composite Coatings Obtained by Co-electrodeposition of Zinc with Nanoparticles of Ti and Ce oxides," *Journal of Solid State Electrochemistry*, Vol. 17, pp. 511–518.

- [Niu 1998] Niu, F., Cantor, B. and Dobson, P.J., 1998, "Microstructure and Optical Properties of Si-Ag Nanocomposite Films Prepared by Co-sputtering," *Thin Solid Films*, Vol. 320(2), pp. 184–191.

- [Nüsser 2011] Nüsser, C., Wehrmann, I., and Willenborg, E., 2011, "Influence of Intensity Distribution and Pulse Duration on Laser Micro Polishing," *Physics Procedia*, Vol. 12, pp. 462–471.

- [Ong 1991] Ong, E., Harren, C., and Chen, S., 1991, "Metal Planarization with an Excimer Laser," *Solid State Technology*, Vol. 34, pp. 63–68.

- [Ordonez-Miranda 2011] Ordonez-Miranda, J., Yang, R., and Alvarado-Gil, J.J., 2011, "On the Thermal Conductivity of Particulate Nanocomposites," *Applied Physics Letters*, Vol. 98(23), pp. 233111-1–233111-3.

- [Parker 1961] Parker, W.J., Jenkins, R.J., Butler, C.P., and Abbott, G.L., 1961, "Flash Method of Determining Thermal Diffusivity, Heat capacity, and Thermal Conductivity," *Journal of applied physics*, Vol. 32(9), pp. 1679-1684.

- [Pendleton 1993] Pendleton, W.E., Williams, G.P., Williams, R.T., Wu, J.C., Cvijanovich, G.B., Joyce, J.L., and McCleaf, M., 1993, "Scanning Tunneling Microscopy of Nickel Surface Features before and after Rapid Melting by Excimer Laser," *AMP Journal of Technology*, Vol. 3, pp. 75–84.

- [Perry 2009a] Perry, T.L., Werschmoeller, D., Duffie, N.A., Li, X., and Pfefferkorn, F.E., 2009, "Examination of Selective Pulsed Laser Micropolishing on Microfabricated Nickel Samples Using Spatial Frequency Analysis," *Journal of Manufacturing Science and Engineering*, Vol. 131, pp. 021002-1–021002-9.

- [Perry 2009b] Perry, T.L., Werschmoeller, D., Li, X., Pfefferkorn, F.E., and Duffie, N.A., 2009, "The Effect of Laser Pulse Width and Feed Rate on Pulsed Laser Polishing of Microfabricated Nickel Samples," *Journal of Manufacturing Science and Engineering*, Vol. 131, pp. 031002-1–031002-7.

- [Pfefferkorn 2013] Pfefferkorn, F.E., Duffie, N.A., Li, X., Vadali, M., and Ma, C., 2013, "Improving Surface Finish in Pulsed Laser Micro Polishing Using Thermocapillary Flow," *CIRP Annals*, Vol. 62(1), pp. 203–206.

- [Praveen 2007] Praveen, B.M., Venkatesha, T.V., Naik, Y.A., and Prashantha, K., 2007, "Corrosion Studies of Carbon Nanotubes-Zn Composite Coating," *Surface & Coatings Technology*, Vol. 201, pp. 5836–5842.

- [Praveen 2008] Praveen, B.M., and Venkatesha, T.V., 2008, "Electrodeposition and Properties of Zn-nanosized TiO_2 Composite Coatings," *Applied Surface Science*, Vol. 254, pp. 2418–2424.

- [Poudel 2008] Poudel, B., Hao, Q., Ma, Y., Lan, Y., Minnich, A., Yu, B., Yan, X., Wang, D., Muto, A., Vashaee, D., Chen, X., Liu, J., Dresselhaus, M.S., Chen, G., and Ren, Z., 2008, "High-Thermoelectric Performance of Nanostructured Bismuth Antimony Telluride Bulk Alloys," *Science*, Vol. 320, p. 634.

- [Qu 2004] Qu, N.S., Chan, K.C., and Zhu, D., 2004, "Pulse Co-electrodeposition of Nano Al_2O_3 Whiskers Nickel Composite Coating," *Scripta Materialia*, Vol. 50, pp. 1131–1134.

- [Rai 2007] Rai, R., Elmer, J.W., Palmer, T.A., and DebRoy, T., 2007, "Heat Transfer and Fluid Flow during Keyhole Mode Laser Welding of Tantalum, Ti-6Al-4V, 304L Stainless Steel and Vanadium," *Journal of Physics D: Applied Physics*, Vol. 40, pp. 5753–5766.

- [Ramos 2001] Ramos, J.A., Murphy, J., Wood, K., Bourell, D.L., and Beaman, J.J., 2001, "Surface Roughness Enhancement of Indirect-SLS Metal Parts by Laser Surface Polishing," *The 12th Solid Freeform Fabrication Symposium*, Austin, Texas, US.

- [Ranganatha 2012] Ranganatha, S., Venkatesha, T.V., Vathsala, K., and Kumar, M.K.P., 2012, "Electrochemical Studies on Zn/nano-CeO_2 Electrodeposited Composite Coatings," *Surface & Coatings Technology*, Vol. 208, pp. 64–72.

- [Rawal 2001] Rawal, S., 2001, "Metal-matrix Composites for Space Applications," *Journal of Metals*, Vol. 53(4), pp. 14–17.

- [Ready 2001] Ready, J.F., and Farson, D.F., 2001, *LIA Handbook of Laser Material Processing*, Laser Institute of America, US.

- [Rhim 1999] Rhim, W., Ohsaka, K., Paradis, P., and Spjut, R.E., 1999, "Noncontact Technique for Measuring Surface Tension and Viscosity of Molten Materials Using High Temperature Electrostatic Levitation," *Review of Scientific Instruments*, Vol. 70, pp. 2796–2801.

- [Shao 2002] Shao, I., Vereecken, P.M., Cammarata, R.C., and Searson, P.C., 2002, "Kinetics of Particle Codeposition of Nanocomposites," *Journal of The Electrochemical Society*, Vol. 149, pp. C610–C614.

- [Sim 2005] Sim, B., and Kim, W., 2005, "Melting and Dynamic-surface Deformation in Laser Surface Heating," *International Journal of Heat and Mass Transfer*, Vol. 48, pp. 1137–1144.

- [Smithells 2004] Smithells, C.J., 2004, *Smithells Metals Reference Book*, Elsevier Butterworth-Heinemann, Boston, US.

- [Snead 2007] Snead, L.L., Nozawa, T., Katoh, Y., Byun, T., Kondo, S., and Petti, D.A., 2007, "Handbook of SiC Properties for Fuel Performance Modeling," *Journal of Nuclear Materials*, Vol. 371, pp. 329–377.

- [Song 2013] Song, B., Dong, S., Coddet, P., Zhou, G., Ouyang, S., Liao, H., and Coddet, C., 2013, "Microstructure and Tensile Behavior of Hybrid Nano-micro SiC Reinforced Iron Matrix Composites Produced by Selective Laser Melting," *Journal of Alloys and Compounds*, Vol. 579, pp. 415–421.

- [Steen 2010] Steen, W.M., 2010, *Laser Material Processing*, Springer-Verlag, New York, US.

- [Thiemig 2008] Thiemig, D., 2008, Investigation on the Mechanism of Electrocodeposition and the Structure-Properties Correlation of Nickel Nanocomposites, Ph.D. Thesis, Technischen Universität Dresden, Germany.

- [Tiznobaik 2009] Tiznobaik, H., and Shin, D., 2009, "Enhanced specific heat capacity of high-temperature molten salt-based nanofluids," International Journal of Heat and Mass Transfer, Vol. 57, pp. 542-548.

- [Tong 1998a] Tong, X.C, and Fang, H.S., 1998, "Al-TiC Composites in situ-processed by Ingot Metallurgy and Rapid Solidification Technology: Part I. Microstructural Evolution," *Metallurgical and Materials Transactions*, Vol. 29(3), pp. 875–891.

- [Tong 1998b] Tong, X.C, and Fang, H.S., 1998, "Al-TiC Composites in situ-processed by Ingot Metallurgy and Rapid Solidification Technology: Part II. Mechanical Behavior," *Metallurgical and Materials Transactions*, Vol. 29(3), pp. 893–902.

- [Tsai 1989] Tsai, M.C., and Kou, S., 1989, "Marangoni Convection in Weld Pools with a Free Surface," *International Journal for Numerical Methods in Fluids*, Vol. 9, pp.1503–1516.

- [Tuckerman 1986] Tuckerman, D.B., and Weisberg, A.H., 1986, "Planarization of Gold and Aluminum Thin Films Using a Pulsed Laser," *IEEE Electron Device Letters*, Vol. EDL-7, pp. 1–4.

- [Ukar 2008] Ukar, E., Lamikiz, A., López de Lacelle, L.N., Liebana, F., and Etayo, J.M., 2008, "Laser Polishing Parameter Optimization for Die and Moulds Surface Finishing," *Proceedings of the 2008 International Manufacturing Science and Engineering Conference*, Evanston, Illinois, US.

- [Vadali 2012] Vadali, M., Ma, C., Duffie, N.A., Li, X., and Pfefferkorn, F.E., 2012, "Pulsed Laser Micro Polishing: Surface Prediction Model," *Journal of Manufacturing Processes*, Vol. 14, pp. 307–315.

- [Vadali 2013] Vadali, M., Ma, C., Duffie, N.A., Li, X., and Pfefferkorn, F.E., 2013, "Effects of Pulse Duration on Laser Micro Polishing using Spatial Gaussian Intensity Distribution," *Journal of Micro and Nano-Manufacturing*, Vol. 1(1), pp. 011006-1–011006-9.

- [Vafaei 2006] Vafaei, S., Borca-Tasciuc, T., Podowski, M.Z., Purkayastha, A., Ramanath, G., and Ajayan, P.M., 2006, "Effect of Nanoparticles on Sessile Droplet Contact Angle," *Nanotechnology*, Vol. 17, p. 2523.

- [Vafaei 2009] Vafaei, S., Purkayastha, A., Jain, A., Ramanath, G., and Borca-Tasciuc, T., 2009, "The Effect of Nanoparticles on the Liquid–gas Surface Tension of Bi_2Te_3 Nanofluids," *Nanotechnology*, Vol. 20, p. 185702.

- [Vathsala 2011] Vathsala, K., and Venkatesha, T.V., 2011, "Zn-ZrO_2 Nanocomposite Coatings: Elecrodeposition and Evaluation of Corrosion Resistance," *Applied Surface Science*, Vol. 257, pp. 8929–8936.

- [Vereecken 2000] Vereecken, P.M., Shao, I., and Searson, P.C., 2000, "Particle Codeposition in Nanocomposite Films," *Journal of The Electrochemical Society*, Vol. 147, pp. 2572–2575.

- [Vlasa 2010] Vlasa, A., Varvara, S., Pop, A., Bulea, C., and Muresan, L.M., 2010, "Electrodeposited Zn-TiO_2 Nanocomposite Coatings and their Corrosion Behavior," *Journal of Applied Electrochemistry*, Vol. 40, pp. 1519–1527.

- [Wang 1998] Wang, H., Bourell, D.L., and Beaman, J.J., 1998, "Laser Polishing of Silica Rods," *Proceedings of the 9th Solid Freeform Fabrication Symposium*, Austin, Texas, US.

- [Wang 2008] Wang, A.H. Zhang, X.L., Zhang, X.F., Qiao, X.Y., Xu, H.G., and Xie, C.S., 2008, "Ni-based Alloy/submicron WS_2 Self-lubricating Composite Coating Synthesized by Nd:YAG Laser Cladding," *Materials Science and Engineering A*, Vol. 475 pp. 312–318.

- [Wang 2009a] Wang, C., Zhong, Y., Wang, J., Wang, Z., Ren, W., Lei, Z., and Ren, Z., 2009, "Effect of Magnetic Field on Electroplating Ni/nano-Al_2O_3 Composite Coating," *Journal of Electroanalytical Chemistry*, Vol. 630, pp. 42–48.

- [Wang 2009b] Wang, H.Y., Zuo, D.W., Sun, Y.L., Xu, F., and Zhang, D., 2009, "Microstructure of Nanometer Al_2O_3 Dispersion Strengthened Ni-based High-temperature Protective Coatings by Laser Cladding," *Transactions of Nonferrous Metals Society of China*, Vol. 19, pp. 586–591.

- [Wang 2010a] Wang, H., Zuo, D., Li, X., Chen, K., and Huang, M., 2010, "Effects of CeO_2 Nanoparticles on Microstructure and Properties of Laser Cladded NiCoCrAlY Coatings," *Journal of Rare Earths*, Vol. 28, pp. 246–250.

- [Wang 2010b] Wang, H., Zuo, D., Yan, J., Huang, M., and Li, X., 2010, "Effects of Nanometer Al_2O_3 Particles on Oxidation Behaviors of Laser Cladding Low Al NiCoCrAlY Coatings," *Oxidation of Metals*, Vol. 74, pp. 49–60.

- [Wang 2014] Wang, B., Alam, M.T., and Haque, M.A., 2014, "Grain Growth in Nanocrystalline Nickel Films at Low Temperature and Stress," *Scripta Materialia*, Vol. 71, 1–4.

- [Wu 2000] Wu, X.L., and Hong, Y.S., 2000, "Surface Amorphous and Crystalline Microstructure by Alloying Zirconium Using Nd:YAG Pulsed Laser," *Metallurgical and Materials Transactions A*, Vol. 31A, pp. 3123–3127.

- [Yamasaki 2003] Yamasaki, T., Zheng, Y.J., Ogino, Y., Terasawa, M., Mitamura, T. and Kukami, T., 2003, "Formation of Metal-TiN/TiC Nanocomposite Powders by Mechanical Alloying and Their Consolidation," *Materials Science and Engineering A*, Vol. 350A, pp. 168–172.

- [Yan 2010] Yan, H., Wang, A.H., Zhang, X.L., Huang, Z.W., Wang, W.Y., and Xie, J.P., 2010, "Nd:YAG Laser Cladding Ni Base Alloy/nano-h-BN Self-lubricating Composite Coatings," *Materials Science and Technology*, Vol 26, pp. 461–468.

- [Yang 2004] Yang, Y., Lan, J. and Li, X., 2004, "Study on Bulk Aluminum Matrix Nano-Composite Fabricated by Ultrasonic Dispersion of Nano-sized SiC Particles in Molten Aluminum Alloy," *Materials Science and Engineering A*, Vol. 380, pp. 378–383.

- [Yu 2006] Yu, S., Liu, Y., Ren, L., and Li, W., 2006, "Development of Laser-Cladding Layers Containing Nano-Al_2O_3 Particles for Wear-Resistance Materials," *Metallurgical and Materials Transactions A*, Vol. 37A, pp. 3639–3639.

- [Zebarjadi 2011] Zebarjadi, M., Joshi, G., Zhu, G., Yu, B., Minnich, A., Lan, Y., Wang, X., Dresselhaus, M., Ren, Z., Chen, G., 2011, "Power Factor Enhancement by Modulation Doping in Bulk Nanocomposites," *Nano Letters*, Vol. 11, p. 2225.

- [Zimmerman 2002] Zimmerman, A.F., Palumbo, G., Aust, K.T. and Erb, U., 2002, "Mechanical Properties of Nickel Silicon Carbide Nanocomposites," *Materials Science and Engineering A*, Vol. 328(1–2), pp.137–146.

- [Zhang 2008] Zhang, S.H., Li, M.X., Cho, T.Y., Yoon, J.H., Lee, C.G., and He, Y.Z., 2008, "Laser Clad Ni-base Alloy Added Nano- and Micron-size CeO_2 Composites," *Optics & Laser Technology*, Vol. 40, pp. 716–722.

- [Zhang 2011] Zhang, M.Y., Ye, C., Erasquin, U.J., Huynh, T., Cai, C., and Cheng, G.J., 2011, "Laser Engineered Multilayer Coating of Biphasic Calcium Phosphate/Titanium

Nanocomposite on Metal Substrates," *ACS Applied Materials & Interfaces*, Vol. 3, pp. 339–350.

- [Zheng 2008] Zheng, H., and An, M., 2008, "Electrodeposition of Zn-Ni-Al_2O_3 Nanocomposite Coatings under Ultrasound Conditions," *Journal of Alloys and Compounds*, Vol. 459, pp. 548–552.